Raman and Infrared Active Vibrations, Magnetic Ordering and Phase Stability in Lanthanum–Barium Manganites

by

CHAITALI ROY

DEPARTMENT OF PHYSICS

INDIAN INSTITUTE OF TECHNOLOGY, KANPUR

AUGUST, 1999

Raman and Infrared Active Vibrations, Magnetic Ordering and Phase Stability in Lanthanum-Barium Manganites

A Thesis Submitted
in Partial Fulfillment of the Requirements
for the Degree of

Doctor of Philosophy

by

CHAITALI ROY

to the

DEPARTMENT OF PHYSICS
INDIAN INSTITUTE OF TECHNOLOGY
KANPUR

August, 1999

CERTIFICATE
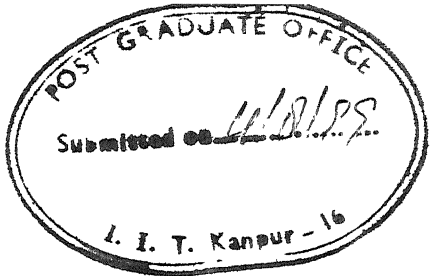
It is certified that the work contained in this thesis entitled "Raman and Infrared Active Vibrations, Magnetic Ordering and Phase Stability in Lanthanum-Barium Manganites", by Chaitali Roy. has been carried out under my supervision and that this work has not been submitted elsewhere for any degree.

4/8/99

Dr. R. C. Budhani
Professor
Department of Physics
Indian Institute of Technology
Kanpur

August, 1999

Synopsis

Name of the student	:	Chaitali Roy
Roll no	:	9310963
Department	:	Physics
Degree for which submitted	:	Ph.D.
Thesis title	:	Raman and infrared active vibrations, magnetic ordering and phase stability in lanthanum-barium manganites
Name of the thesis supervisor	:	Prof. R. C. Budhani

This thesis deals with the identification and subsequent studies of structural and magnetic behavior of different crystallographic phases present in the ceramic system $La_{1-x}Ba_x MnO_3$ where x varies from 0 to 1. The experimental techniques used to probe these aspects are X-ray diffraction, Raman spectroscopy, infrared absorption measurements and high-field magnetometry over a broad range of temperatures. The doped manganites of the type $R_{1-x}A_x MnO_3$ (R = rare-earth element La, Nd, Pr, *etc.* and A = Ca, Sr, Ba or Pb) provide systems where strong interactions between the charge, spin and lattice degrees of freedom lead to a rich variety of physical phenomena. Within the perovskite structure, the strength of these interactions depends on the ionic radii of the R and A cations, their relative concentration and on deviations in oxygen stoichiometry. In a certain concentration range the perovskite structure itself may become unstable leading to a two-phase mixture with insuing granularity in various physical properties. Amongst the family of $R_{1-x}A_x MnO_3$, the compounds which have been studied extensively are $La_{1-x}Ca_x MnO_3$

and $La_{1-x}Sr_xMnO_3$. These two systems show considerable variance in their properties owing to the difference in the ionic radius of Ca^{2+} and Sr^{2+}. The next divalent dopant with a still higher ionic radius is barium. Surprisingly, however, the issues related to phase stability and magnetic behavior of $La_{1-x}Ba_xMnO_3$ system are relatively unexplored We have therefore undertaken a systematic study of phase stability and magnetic behavior of $La_{1-x}Ba_xMnO_3$ system. The studies of vibrational, electronic and magnetic excitations in these perovskites with optical spectroscopy techniques such as Raman scattering and infrared absorption are also lacking. In order to look into the lattice dynamical aspects of the manganites in general, this work also reports laser Raman scattering and infrared spectroscopy studies of the $La_{1-x}Ba_xMnO_3$ system. The specific objectives of this thesis are as follows;

1. To study the formation of different crystallographic phases and their characteristic Raman and infrared spectra in the manganite system $La_{1-x}Ba_xMnO_3$ for x in the range of $0 \leq x \leq 1$, and with variation in oxygen stoichiometry.

2. To study the onset of ferromagnetism in Ba substituted $LaMnO_3$ and a comparative study of the ordering temperatures with that of Ca and Sr doped manganite in order to elucidate the influence of ionic size on the ordering temperature.

3. To establish the magnetic state of the two-phase region and study magnetic granularity of the material.

4. To study the influence of magnetic ordering on the local atomic arrangement through studies of the temperature dependence of the Raman active phonon modes.

The thesis has been divided into seven Chapters. A summary of the Chapters is as follows :

Chapter 1 presents an overview of the structural, magnetic and electronic aspects of the $La_{1-x}A_xMnO_3$. The stability of the perovskite structure in Ca, Sr and Ba substituted material is discussed and various polymorphic forms of the end members are introduced.

The ordering of Mn^{3+} and Mn^{4+} ions and the formation of ordered phases is discussed. In this Chapter we also review the limited Raman and IR spectroscopy work that has been reported on these compounds.

Chapter 2 describes the experimental techniques used to investigate the structural and magnetic properties of the samples. The method of sample preparation and the use of sample characterization tools such as scanning electron microscopy and x-ray diffraction are also discussed in this Chapter. Various important features of Raman scattering and IR transmission measurement techniques are summarized aswell. Detail of the advanced spectrographs, Raman microprobes and high performance charge coupled device (CCD) are discussed critically.

The presence of various crystallographic phases in the $La_{1-x}Ba_xMnO_3$ system is given in Chapter 3. The powder X-ray diffraction technique has been utilized to verify the crystallographic structure of the samples. Synthesis of the end member $LaMnO_3$ in pure argon environment leads to the formation of JT distorted, antiferromagnetic orthomanganite. The oxygen rich $LaMnO_3$ is rhombohedral. In Ba-substituted compositions with $0<x\leq0.25$, a single phase rhombohedral compound of decreasing rhombocity is formed. A further increase in x leads to the ideal cubic perovskite structure. The critical Ba-concentration (x_c) upto which the perovskite phase is stable in the series $La_{1-x}Ba_xMnO_3$ has been established from XRD measurements as 0.40. For $x>x_c$, the system phase separates into cubic $LaBaMnO_3$ and hexagonal $BaMnO_3$.

Chapter 4 deals with the room temperature Raman and IR study of $La_{1-x}Ba_x MnO_3$ series over the composition range $0\leq x\leq1$. The spectroscopy studies on the end members have also been performed by varying the oxygen stoichiometry. The results of a factor group analysis of allowed zero-wave-vector phonon modes for different crystal symmetries are presented in tabular form. The micro-Raman and IR transmission techniques have been utilized to establish the critical concentration x_c for phase separation. The presence of various Raman and IR active phonon modes is analysed within the framework of the group theoretical analysis. The observed Raman modes for $LaMnO_3$ compound are primar-

ily due to the internal vibrations of the MnO_6 octahedra. The oxygen rich rhombohedral $LaMnO_{3+\delta}$, has fewer zero-wave-vector phonon modes. In Ba-substituted compounds for higher values of x (>0.25) the ideal cubic perovskite structure does not yield any Raman active mode. However, the compound with x=0 35, shows faint Raman modes of hexagonal $BaMnO_3$ ($P6_3mc$, noncentrosymmetric group) whose presence is not observed in X-ray diffraction pattern of the sample with x=0.35. The IR spectra show an absorption edge in addition to the IR active phonons. The absorption edge shifts to lower energies and phonon modes are screened as more and more holes are doped in the system with increasing Ba concentration. An attempt has been made to correlate the progressive increase in symmetry of the crystal structure, shift of IR absorption edge to lower energies and disappearance of phonon modes with x and δ with the reported electrical and magnetic behavior of this hole-doped manganite.

In Chapter 5, the magnetic behavior of $La_{1-x}Ba_xMnO_3$ bulk samples is studied over a wide range of composition ($0 \leq x \leq 1$), temperature (4.2 K - 775 K) and magnetic field strength (1 G - 50 kG). The ordered moment on $LaMnO_{3+\delta}$ depends sensitively on the processing conditions and the lowest value of 0.006 μ_β per Mn ion at 4.2K is realized in the antiferromagnetic compound of δ=0. The complex magnetic behavior of $BaMnO_3$ suggests antiferromagnetic ordering below ~150K. The Ba-substituted compounds order ferromagnetically with a monotonic increase of T_c and saturation magnetization M_s with x<0.35. In the two-phase region (x>0.35), M_s scales with the fraction of the ferromagnetic phase ($La_{0.65}Ba_{0.35}MnO_3$) present in the sample. Magnetic granularity, superparamagnetism and an effective medium approach of susceptibility of the two-phase mixture are discussed in this Chapter.

The results of the temperature dependence of the Raman active modes in $LaMnO_3$ and $BaMnO_3$ are presented in Chapter 6. The temperature variation of Raman spectra have been obtained over a temperature range of 10 - 300 K. A structural instability associated with the antiferromagnetic ordering has been noticed in the phonon spectra of the orthomanganite $LaMnO_3$ samples. The behavior of certain phonon modes at T_N suggests

a sudden change in the topology of the MnO_6 octahedra. The temperature dependence of the frequency and linewidth of various Raman active modes of $BaMnO_3$ compound is measured and attributed to the anharmonic terms in the vibrational potential energy of the lattice.

Chapter 7 summarizes the important findings of this work and also identifies scope for future work.

Acknowledgements

Chaitali Roy

Dedicated

to

My Dear Parents

List of Publications

In Refereed Technical Journals :

1. "Raman- and infrared- active phonons in hexagonal $BaMnO_3$", Chaitali Roy and R. C. Budhani, *Phys. Rev. B* **58**, 8174 (1998).

2. "Raman-, infrared- and X-ray diffraction study of phase stability in $La_{1-x}Ba_xMnO_3$ doped manganites", Chaitali Roy and R. C. Budhani, *J. Appl. Phys.* **85**, 3124 (1999).

3. "Magnetic ordering and granularity effects in $La_{1-x}Ba_xMnO_3$ ", R. C. Budhani, Chaitali Roy, Laura H. Lewis, Qiang Li and A. R. Moodenbaugh, *Communicated.*

In Conference Proceedings :

1. "Inelastic light scattering and magnetic ordering in doped lanthanum manganites", Chaitali Roy, R. C. Budhani, P. S. Dobal and H. D. Bist, *Proc. DAE Solid State Phys. Symp.* BARC Mumbai, India, Dec 1996, p-95.

2. "Inelastic light scattering from $AMnO_3$ (A = Sr, Ca and Ba)", Chaitali Roy and R. C. Budhani, *Proc. National Laser Symp.* PRL Ahmed-

abad, India, Dec 1997, p-116.

3. "Raman scattering from hexagonal $BaMnO_{3-\delta}$, $(\delta \geq 0)$", Chaitali Roy and R. C. Budhani, *Proc. National Laser Symp.* IIT Kanpur, India. Dec 1998, p-106.

Contents

List of Figures

List of Tables

Chapter 1

Introduction

The mixed valent oxides of the type $R_{1-x}A_x\text{MnO}_3$, where R is a rare-earth element like La, Pr or Nd and A is the divalent Ca, Sr, or Ba, have been a subject of scientific investigations for many decades [1, 2]. The recent interest in this family of materials has been stimulated by the observation of a large negative magnetoresistance [3-5], charge and spin ordering effect as a function of Mn^{3+} / Mn^{4+} ratio [6, 7], and lattice instabilities and distortions [8]. These systems display a rich variety of structural, magnetic and metal-insulator phase transitions as a function of temperature, pressure and doping of divalent cation, viz Ca, Sr [9, 10]. The similarity of many issues related to magnetism and transport properties in these perovskites with the high T_c cuprates [11] has been an additional factor contributing to the recent global interest.

The need to understand the structural, magnetic and electrical behavior of these doped transition metal oxides in bulk and thin film forms has also arisen due to their potential for many technological applications. While the established areas of applications are as magnetic read-write heads, magnetic sensors [4], electrode materials for MHD generation [12], batteries and fuel cells [13], and many new applications may emmerge with the development of multilayer deposition technology. Perovskite type oxides, in general, are also catalysts for many reactions among which are those involved in the removal of atmo-

spheric contaminants (CO, hydrocarbons and NO_x) from vehicle exhaust gases. The use of non-stoichiometric lanthanum manganites as electro-catalytic oxygen electrodes in aquous solutions has also been studied [14, 15]. Correlations have been established between their catalytic activity and physical properties by several authors [16, 17] Most of the exhotic properties of these oxides originate from the partially filled 'd' shell of the transition metal present in the system. The most extensively studied derivatives of the above general class of oxides are the compounds with formula $La_{1-x}A_xMnO_3$. The strontium and calcium substituted lanthanum manganites have been extensively studied by a large number of workers, and the Sr-doped compound, in particular, has found extensive use as a cathode material for solid oxide fuel cells (SOFC) [13]. However, a limited literature is available for barium-substituted lanthanum manganite [1, 18-20], although it is also expected to show a variety of interesting physical and chemical properties.

The end members of this series, namely $LaMnO_{3-\delta}$ and $AMnO_{3-\delta}$ where δ represents the propensity of the Mn ions to be in 3+ or 4+ valence state, also present two interesting classes of oxides. While $LaMnO_3$ is a Jahn-Teller (JT) distorted cubic perovskite having antiferromagnetically ordered canted Mn^{3+} spins and an electrically insulating ground state [21, 22], the magnetic and crystallographic structure of $AMnO_3$ is quite complex. The cubic structure is retained in the case of $CaMnO_3$ whereas $SrMnO_3$ and $BaMnO_3$ crystallize into hexagonal lattice. The detailed structural aspect of these compounds will be discussed in the following sections.

The structural and magnetic phase diagram of $La_{1-x}Ca_xMnO_3$ system has been studied in detail [9]. Structurally, there is a complete solubility between the two end members of this series. The stability of the perovskite structure as a function of Sr or Ba concentration, on the other hand, is not well established. However, there are a large number of recent studies on electron transport mechanism and magnetic ordering of $La_{1-x}Sr_xMnO_3$ [10, 22-25] system for x$\leq$ 0.4 where a single phase is formed. For the still larger ion, Ba^{2+} - based compound, detailed studies are lacking.

Most of the information available on the structure and phase stability of $La_{1-x}A_xMnO_3$

alloys has been deduced through macroscopic tools such as x-ray and neutron diffraction or inferred from susceptibility measurements. A lot more could be learned about the physics of these materials through light scattering and infrared (IR) absorption experiments. Inelastic scattering of light by vibrational, magnetic and electronic excitations in these system, for example, can provide a powerful means to track the structural and magnetic phase transformation as a function of temperature and composition. Similarly, light transmission/absorption studies allow understanding of the electronic and vibrational excitations. Light scattering spectroscopy is now firmly established as a standard technique for measuring magnetic excitations in solids. The theoretical interpretation of such spectra is well developed, and considerable physical information about the magnetic properties of solids can be learned from their light scattering spectra. While Raman scattering (RS) has been used extensively to study vibrational and magnetic excitations in various alkali halide based perovskites [26, 27], and ternary oxides of iron and chromium [28, 29], the field of manganites is relatively unexplored except for some very recent studies.

In spite of the voluminous recent work on Ca or Sr doped manganite systems, several important questions still remain unanswered.

- Can one assume the results of Ca- or Sr- doped manganites as models for the Ba-doped materials ? How would the larger ionic radius of Ba^{2+} affect the electrical, magnetic and structural properties of the manganite ?

- Is there a complete structural solubility between $BaMnO_3$ and $LaMnO_3$? How would cation vacancies affect the properties of these compounds ?

- Do the crystallographic structure and magnetic state change by introduction of cation vacancies or variation of oxygen stoichiometry in $La_{1-x}Ba_xMnO_3$ series ?

All these questions motivated us to carry out a systematic study of the structural and magnetic behavior of this interesting manganite system with Ba- as divalent dopant. To arrive at some meaningful conclusions, we have probed the series $La_{1-x}Ba_xMnO_3$ ($0 \leq x \leq 1$) with the following experimental techniques,

1. X-ray powder diffraction,

2. Laser Raman Scattering,

3. Infrared absorption, and

4. Magnetization measurements.

Having stated the basic objectives of the thesis, we would like to begin with a brief overview of the structure, magnetic ordering and phase stability of the lanthanum manganite system.

1.1 Overview of $La_{1-x}A_xMnO_3$

1.1.1 Crystallographic Structure

The crystallographic symmetry of lanthanum manganite compounds belongs to the perovskite related structure. The oxides crystalizing in perovskite structure can be assigned the chemical formula ABO_3, where A denotes a larger ion *viz.* Ca^{2+}, Sr^{2+}, Ba^{2+}, Cd^{2-}, Pb^{2+}, La^{3+}, Pr^{3+}, Nd^{3+}, Gd^{3+}, Y^{3+} *etc.*, while B is the small metal ion *viz.* Al^{3+}, Cr^{3-}, Mn^{3+}, Fe^{3+}, Ti^{3+}, Mn^{4+} *etc.*, and O, the oxygen ion [30]. The perovskite unit cell is shown in Fig.1.1. The ABO_3 perovskite type structure is a closed packed AO_3 lattice with B ions in the octahedral sites that are completely surrounded by the oxygen ions. The structure of all the known copper oxide based high T_c superconductors can also be described in terms of a stacking of the (AO) or 'rock salt type' and (BO_2) or perovskite-type planes in suitable sequence [31].

Stability of the Perovskite Structure

It was pointed out by Goldschmidt [32] that the perovskite structure is stable only if the tolerance factor t, defined by

$$t = \frac{r_A + r_O}{\sqrt{2}(r_B + r_O)} \qquad (1.1)$$
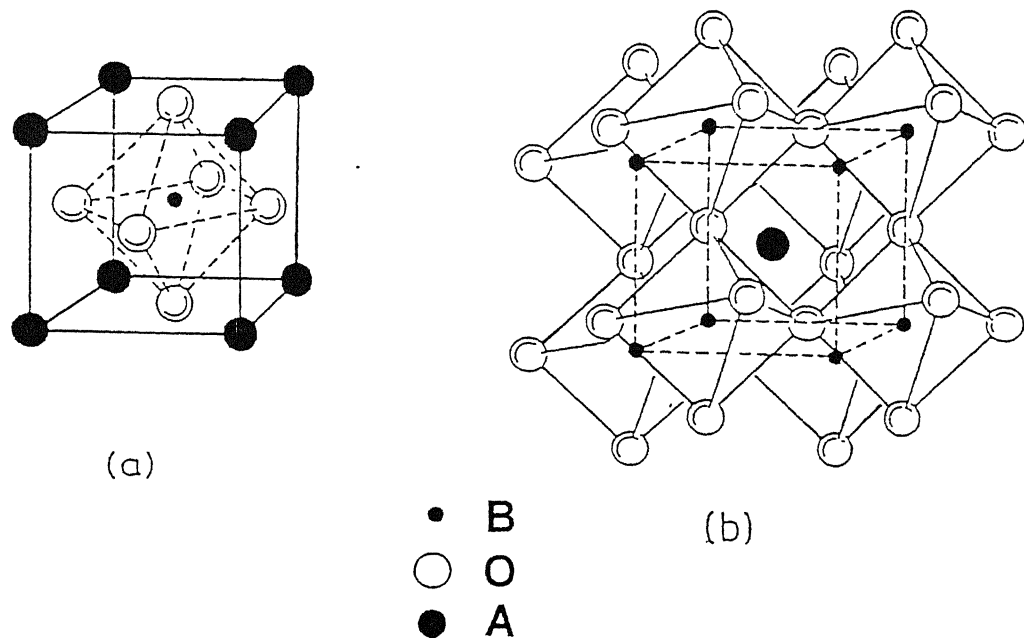
Figure 1.1: (a) The ABO_3 structure; (b) the oxygen octahedra.

equals unity. Where r_A, the radius of A ion, r_B, the radius of B ion, and r_O, the radius of O ion respectively. A purely cubic structure is found if it is equal to unity as is the case for strontium titanate ($SrTiO_3$). When the tolerence factor (t) is different from unity the perovskite structure shows distortions from the cubic symmetry such as in $CaTiO_3$ and $BaTiO_3$. However, large deviations from unity result in completely different crystal structures (*e.g.* ilmenite for t<1, calcite and argonite for t>1). Table 1.1 shows the

Table 1.1: The values of tolerance factor 't' and crystallographic symmetry for various ABO_3 oxides

Compound	t	Structure	Compound	t	Structure
* $LaMnO_3$	0.89	Orthorhombic	* $CaMnO_3$	0.91	Cubic
* $(Pr, Nd)MnO_3$	0.86	Pseudocubic	$SrMnO_3$	0.99	Hexagonal
* $GdMnO_3$	0.85	Orthorhombic	$BaMnO_3$	1.05	Hexagonal
$YMnO_3$	0.83	Hexagonal			
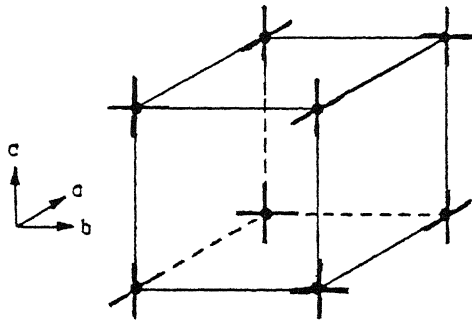
Figure 1.2: Simple-cubic array of transition-element ions in perovskite-type lattice, showing the orientations of empty $d_{x^2-y^2}$ orbitals responsible for orthorhombic symmetry [34].

values of tolerance factor and the corresponding structure for various ABO_3 oxides. The compounds showing perovskite structure are marked with an asterisk. In the following we discuss the structure of $La_{1-x}A_xMnO_3$ compounds in detail.

(a) $LaMnO_{3+\delta}, \delta \geq 0$

As discussed above, the $LaMnO_3$ perovskite type structure is a closed packed LaO_3 lattice with the Mn ions in the octahedral sites which are completely surrounded by six oxygen ions. At room temperature, stoichiometric $LaMnO_3$ is orthorhombic due to a mismatch between La-O and Mn-O bond lengths, and due to a cooperative JT distortion associated with Mn^{3+} ions. The structure transforms towards more symmetric phase such as rhombo-hedral or monoclinic with the rise of temperature [33]. The orthorhombic distortion from cubic symmetry observed for pure $LaMnO_3$ is larger than that for the other orthorhombic perovskites. Goodenough [34, 35] has indicated that this large orthorhombic distortion is due to a particular ordering of the four coplanar, empty orbitals of the Mn^{3+} ions as shown in Fig.1.2. Smaller distortion from the cubic symmetry results when this ordering is destroyed. The substitution of ions such as Mn^{4+}, Cr^{3+}, Co^{3+} and Fe^{3+} which do not have

an unequal occupation of d_{z^2} and $d_{x^2-y^2}$ orbitals at the octahedral oxygen-ion interstice reduce the number of Jahn-Teller ion (Mn^{3-}) which are available to participate in the distortion mechanism. Consequently, the magnitude of this distortion and temperature of the transition from orthorhombic to rhombohedral are expected to decrease with increasing concentration of the foreign ions (non Jahn-Teller).

The changes in the crystallographic structure, magnetic and electrical properties of the nonstoichiometric $LaMnO_{3+\delta}$ for δ greater than zero, have been studied by many workers [19, 36-37]. Here the 'δ' is a positive fraction which represents the vacancy content on the metal sites and not any extra oxygen in the lattice. The tendency of manganese atoms to adopt a 4+ state leads to a non-zero value of δ. The composition of $LaMnO_{3+\delta}$ is better expressed as $La_{1-\epsilon}Mn_{1-\epsilon}O_3$ with $\epsilon = \delta/(3+\delta)$ or $LaMn^{3+}_{1-2\delta}Mn^{4+}_{2\delta}O_{3-\delta}$. Powder X-ray diffraction measurements of Topfer and Goodenough [21] show a distinct orthorhombic phase for $0\leq \delta \leq 0.06$ and a rhombohedral phase for $0.1\leq \delta \leq 0.18$. For δ between 0.06 and 0.10, a two-phase mixture of orthorhombic and rhombohedral phases is predicted. Verelst *et al.* [37] have shown the structural change in $LaMnO_{3+\delta}$ from orthorhombic to cubic (via rhombohedral) with increase in Mn^{4+} content. According to their measurements, the compound is orthorhombic (Pbnm, Z=4) up to ~20% Mn^{4+} and becomes rhombohedral ($R\bar{3}c$, Z=2) up to ~30% Mn^{4+}, the compound becomes cubic (Fm3m, Z=8) if Mn^{4+} content exceeds 30%. Van Roosmalen *et al.* [38] have shown by neutron diffraction that doubling of the unit cell is likely for rhombohedral $LaMnO_{3+\delta}$. This was also observed by Tofield and Scott [39], and for orthorhombic $LaMnO_{3.00}$ by Elemans *et al.* [19]. Neutron diffraction results [38] indicate that the atomic positions in the doubled unit cell are shifted only slightly and that the structure of $LaMnO_{3+\delta}$ compounds can be described satisfactorily in the usual orthorhombic and rhombohedral unit cells [Fig.1.3].

(b) $La_{1-x}A_xMnO_3$, ($A = $ Ca, Sr, and Ba)

The structural aspects of $La_{1-x}Ca_xMnO_3$ have been studied extensively [1, 22, 40-42]. The work on this material was started in early fifties by Jonker and van Santen [1], which
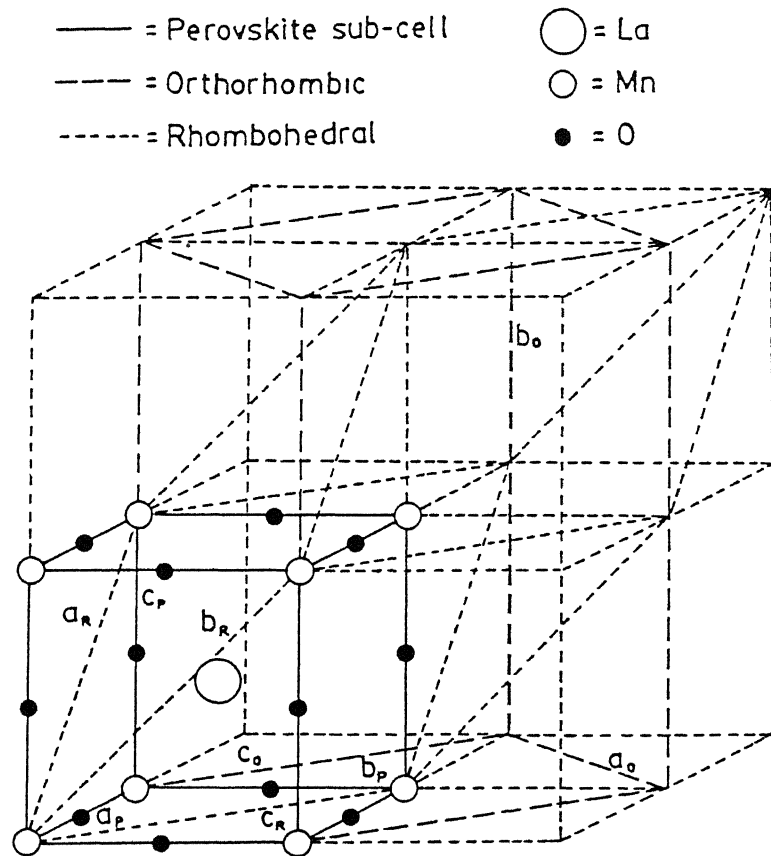
Figure 1.3: Comparison of the orthorhombic and rhombohedral unit cell of $LaMnO_{3+\delta}$, drawn in a nondistorted perovskite structure. Both can be expressed in the perovskite subcell [38].

showed a complete structural solubility of this series for entire range of Ca doping. In the year 1970, G. Matsumoto [42] published an extensive piece of work on the structural and magnetic properties of $La_{1-x}Ca_xMnO_3$ ($0 \leq x \leq 0.3$) compounds synthesized using standard solid state reaction method. The phase diagram according to this work shows that the system at room temperature is monoclinic for $x < 0.04$, orthorhombic for $0.04 < x < 0.125$, and cubic for $x > 0.125$. In the pure compound, the transition temperature from monoclinic to cubic phase is in the range of 750-780K. The phase transition temperature from monoclinic phase to the cubic one decreases sharply with increase in Ca concentration. In 1982, Tanaka *et al.* [43] had carried out the crystallographic and magnetic studies of $La_{0.8}Ca_{0.2}MnO_3$ samples prepared using two different methods one involving coprecipitation of metal ions from aquous solution and the other the standard solid-phase reaction approach. The sample prepared by coprecipitation method was found to have monoclinic structure and the one synthesized using the standard solid-phase reaction yielded a cubic material. The difference of the structures between these two samples has been attributed to the homogeneity of distribution of ions in the two types of samples. The coprecipitation method, in principle, gives material where the constituents are homogeneously distributed in an atomistic scale. Hence, these authors attributed the symmetry of $La_{0.8}Ca_{0.2}MnO_3$ to be monoclinic. However, a recent work [22] dealing with the studies on structure, transport, and magnetic properties of $La_{1-x}Ca_xMnO_3$ over a wide range of compositions synthesized by solid-state reaction route shows that the room temperature structures are as follows; orthorhombic for $0 \leq x \leq 0.1$, rhombohedral for $0.1 < x < 0.2$ and cubic for $0.2 \leq x \leq 1.0$.

The work on the Sr based material by Jonker and van Santen [1], shows that the perovskite phase is stable upto 70% of Sr doping in $LaMnO_3$. The studies on Sr doped lanthanum manganites synthesized by solid state method reveal that the compound is rhombohedral for x in the range of 0.1 - 0.3, and cubic when x=0.4 - 0.5 [22]. However, the crystal structure of $La_{1-x}Sr_xMnO_3$ grown by floating zone (FZ) method studied by Urushibara *et al.* [10] gives a different picture. The compound seems to be orthorhombic (Pbnm, Z=4) up to the composition x=0.15, then the structure changes to rhombohedral

(R$\bar{3}$c, Z=2) for 0.175$\leq$x$\leq$0.6 at room temperature. From these reports it is clear that a considerable amount of ambiguity exist about the solubility of Sr in the perovskite lattice of LaMnO$_3$. The compounds La$_{1-x}$Sr$_x$MnO$_3$ also undergo rich structural and magnetic phase transitions [44-45] as a function of temperature and pressure. The temperature at which the structural phase transition (SPT) from a high-temperature rhombohedral phase (R$\bar{3}$c) to a low temperature orthorhombic phase (Pbnm) takes place is very sensitive to the level of doping (x).

The studies of La$_{1-x}$Ba$_x$MnO$_3$ were started as early as 1950 by Jonker and van Santen [1]. However, compared to the works on Ca or Sr doped materials, the crystallographic as well as magnetic phase diagram of the Ba substituted manganites are poorly understood. This is inspite of the fact that the study which generated so much of interest in the manganite was done on thin film samples of La$_{0.67}$Ba$_{0.33}$MnO$_3$ by von Helmolt *et al.* [3]. The studies of Jonker and van Santen [1] show the formation of a two-phase mixture beyond 45% of divalent Ba doping in place of trivalent La. Recent X-ray diffraction (XRD) results of Chakraborty *et al.* [46] show that the material exists as a single phase having perovskite structure up to 40% substitution of Ba for La. For the Ba concentration in the range of 40 - 50 percent these workers found a two phase mixture. Recently, Dabrowski *et al.* [47] have reported structural, magnetic and transport properties of the single-phase and vacancy free samples of La$_{1-x}$Ba$_x$MnO$_3$ in the composition range x=0.12-0.24. The structural studies in this work were carried out using powder neutron diffraction method. The room temperature powder diffraction data show that the system is orthorhombic for 0$\leq$x$\leq$0.13 and the rhombohedral phase is stabilized for 0.13$\leq$x. This should be contrasted with the critical concentration x of 0.165 at which the rhombohedral phase wins over the orthorhombic phase in the Sr-substituted LaMnO$_3$. The structural aspects of Ba-doped LaMnO$_3$ compound have been discussed by Dabrowski *et al.* [47] in the framework of tolerance factor concept. Since the ionic size of Ba is considerably larger than that of Sr or Ca, the tolerance factor increases faster with Ba substitution than with Sr or Ca substitution. Thus, the materials with the composition of x$_{Ba}$ =0.13 and x$_{Sr}$=0.165 have

very similar tolerance factor t=0.975 and 0.971 respectively.

(c) $AMnO_{3-\delta}, \delta \geq 0$

The crystallographic structure of the other end member of the $La_{1-x}A_xMnO_3$ series namely $AMnO_{3-\delta}$ is quite complex Here the ideal perovskite structure consisting of all corner-sharing MnO_6 octahedra becomes unstable as the size of A cation becomes larger than the critical radius given by the Goldschmidt formula [32]. The cubic structure is retained in the case of $CaMnO_{3-\delta}$ [48] for δ as high as 0.5 [49]. However, the cubic structure is unstable for $SrMnO_3$ and $BaMnO_3$. Instead, the structure consists of a stacking of closed packed SrO_3 (or BaO_3) layers with Mn ions occupying interlayer octahedral sites [50]. Based on the number of layers, stacking sequences, and ordering of transition metal ions, numerous unique poly types of the compounds can be theoretically generated. All these structure types can be considered to consist of mixtures of two types of layer packing. A total hexagonal stacking (AB AB type) of BaO_3 layers resulting in a two-layer (2L) hexagonal cell which is characterized by infinite strings of face-sharing MnO_6 octahedra parallel to the c axis. A total cubic stacking (ABC) yields the familar perovskite structure in which all octahedra share corners. An alternation of face and corner sharing octahedra results in mixed cubic and hexagonal stacking. The typical examples of hexagonal 6L structure is $BaTiO_3$ (ABCACB) with $66\frac{2}{3}\%$ cubic stacking [51] and the 4L structure of $SrMnO_3$ (ABAC) with 50% cubic stacking [52]. The ideal hexagonal structure however is highly sensitive to the valence state of the Mn ions. A decrease in the oxygen concentration leads to the stabilization of the Jahn-Teller Mn^{3+} and a progressive deviation from the ideal hexagonal stacking.

There are a few reports on $SrMnO_{3-\delta}$ [53-55] describing the structural and magnetic properties of 4H, 2C and 6H polymorphic forms, where H and C are the hexagonal and cubic stacking respectively. Whereas $BaMnO_{3-\delta}$ is a well studied system [50, 54, 56-59] from the crystallochemical point of view. The stoichiometric $BaMnO_3$ crystallizes in the 2L hexagonal form. This type of structure can be described as formed by a hexagonal sequence
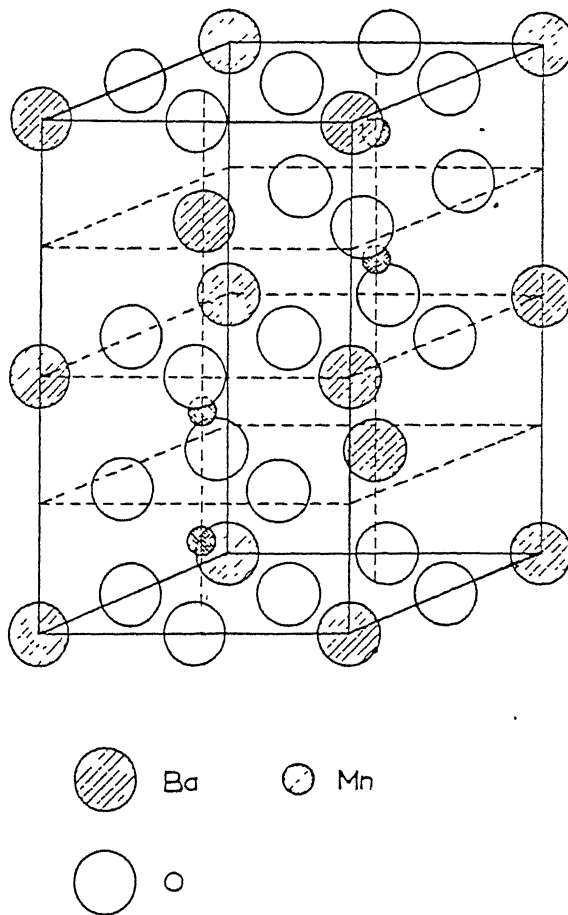
Figure 1.4: The tetramolecular cell of $BaMnO_{3-\delta}$ or the 4H structure [56].

(...hhh...) of BaO_3 layers [56]. Powder X-ray diffraction studies of Negas and Roth [50] have shown a series of different phases in the anion-deficient $BaMnO_{3-\delta}$ system ($0\leq \delta \leq 0.25$); a rhombohedral 15-layer type, $(chhhh)_3$ stacking sequence and hexagonal 8H, ...$(hhhc)_2$..... 6H, ...hchhhc...., 10H, ...$(hhchc)_2$...., and 4H, ...hchc.... types. Figure 1 4 shows the crystallographic structure of a tetramolecular $BaMnO_{3-\delta}$ or the 4H polymorphic form. The high-resolution electron microscopy measurements of Parras *et al.* [57] and Gonzalez-Calbet *et al.* [58] show that oxygen deficiency in $BaMnO_{3-\delta}$ ($0<\delta<0.25$) is accommodated by the introduction of $BaO_{2.5}$ cubic layers in the BaO_3 hexagonal layers. The ideal anionic composition for every hexagonal type can be established as $BaMnO_3$ (2H), $BaMnO_{2.90}$ (15R), $BaMnO_{2.875}$ (8H), $BaMnO_{2 83}$ (6H), $BaMnO_{2 8}$ (10H) and $BaMnO_{2 75}$ (4H). The

Table 1.2: Summary of the $BaMnO_{3-\delta}$ phases prepared by Negas and Roth [50]

Phase	Cubic stacking (%)	Stability range in air T (°C)	δ in $BaMnO_{3-\delta}$
2 - layer	0	< 1150	0.00
15 - layer	20	1150 - 1300	0.00 (?) - 0.02
8 - layer	25	1300 - 1350	0.03 - 0.05
6 - layer	$33\frac{1}{3}$	1350 - 1475	0.10 - 0.15
10 - layer	40	1475 - 1550	0 17 - 0.20
4 - layer	50	> 1550	> 0.25

structure of these compounds is very sensitive to the annealing conditions. In general. various oxygen-deficient $BaMnO_3$ polymorphic compounds are obtained starting from the stoichiometric 2L $BaMnO_3$ compound by changing the annealing temperature and oxygen partial pressure during annealing A summary of the conditions under which the 2L structure transforms to various oxygen deficient polymorphs is given in Table 1.2.

1.1.2 Magnetic Structure

(a) $LaMnO_{3+\delta}$. $\delta \geq 0$

The parent antiferromagnetic insulator $LaMnO_3$ contains Mn^{3+} ions with elctronic configuration $t_{2g}^3 e_g^1$. Among the four 3d electrons on the Mn sites, the three t_{2g} electrons occupy the tightly bound d_{xy}, d_{yz} and d_{xz} orbitals with very little hybridization with the oxygen 2p states and can be considered as a local spin of 3/2. The remaining electron occupies the e_g state made of the $d_{x^2-y^2}$ and d_{z^2} orbitals and is strongly hybridized There is a strong exchange interaction J_H (Hund's coupling) between the 3d t_{2g} local spin and the 3d e_g conduction electrons which may hop from site to site and lead to a site spin S=2. The magnetic structure of $LaMnO_{3+\delta}$ has been analyzed by various workers [2, 19, 38-39, 60]. The neutron diffraction measurements show that the stoichiometric compound
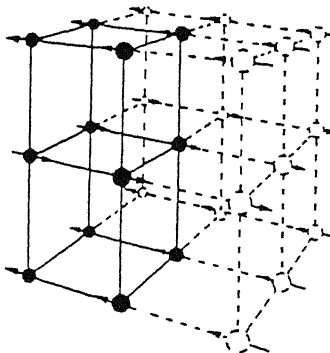
Figure 1.5: The magnetic structure of LaMnO$_3$, indicating only the manganese atoms [2].

which is orthorhombic from crystallographic point of view, orders antiferromagnetically at T$_N$ ∼140K below which some degree of canting of Mn^{3+} spins leads to a parasitic ferro-magnetism. The magnetic space group symmetry of LaMnO$_3$ is Pn'ma' [2]. The magnetic structure of LaMnO$_3$ is A-type as illustrated in Fig.1.5. It consists of ferromagnetically ordered sheets of Mn^{3+} spins such that the spins in successive sheets are ordered antiferromagnetically. The magnetic unit cell is doubled in the c-direction of the chemical cell. The nearest neighbours for each Mn ion are two ions with antiparallel spins and four with parallel spins. The moment directions lie within the ferromagnetic sheets. The recent neutron diffraction studies of LaMnO$_{3+\delta}$ by Ritter *et al.* [61] are also in good agreement with the above structure. The magnetic structure of non-stoichiometry LaMnO$_{3\,12}$ is different from the stoichiometric compound [39].

The recent structural work of Huang *et al.* [60] shows that annealing the stoichiometric LaMnO$_3$ in oxygen introduces small amount of additional oxygen in the system. This additional oxygen appears to be accommodated by the creation of La and Mn vacancies in the structure, this has the effect of changing the magnetic structure from antiferromagnetic to ferromagnetic, while crystallographically the orthorhombic splitting is first reduced in size as the number of defects increases and then a monoclinic-rhombohedral structure is formed.

(b) $La_{1-x}A_xMnO_3$, $(A = Ca, Sr, and Ba)$

A full investigation of the properties of the series of perovskite compounds $La_{1-x}Ca_xMnO_3$ has been made by several workers. In early fifties Wollan and Koehler [2] tried to establish the magnetic structure of this series. Their work shows that in $La^{3+}Mn^{3+}O_3$ which is one end member of the series, the maganese exists entirely as the Mn^{3+} ion. As one proceed to increase x through the series, Mn^{3+} ion is continuously replaced by Mn^{4-}. All Mn^{3+} sites are converted to Mn^{4+} sites when x reaches the value 1, which corresponds to $CaMnO_3$. This Calcium based manganite is also antiferromagnetic but has a type-G structure [Fig.1.6]. A G-type antiferromagnetic unit cell is shown in Fig.1.7(a). The sheets of Mn^{4-} ions now contain both + and - spins and the magnetic cell is twice as large as the chemical cell in all the three directions. Each Mn^{4+} ion has six antiparallel nearest neighbours and the structure may be regarded as two interpenetrating face centered lattices with the spin directions oppositely directed in the two cases. The moments lie in some undetermined direction within the layer planes. At intermediate compositions, a number of different ferromagnetic and antiferromagnetic structures including mixed phases occur. With increase of Mn^{4+} content, the A type magnetic structure of $LaMnO_3$ is gradually replaced by a simple ferromagnetic structure B [illustrated in Fig.1.6] in which all the moments are parallel and which is the sole phase present for an Mn^{4+} content of 40 per
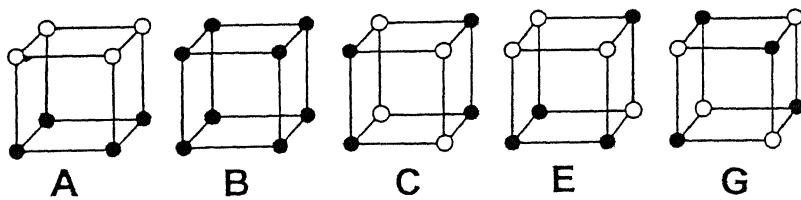
Figure 1.6: Octants of the various magnetic unit cells found in the series of perovskite-type compounds $La_{1-x}Ca_xMnO_3$. The filled and open circles indicate oppositely directed magnetic moments [2].
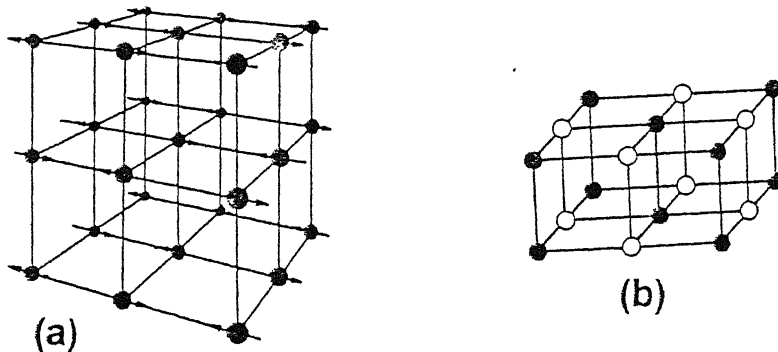
Figure 1.7: (a) The magnetic unit cell of G-type antiferromagnet. (b) The full magnetic unit cell of the type-C phase, for which two axes are doubled compared to the chemical cell in the $La_{1-x}Ca_xMnO_3$ system.

cent. Proceeding from the Ca end of the system, the type G structure of $CaMnO_3$ is replaced, at 80 percent of Mn^{4+}, by the structure shown as type C, which requires a doubling of the unit cell in two directions as seen more clearly in Fig.1.7(b). In the central region of the phase diagram (for x~0.5) a much more complicated antiferromagnetic phase is found.

(c) $BaMnO_3$

Neutron diffraction measurements of Christensen and Olliver [59] show that $BaMnO_3$ (2H) is antiferromagnetic below 150 K. The volume of the magnetic cell is three times that of the chemical cell and contains six manganese atoms. Each manganese atom has two nearest manganese atoms perpendicular to the basal plane at a distance of 2.403 Å. In the basal plane, each manganese atom has six nearest manganese atoms at a distance of 5.694 Å. The structure consists of face sharing MnO_6 octahedra stacked in the c (see Fig.1.8). These authors have proposed a model for an antiferromagnetic arrangement of the manganese spins. The spin of the manganese atom at the position (0, 0, 0) is opposite to the spin of the manganese atoms at the positions $(\frac{1}{3}, \frac{2}{3}, 0)$ and $(\frac{2}{3}, \frac{1}{3}, 0)$.
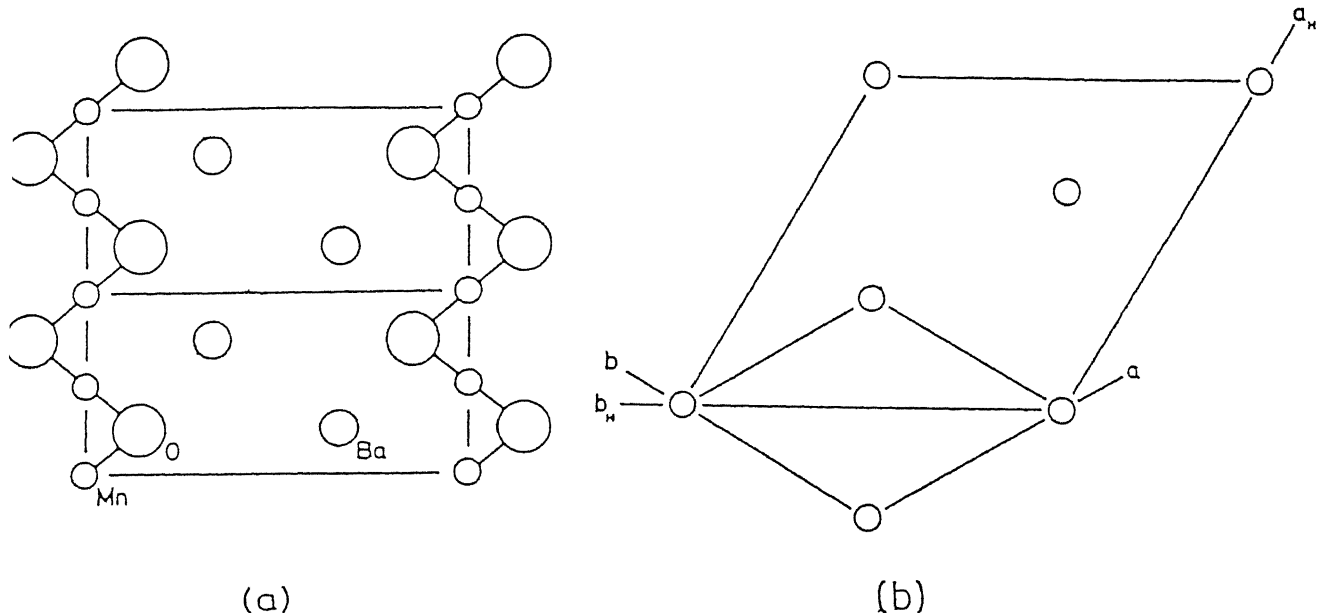
Figure 1.8. (a) Atoms in the (110) plane of the chemical unit cell of $BaMnO_3$; (b) Relation between the chemical and magnetic unit cell and positions of the manganese atoms in the magnetic cell, the other atoms have been omitted [59].

1.1.3 Magnetic Ordering Temperatures and Electrical Conduction

(a) $LaMnO_{3+\delta}, \delta \geq 0$

The magnetic behavior of $LaMnO_{3+\delta}$ has been reported by several authors [19, 21, 22, 36, 42, 61, 62]. Tofper and Goodenough [21] have measured the magnetic and transport properties of $LaMnO_{3+\delta}$ with δ in the range of 0-0.18. These studies indicate that all the samples exhibit a ferromagnetic Weiss constant θ_p that increases with δ. The temperature at which a long-range magnetic order sets in ranges from $T_N = 135K$ for $\delta = 0.00$ to $T_c = 240K$ for $\delta = 0.18$. Each sample shows a ferromagnetic component below the ordering temperature. The Curie temperature of the samples with $0.05 \leq \delta \leq 0.11$ are at about 170-180K. The saturation magnetization for $LaMnO_{3+\delta}$ increases with δ to a maximum value of $\sim 3.25 \mu_B$ around $\delta = 0.12$. But for $\delta > 0.12$, it decreases with increase in δ. The structural and magnetic studies of $LaMnO_{3+\delta}$ by Topfer and Goodenough show that below T_c three compositional domains can be distinguished; $0 < \delta < 0.07$, $0.10 < \delta < 0.14$

and $0.14 \leq \delta \leq 0.18$. The first appears to contain ferromagnetic clusters embedded in an antiferromagnetic matrix giving rise to a spin glass (SG) type magnetic behavior. With the collapse of the cooperative static JT deformation associated with the O'-orthorhombic structure the matrix becomes ferromagnetic, while some antiferromagnetic order remains in clusters of the material. In the range of $\delta \simeq 0.13$ to $\delta \simeq 0.18$, there is a transition of the charge carriers below T_c from polaronic behavior to a delocalized state and the system shows a metamagnetic behavior and a reduced magnetization.

The studies of electron transport and magnetic behavior of nonstoichiometric $LaMnO_{3-\epsilon}$ are also reported by Mahendiran et al. [22] The cubic $La_{0.945}Mn_{0.945}O_3$ (Mn^{4+} 33%) and rhombohedral $La_{0.96}Mn_{0.96}O_3$ (Mn^{4+} 24%) show sharp ferromagnetic transitions. The saturation magnetization of the cubic sample is 3.8 μ_B. The orthorhombic sample (δ=0.02) is insulator at all temperatures. The resistivity data of the rhombohedral and cubic samples with δ=0.04 and 0.055 show distinct T_p, (T_p is the temperature corresponding to the resistivity peak for H=0 T) and a metallic behavior below this temperature. The magnetic ordering in nonstoichiometric $La_{1-\epsilon}MnO_{3+\delta}$ for $0.00 \leq \epsilon \leq 0.12$ is studied by Hauback et al. [36] using powder neutron diffraction method. They have reported three modifications of $La_{1-\epsilon}MnO_{3+\delta}$. First, the reduced ($0.00 \leq \epsilon \leq 0.08$) phase with JT deformed Mn^{3+} octahedra is orthorhombic (ORT1) and orders antiferromagnetically at ~140 K with μ_{AF} ~3.4 μ_B. All samples of this type exhibit a parasitic ferromagnetism. Second, the fully oxidized samples have a rhombohedral (RH) crystal structure with ferromagnetic ordering at low temperatures; For example in the case of $La_{0.96}MnO_{3.05}$, the Curie temperature and saturation moment are $T_c \simeq 213 \pm 10$ K and μ_F=3.9±0.1 μ_B respectively. Third, for intermediate oxygen contents (partially oxidised) an orthorhombic structure (ORT2) forms, with minor distortions of MnO_6 octahedra. For $LaMnO_{3.08}$ of ORT2-type, ferromagnetic order occurs below T_c=125±10 K and ordered magnetic moment μ_F=2.46±0.04 μ_B.

Ritter et al. [61] have established the magnetic behavior of $LaMnO_{3+\delta}$ for $0 \leq \delta \leq 0.15$. Th compounds with δ=0, 0.025, and 0.07 are orthorhombic in the temperature range of 1.5K - 320K. In the neutron thermo-diffractograms of the compound with $\delta = 0$, one can

notice the presence of extra magnetic peaks below T_N=140 K. This indicates the existence of long-range antiferromagnetic ordering For the compound with δ=0.025, antiferromagnetic peaks appears at the same positions as in the δ=0 sample at T_N = 110 K. However, the δ=0.025 compound also shows a ferromagnetic contribution to scattered intensity. The authors have attributed this result to a coexistence of ferro and antiferromagnetically ordered regions at low temperatures or to the existence of a canted spin structure for δ=0.025 compound. The refinement of the neutron diffraction data at the lowest temperature gives a value of 1.48 μ_B for the ferromagnetic component and of 2.52 μ_B for the antiferromagnetic component. For the δ=0.07 compound, the refinement of the low temperature spectrum yields a very small antiferromagnetic component of 0.25 μ_B. A large ferromagnetic contribution is observed below T_c=160 K, which reaches a value of 3.25 μ_B/Mn at the lowest temperature. For δ=0.1 compound, a small ferromagnetic contribution is observed below T_c=150 K. The compound with δ=0.15 contains the maximum oxygen content *i.e.* the largest number of La and Mn vacancies. The compound orders ferromagnetically, however the saturation moment is small. Since the neutron thermo-diffractogram of this compound does not show any peak due to antiferromagnetic ordering, the small value of the ordered moment can not be ascribed to spin canting The susceptibility plot of this compound shows a cusplike anomaly at T=50 K [61], also the magnetic irreversibilities observed in the field-cooled and zero-field-cooled magnetization meaurements suggest the existence of a disordered cluster-glass state.

(b) $La_{1-x}A_xMnO_3$, (A = Ca, Sr, and Ba)

The doped manganites exhibit a great variety of magnetic and transport properties that strongly depend on the stoichiometry and the structure of the material [9, 63-70]. Doping of the parent compound $LaMnO_3$ with divalent alkaline earth cations (A^{2+}), such as Ca^{2+}, Sr^{2+} or Ba^{2+} causes the conversion of a proportional number of Mn^{3+} to Mn^{4+}. The doped compounds in a certain range of composition show upon cooling both ferromagnetic (FM) and metallic behavior, together with CMR effect near the ferromagnetic ordering

temperature T_c [9, 63, 66] The Double Exchange (DE) mechanism was proposed by Zener [62] and other workers [71-72] to explain the simultaneous occurance of ferromagnetism and a metallic state in the doped compounds. In pure $LaMnO_3$, Mn^{3+}-O^{2-}-Mn^{3+} coupling is weakly ferromagnetic within an Mn-O plane and antiferromagnetic across the plane (type-A antiferromagnetism [2]) as mixed semicovalent and ionic exchange takes place in Mn^{3-}-O^{2-}-Mn^{3+} across a plane [35]. This is in contrast to $CaMnO_3$ or $SrMnO_3$ systems, where Mn^{4+}-O^{2-}-Mn^{4+} exchange is purely semicovalent (intraplane as well as interplane) and hence the coupling is antiferromagnetic with each Mn ion coupled to six nearest neighbors (type-G antiferromagnetism). Within the parent $LaMnO_3$ system, as Mn^{4+} concentration increases (or holes are doped at Mn^{3+}), strong ferromagnetic couplings develop in Mn^{3-}-O^{2-}-Mn^{4+} bonds as holes hop from Mn^{4+} to Mn^{3+} (or extra electron on Mn^{3+} travels back and forth between the two Mn ions) via O^{2-} with the lining up of local spins in parallelism which renders Mn^{3+}-O^{2-}-Mn^{4+} bonds metallic [Fig.1.9].

In recent works [73-75], it has been pointed out that in addition to the DE mechanism, a strong electron-phonon interaction arising out of the JT splitting of outer Mn d levels plays a crucial role in deciding the magnetic and electronic state of the material, especially at temperatures near and above T_c. Such an interaction is shown to have a strong effect in controlling the CMR.

The magnetic phase diagram of $La_{1-x}Ca_xMnO_3$ for $0<x<1$, over a broad range of temperature and field has been established by Schiffer *et al.* [9]. Structurally, there is
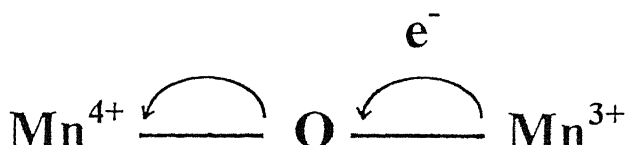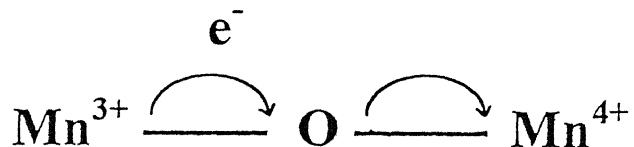
Figure 1.9: Double exchange mechanism in manganite system.

a complete solubility between $CaMnO_3$ and $LaMnO_3$. In its magnetically ordered state, the solid solution becomes metallic for $0.18 \leq x \leq 0.5$. For $0 \leq x \leq 0.1$ and $\delta > 0$, the material is ferromagnetic at low temperature ($T_c \sim 160$ K) but remains electrically insulating. The compound shows large negative magnetoresistance for Ca concentration x=0.20-0.45 where it is metallic. The magnetic behavior at low temperature changes from ferromagnetic insulator to antiferromagnetic insulator when the Ca concentration exceeds 50 percent [76]. At T_N, the inflection in $\rho(T)$ curve indicates the charge-ordering transition. The charge-ordering of Mn^{3+} and Mn^{4+} into two sublattices suppresses hole transfer and allows the system to enter an AFM state.

There are a large number of recent studies on electrical conduction and magenetic ordering in $La_{1-x}Sr_xMnO_3$ [10, 22, 77] system for $x \leq 0.4$ where a single phase is formed. For the case of $La_{1-x}Sr_xMnO_3$ as well, the substitution of Sr at La sites changes the Mn^{3+} ions to Mn^{4+} ions. This results in a ferromagnetic ground state with a Curie temperature T_c, which increases from 238 to 283 K with a small change in doping from x=0.15 to 0.175. This behavior is qualitatively explained in terms of the double exchange interaction between Mn ions as discussed before. The electronic phase diagram of $La_{1-x}Sr_xMnO_3$ has been summarized by Urushiba *et al.* [10]. Below the magnetic transition temperature, the phases can be divided into three regions; (i) the samples with small levels of Sr doping (x<0.1) are spin-canted antiferromagnetic insulator (CNI), (ii) for $0.1 \leq x \leq 0.15$ the material is ferromagnetic insulator (FI), and (iii) the system is a ferromagnetic metal (FM) with higher doping of Sr (x>0.15). On the other hand, above the magnetic transition temperatures (T_N and T_c) the electrical behavior changes from insulating to metallic around x=0.3.

A little is known about the magnetic phase diagram of Ba doped $LaMnO_3$. Dabrowski *et al.* [47] have reported the magnetic and electrical properties of Ba-substituted polycrystalline samples in the composition range x = 0.10-0.24 (in steps of Δx=0.02). The material orders ferromagnetically in the composition range x = 0.14-0.22. The magnetic transitions from the para- to the ferro- state are continuous and sharp for x = 0.14-0.22. Whereas, the

transitions for samples with x = 0.10 and x = 0.12 are less regular indicating the existence of a canted ferromagnetic state, similar to that observed for the $La_{1-x}Sr_xMnO_3$ compound with x = 0.125 [24] and $La_{1-x}Ca_xMnO_3$ with x ~ 0.1-0.2 [42] The magnetic transition for the x = 0.24 sample shows an additional increase of magnetization at ~335 K. The authors speculated the increase in magnetization is due to the presence of a small fraction of the x~0.3 phase at the Ba-solubility limit in the perovskite phase. With increasing x, the material shows a gradual transition from nonmetallic to metallic properties that are marked by a resistive anomaly at temperatures that correlate very well with the magnetic transition temperatures. A recent work on this materials by Chakraborty *et al.* [79] shows the insulator-to-metal transition at a relatively higher doping level (x≥0.2) than what is normally observed in the case of Sr or Ca substitution. However, the detail magnetic phase diagram over entire range of Ba doping (0≤x≤1) is lacking.

(c) $AMnO_{3-\delta}, \delta \geq 0$

As discussed previously, the crystallographic as well as the magnetic state of $AMnO_{3-\delta}$ is quite complex, and phenomenologically rich group of nonstoichiometric compounds can be derived from this perovskite structure [80]. The physical properties of these compounds depend on the nature of *A* cation and on the particular ordering of oxygen vacancies that affects the oxygen coordination of the transition metal ions.

In the case of $CaMnO_3$, early neutron diffraction measurements [2] show antiferromagnetic ordering at T_N = 110 - 130 K, and the paramagnetic susceptibility is consistent with the picture of a quenched orbital angular momentum and a high spin state with $S=\frac{3}{2}$ for the Mn^{4+} ions. Magnetic measurements below T_N indicate a Dzyaloshinsky type [81] parasitic ferromagnetism due to canting of Mn^{4+} spins [49]. While $SrMnO_3$ and $BaMnO_3$ have also been argued to order antiferromagnetically at low temperatures, neither compound shows the characteristic cusp in susceptibility, associated with the Neel ordering [59, 54]. For $BaMnO_3$, neutron diffraction measurements of Christensen and Olliver [59] performed at 77 K and 4.2 K show magnetic reflections whose intensity increases at 4.2 K. The authors

speculate that the system may have a partially ordered antiferromagnetic state below 150 K. The magnetic behavior of various polymorphic forms of $SrMnO_3$ and $BaMnO_3$ compound have not been studied atall. The electronic behavior of these compounds is also poorly understood.

1.1.4 Light Scattering and IR Absorption Studies on $La_{1-x}A_xMnO_3$

Despite a great deal of interest on magneto-transport and magnetic ordering in $La_{1-x}A_xMnO_3$ materials, surprisingly little work has been done on the studies of phonon modes in these systems. The local coordination of Mn ions in the doped materials has been probed with X-ray absorption spectroscopy and extended X-ray absorption fine structure measurements [8, 82]. Some information about optical phonons in Ca- and Sr- doped lanthanum manganite has been inferred from measurements of infrared (IR) reflectivity [83-86]. The first report related to the Raman scattering study of the doped $La_{1-x}A_xMnO_3$ compound [87] did not show any signature of optical phonon modes present in this system. One of the possible causes of this absence could be due to the detection system (*i.e.* photomultier tube) used in this experiment, which is not sensitive enough for the detection of weak signals. Other possible reason is the small penetration depth of the excitation radiation as well as a pseudocubic symmetry of doped $La_{1-x}A_xMnO_3$ materials, both of which result in an extremely weak Raman scattering signal. The Raman active phonon modes in the orthomanganites have been studied very recently (in parallel with our studies) by Iliev *et al.* [88] and by Podobedov *et al.* [89]. Yoon and coworkers [90] and Granado *et al.* [91] have shown various Raman active modes in undoped as well as Ca, Sr and Pb doped manganites, the detection system for all those experiments consisted of liquid nitrogen cooled charge-coupled device (CCD), which is sensitive enough to detect even a single photon.

Raman Studies on Undoped $LaMnO_{3+\delta}$

The Raman active phonon modes in the orthorhombic $LaMnO_3$ have been investigated for various scattering configurations at room temperature [88] and also with the variation of

temperature [89]. Orthorhombic $LaMnO_3$ belongs to the space group D_{2h}^{16} (Pbnm) with four formula units in the cell [15, 92-93]. Invoking the crystal symmetry and Wyckoff sites occupied by different ions, the factor group analysis yield the following optical vibrational modes for the orthorhombic $LaMnO_3$:

$$7 A_g^{RS} + 5 B_{1g}^{RS} + 7 B_{2g}^{RS} + 5 B_{3g}^{RS} + 8 A_u + 9 B_{1u}^{IR} + 7 B_{2u}^{IR} + 9 B_{3u}^{IR}.$$

Of the total 60 Γ-point phonon modes, 24 are Raman active modes ($7 A_g + 5 B_{1g} + 7 B_{2g} + 5 B_{3g}$).

Oxygen rich $LaMnO_{3+\delta}$ can exist in two symmetries *viz.* rhombohedral and cubic depending on the value of δ. The factor group analysis for the rhombohedral symmetry D_{6d}^6 ($R\bar{3}c$) with two formula units in the cell for $LaMnO_{3+\delta}$ [44, 94] yields the following optical vibrational modes :

$$A_{1g}^{RS} + 2 A_{1u} + 3 A_{2u}^{IR} + 4 E_g^{RS} + 5 E_u^{IR} + 3 A_{2g}.$$

Out of these, A_{1g} and $4 E_g$ are Raman active phonons. Iliev *et al.* [88] reported the room temperature Raman spectra of rhombohedral $LaMnO_3$ showing broad peaks at 220, ~490 and ~610 cm^{-1}. However, the last two peaks are not observed in the measurements of Granado *et al.* [91] from the fresh surfaces of rhombohedral samples. They argue that the spectra reported for the rhombohedral $LaMnO_{3+\delta}$ by Iliev *et al.* [88] may be due to orthorhombic distortions present in the samples We started Raman measurements on Ba doped manganites in parallel with the work of Iliev *et al.*. Our measurements of both orthorhombic and rhombohedral $LaMnO_{3+\delta}$ samples are in good agreement with the results of Iliev *et al.* [88]. These results will be discussed in the subsequent Chapters.

For the cubic symmetry $LaMnO_{3+\delta}$ which belongs to space group O_h^1 (m3m) with one formula unit in the primitive cell [84, 95], the group theory does not allow any first order Raman active modes. The vibrational phonon modes for this system are;

$$3 F_{1u}^{IR} + F_{2u}.$$
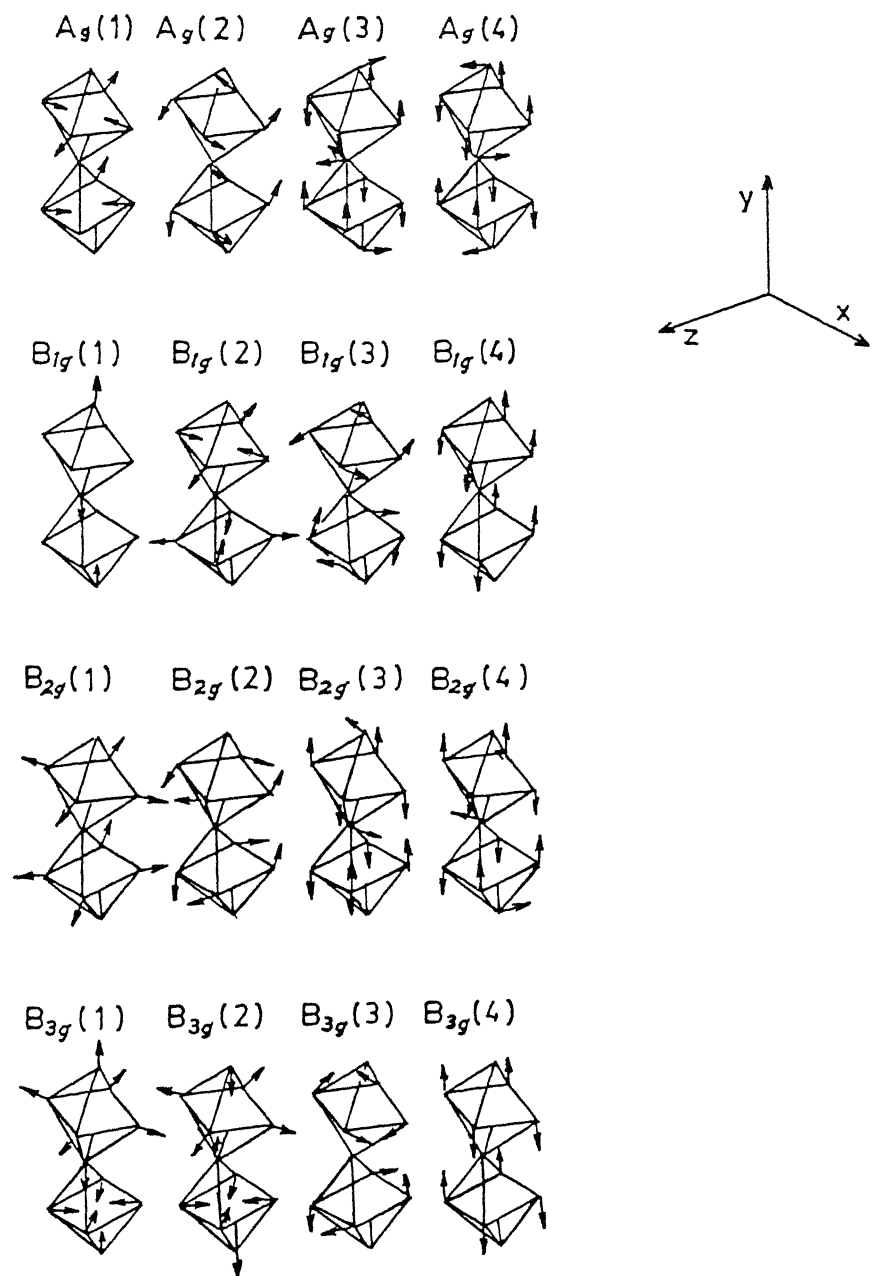
Figure 1.10: Raman allowed phonon modes for ABO_3 compounds with Pbnm or Pnma structure [88].

The temperature dependent polarized Raman spectra from undoped and Sr and Ca doped $LaMnO_3$ single crystals are reported by Podobedov et al. [89]. Their Raman spectra from the undoped $LaMnO_3$ structure distorted by the static JT effect are consistent with the orthorhombic D_{2h}^{16} space group The observed frequencies are centered at 96, 142, 149, 210, 260, 333, 450, 484, 493, 609 and 675 cm^{-1}. One of the interesting observations of this work is the additional band at 675 cm^{-1} that is usually stronger in z-axis related geometries, exhibits a weak polarization dependence. The above features are also observed in the spectra of the doped materials, and have been attributed to the second-order Raman processes. Another important finding of this work is the anomalous behavior of a low frequency band (~ 309 cm^{-1}) with the variations in the type and concentration of the dopant ion. The low frequency band shows a large shift (more than 50 cm^{-1}) as the doping increases from 0.1 to 0.3 and also by changing the dopant from Ca to Pb. The anomaly of the low frequency band is due to the nature of interaction between La/A ions and MnO_6 octahedra. The increase of ionic radius of A atom strongly effects the force constant in $La/A-MnO_6$ vibrational system. This effect explains the corresponding change in the Raman shift of the related low frequency mode. The most remarkable observation of the work by Podobedov et al. [89] is the anomalous behavior of the strongest mode (~ 609 cm^{-1}) in the temperature range 100-140K This mode shows an abrupt frequency shift near ~ 140 K which corresponds to the Neel temperature of the system. Podobedov et al. have explained this observation in terms of spin-lattice interaction, which arises from the stabilization energy required to bring the MnO_6 octahedra to a particular structural configuration. This stabilization energy is determined by the relative orientation between the Mn spins of near-neighbor MnO_2 planes. With the magnetic transition from para to canted antiferro in $LaMnO_3$, the MnO_6 octahedra change accordingly in response to the antiferromagnetic ordering of the Mn spins.

The studies of infrared spectra on the orthomanganites were reported for the first time by Subba Rao et al. [96]. The spectra of a few $RMnO_3$ (R=La, Pr, Nd, Ho, Yb and Y) are compared with those of Mn_2O_3. All the orthomanganites show absorption bands
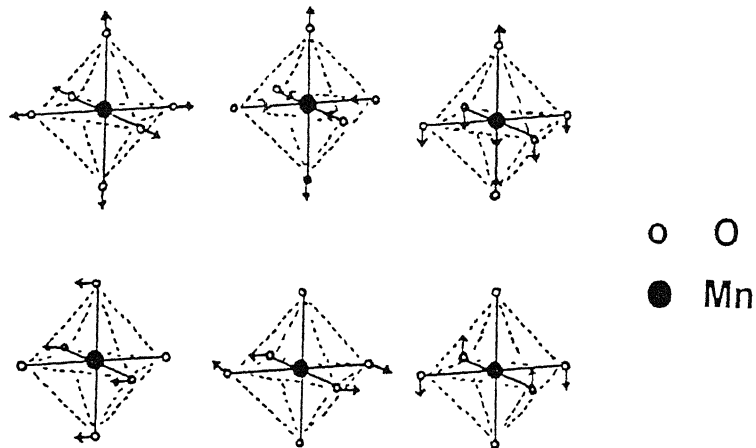
Figure 1.11: Normal modes of vibration of octahedral MnO_6 molecules.

which are generally broader than those of the chromites. There are no major bands in the region 4000-800 cm^{-1} but several characteristic bands are observed in the 700-200 cm^{-1} region. The more intense bands in the 670-500 cm^{-1} region are expected due to the Mn-O stretching modes. The shoulder at ~620 cm^{-1} in Mn_2O_3 appears as a shoulder in the lighter manganites but becomes a well defined band in the heavier rare earth manganites. The strong broad band ~608 cm^{-1} of Mn_2O_3 is observed at ~590 cm^{-1} in all the manganites.

The infrared transmission spectra of polycrystalline $La_{1-x}Ca_xMnO_3$ system over a wide range of concentration at room temperature have been reported by Li *et al.* [86]. Two strong absorption peaks located around 600 and 350 cm^{-1} are observed which are characteristic bands of ABO_3 perovskite oxides [96-99]. These peaks are associated with the internal phonon modes *i.e.* stretching and bending modes of the MnO_6 octahedra. The octahedral MnO_6 belongs to space symmetry O_h^6. For this seven atom-molecule, six vibrating modes [100] are illustrated in Fig.1.11, where the first three modes are stretching modes and the other three are bending modes, but only two of them (ν_3 and ν_4) are IR activated.

The temperature dependent reflectivity spectra of $La_{0.7}Ca_{0.3}MnO_3$ compounds are reported by Kim *et al.* [84]. The spectra consist of three main phonon bands located at 70, 330 and 580 cm^{-1}. The F_{1u} phonon modes are called external, bending or stretching

modes depending on the types of collective motions. The external mode, located at ~ 70 cm^{-1} represents vibrating motion of the La(Ca) ions against the MnO$_6$ octahedra. The bending mode located at 330 cm^{-1}, reflects an internal motion of the Mn and O ions located along a particular direction against the other oxygen ions in a plane perpendicular to the direction. This mode is strongly affected by a change of the Mn-O-Mn bond angle. The stretching mode located near 580 cm^{-1} corresponds to an internal motion of the Mn ion against the oxygen octahedron, and is sensitive to the Mn-O bond length [83] The internal phonon modes of MnO$_6$ octahedra in this compound show a significant frequency shift near the Curie temperature.

1.2 Focus of the Present Work

The review of the literature in the preceeding sections indicates that the charge, spin and orbital degrees of freedom in the perovskite manganites R$_{1-x}$A$_x$MnO$_3$ lead to a rich variety of physical phenomena. Amongst the family of $R_{1-x}A_x$MnO$_3$, the Ca and Sr doped materials have been studied extensively and these two systems show considerable variance in their properties owing to the difference in the ionic radius of the divalent dopant. The divalent metal Ba, because of its much larger ionic size compared to the ionic radius of Sr or Ca, is expected to distort the perovskite cell much more strongly and therefore affects all physical properties of the system. The key focus of this thesis is to study the phase stability, lattice vibrations and magnetic behavior of La$_{1-x}$Ba$_x$MnO$_3$ system. In order to provide a better understanding of the correlation between atomic structure and physical properties, we have utilized two principal spectroscopic techniques *viz.* Raman and infrared absorption spectroscopy to study the lattice dynamics of the Ba doped lanthanum manganites. The granularity, structural as well as magnetic, seem to play an important role in electronic transport in these systems, particularly the spin polarized transport. The Ba-doped materials also provide a unique granular system in a certain composition range. We have carried out the magnetic measurements on all the samples over a wide range of temperature and magnetic field strength in order to establish the ordering of Mn^{3+} and

Mn^{4+} spins on a local and global scale. The specific objectives of this thesis are as follows:

1. To study the formation of different crystallographic phases and their characteristic Raman and infrared spectra in the manganite system $La_{1-x}Ba_xMnO_3$ for x in the range of $0 \leq x \leq 1$.

2. To study the behavior of Raman active phonon modes of the Jahn-Teller distorted cubic perovskite $LaMnO_3$ and to establish the changes in these modes as the distortion is gradually removed with excess oxygen.

3 To establish the critical Ba concentration beyond which the perovskite cell becomes unstable.

4. To establish the effects of oxygen disorder and vacancies on the IR and Raman active modes of the compound $BaMnO_3$.

5. To study the onset of ferromagnetism in Ba substituted $LaMnO_3$ and elucidate the influence of ionic size on the ordering temperature.

6. To establish the magnetic state of the two-phase region and study magnetic granularity of the material.

7. To study the influence of magnetic ordering on the local atomic arrangement through studies of the temperature dependence of the Raman active phonon modes in JT distorted $LaMnO_3$ and various hexagonal polymorphic forms of $BaMnO_3$ compounds.

1.2.1 Organization of the Thesis

The rest of the thesis is organized as follows : Chapter 2 deals with the description of the experimental techniques used in this work, which is followed by the details of the sample chracterizations in Chapter 3. Various crystallographic phases that are formed in the Ba doped $LaMnO_3$ for wide composition range of Ba are also discussed in this Chapter.

Chapter 4 presents the results of Raman and infrared spectroscopy measurements on the $La_{1-x}Ba_xMnO_3$ system. The appearance of a hexagonal $BaMnO_3$ phase in the

background of cubic $La_{0.65}Ba_{0.35}MnO_3$ for $0.35 \leq x < 1$ is discussed and compared with the XRD results. A brief outline of the factor group analysis of zone-center vibrations for all the structural symmetries of these materials is presented in this Chapter. The behavior of various vibrational modes in $La_{1-x}Ba_xMnO_3$ compounds is discussed in the framework of group theory. The controversy regarding the correct space group for $BaMnO_3$ (2H) is resolved through systematic studies of Raman and IR spectra of this compound.

In Chapter 5, the magnetic behavior of $La_{1-x}Ba_xMnO_3$ is discussed. The magnetic ordering effects in the two end members of this series are reinvestigated. The magnetic behavior of the single and two-phase Ba doped compounds is also established. Magnetic granularity, superparamagnetism and an effective medium approach for the susceptibility of the two-phase mixture are also presented in this Chapter.

Chapter 6 deals with the low temperature lattice dynamic study of lanthanum barium manganites. This Chapter addresses the behavior of phonon modes at the magnetic ordering temperature. The temperature dependence of the frequency and linewidth of various Raman active modes are discussed in the framework of anharmonicity in vibrational potential energy of the lattice.

Chapter 7 summarizes the results of the present work.

Chapter 2

Experimental Techniques

2.1 Introduction

An overview of various experimental techniques used to study the crystallographic and magnetic phases and phase transformations in the barium doped lanthanum manganite system is given in this Chapter. Emphasis is also placed on the sample preparation technique since the properties of these manganites are highly sensitive to processing conditions such as temperature and oxygen partial pressure. Since the optical scattering cross section of the manganites, particularly of the metallic phases, is quite low special care had to be taken while collecting the Raman scattering data. Various sample characterization techniques such as powder X-ray diffraction (XRD), infrared absorption (IR) and scanning electron microscopy (SEM) are also described. For the measurements of magnetic moment, techniques such as vibrating sample magnetometry (VSM) and Superconducting Quantum Interference Device (SQUID) magnetometry have been used. The details of these experiments are formulated briefly.

2.2 Method of Sample Preparation

The perovskite manganite materials studied in the present work qualify as electrical and magnetic ceramics. There are several techniques available for preparation of such ceramics. Some of the commonly used techniques are as follows;

1. Solid state reaction method or ceramic technique.

2. Solution technique, which comprises of

   - Co-precipitation method

   - Sol-gel method

   - Freeze drying method

   - Co-decomposition method.

3. Crystal growth technique like floating-zone method.

4. Various thin film growth techniques such as laser ablation, sputtering, chemical vapour deposition *etc.*

For the present studies, samples were prepared by the standard solid state reaction method. The critical steps involved in preparation of manganite samples with this technique are described as follows;

2.2.1 Calcination

The oxides, carbonates or hydroxides of the relevant metals are first weighed to achieve the desired metal ion stoichiometry and then mixed properly in an agate mortar in order to achieve homogeneity. This initial decomposition of stable starting powders, by heating below their melting point is known as calcination. The powders to be calcined are not normally pressed to ensure easy escape of CO_2 and moisture. The compound forming reaction does not go to completion in one step partly owing to small contact areas at

interfaces between grains. Repeated mixing, pressing and grinding are required to form a homogeneous sintered product.

2.2.2 Pelletization

Pellets are made by applying axial pressure with a hydraulic press to powder in a die. The effects of the pressure are; (i) a reduced pore size, (ii) break up of particles especially at surfaces in contact, and (iii) introduction of strain and plastic flow. Often microscopic pressure gradients developed across the pellet during the pelletization tend to produce cracking, and hence the value of pressure must be optimized. The pellets are placed on chips or powder of the same material to avoid contamination from underlying brick during firing. Cracks, introduced by inhomogeneous compression, tend to grow during sintering for reasons of stress relief.

2.2.3 Sintering

In sintering, the grains in adjacent particles react and bound. In ceramic systems, the reaction generally occur at the interfaces between different phases and are therefore heterogeneous. Repeated grinding, mixing and re-sintering are done to make a reaction to go for completion so as to form a single phase. Surface contact between particles is maximized by pressing the powder before sintering. The dominant physical factor controlling sintering is temperature. In traditional ceramics a typical sintering temperature is three-quarters of the melting temperature expressed on the absolute scale.

2.2.4 Methodology for $La_{1-x}Ba_xMnO_3$ samples :

The starting material, La_2O_3 (99.9%), $BaCO_3$ (99.9%), and Mn_2O_3 (99.9%) from Aldrich Chemicals USA taken in stoichiometric proportions were thoroughly mixed in a motorized agate mortar. The powder was then calcined at $1000^{\circ}C$, reground and calcined again three times following the same steps. The calcined powder was then pelletized in the form of 3 and 6 mm diameter discs. These discs were annealed in air at $1200^{\circ}C$ and in some cases at $1350^{\circ}C$ for 5 hr., in oxygen at $1100^{\circ}C$ for 8 hr. and finally cooled to room temperature

in flowing oxygen at a rate of 2^oC/min. In order to minimize δ in samples of $LaMnO_{3-\delta}$, a separate set of samples was synthesized by carrying out the calcination and annealing steps described previously in flowing argon gas (99.99%) environment. These samples were then oxygenated at several temperatures in the range of 600-1100 °C.

In $BaMnO_{3-\delta}$ samples, the oxygen concentration was varied by quenching the oxygen rich stoichiometric $BaMnO_3$ from various temperatures *e.g.* 1400, 1320, and 1200^oC to room temperature in air. A set of $BaMnO_{3-\delta}$ samples with different δ was synthesized by performing all the annealings *viz.* calcinations and sintering in the environment of argon gas (99.99%). The equations of chemical reaction for $LaMnO_3$, $BaMnO_3$ and $La_{1-x}Ba_xMnO_3$ compounds are given below :

$$\frac{1}{2}La_2O_3 + \frac{1}{2}Mn_2O_3 \rightarrow LaMnO_3 \tag{2.1}$$

$$2BaCO_3 + Mn_2O_3 + \frac{1}{2}O_2 \rightarrow 2BaMnO_3 + 2CO_2 \tag{2.2}$$

$$\frac{1-x}{2}La_2O_3 + xBaCO_3 + \frac{1}{2}Mn_2O_3 \rightarrow La_{1-x}Ba_xMnO_3 + CO_2 \tag{2.3}$$
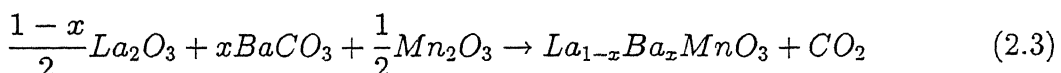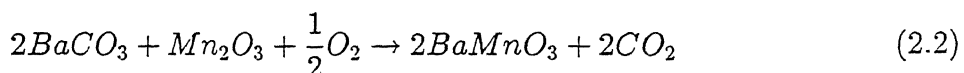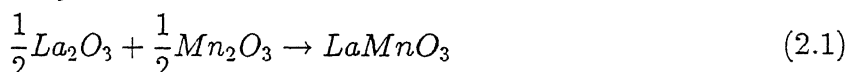
In $LaMnO_{3+\delta}$ compound, the oxygen nonstoichiometry δ is not simply oxygen excess rather metal-ion vacancies [38]. The defect chemistry of this material is scanty. Incorporation of oxygen excess in $LaMnO_{3+\delta}$ coincides with the formation of La and Mn vacancies in combination with the partial charge disproportionation of Mn^{3+} into Mn^{2-} and Mn^{4-} [101]. The average Mn valency in excess of 3+ can be estimated from wet-chemical redox titration. In some cases the overall Mn^{4+} content is used as a measure of the nonstoichiometry.

2.3 Sample Characterization Techniques

The techniques used for characterization of the samples include (i) X-ray diffraction measurement (XRD), and (ii) Scanning electron microscopy (SEM). These techniques are described in the following;

Table 2.1: Operating parameters of X-ray diffractometer

Electron beam voltage and current	30 kV, 20 mA
Detector scanning speed (SS)	0.6 °/min.
Chart speed (CS)	0.6 cm/min.
Counts per min. (CPM)	5 k
Time constant (TC)	10 sec.

2.3.1 XRD Measurements

The powder X-ray diffraction technique has been used to analyze the crystallographic phases present in the sintered pellets and to determine their crystal structure and lattice parameters. The XRD measurements were carried out using a $(\theta - 2\theta)$ X-ray diffractometer (Rich Seifert Iso-Debyeflex 2002, Germany). This instrument had a CuK_α source (λ=1.5418Å) and a Ni foil monochromator. The typical XRD scan parameters used are listed in Table 2.1.

Sintered pellets are powdered to reduce the effects of preferential orientations in the scattering intensity. The powdered sample is spread evenly on the surface of a glass slide. A few drops of methanol are added in the powder so that it sticks to the glass slide. The XRD plots are recorded in a 2θ range of $20°$ to $70°$. The 2θ values corresponding to the position of diffraction peaks are noted and the interplanar spacing d is calculated using the Bragg's law

$$n\lambda = 2dsin\theta \qquad (2.4)$$

where n is the order of diffraction, λ is the X-ray wavelength, and θ is the diffraction angle. The relative intensities of the peaks are also measured relative to the most intense peak whose intensity was assumed to be 100. The calculated 'd' values and the corresponding relative intensities are compared with the standard powder diffraction data (powder diffraction file). The diffractometer was calibrated using high purity silicon powder as standard.

Determination of Lattice Parameters

For cubic system the lattice parameter (a) has been calculated from the following equation for the interplanar spacing;

$$\frac{1}{d_{hkl}^2} = \frac{h^2 + k^2 + l^2}{a^2} \tag{2.5}$$

where d_{hkl} is the interplanar distance and a is the lattice parameter.

For rhombohedral system the (110) and (006) planes have been used to determine the lattice parameters. If h, k, l are the Miller indices of rhombohedral system then the corresponding indices for the hexagonal system are given by the following equations

$$H = h - l$$

$$K = k - l \tag{2.6}$$

$$L = h + k + l$$

For hexagonal system one can write [102]

$$sin^2\theta = \frac{\lambda^2}{4} \left[\frac{4(H^2 + HK + K^2)}{3a_H^2} + \frac{L^2}{c_H^2} \right] \tag{2.7}$$

where a_H and c_H are the hexagonal lattice parameters. Now knowing at least two sets of (H, K, L) values and corresponding Bragg's angle the values of the lattice parameters can be determined.

The rhombohedral lattice parameters are determined from the following equations

$$a_R = \frac{1}{3}\sqrt{3a_H^2 + c_H^2} \tag{2.8}$$

$$sin(\frac{\alpha}{2}) = \frac{3}{2\sqrt{3 + (c_H/a_H)^2}} \tag{2.9}$$

For orthorhombic system, the basic equation governing the $sin^2\theta$ values is

$$sin^2\theta = Ah^2 + Bk^2 + Cl^2 \tag{2.10}$$

where the three unknown constants A, B, and C are related to the λ and lattice parameters a, b, and c as;

$$A = \frac{\lambda^2}{4a^2}, \qquad B = \frac{\lambda^2}{4b^2}, \qquad and \qquad C = \frac{\lambda^2}{4c^2} \qquad (2.11)$$

Considering any two lines having the same hk values one can solve Eq.(2 10) to obtain value of C and accordingly c. Then taking θ values of two lines having the same kl one can obtain a, similarly b can also be calculated using Eqns.(2.10 and 2.11).

2.3.2 Scanning Electron Microscopy (SEM) Measurements

Microstructure observations like the presence of cracks, voids etc. in the samples as well as measurements of grain size have been done using a scanning electron microscope (JSM 840 A, JEOL, Japan). Scanning electron microscopy primarily involves imaging of secondary electrons which are emitted from the sample when a beam of energetic electrons hits it. The energy distribution of the secondary electrons is sharply peaked at low energies of below a few eV, and can be used to examine the topography of a sample. The slow secondary electrons are extracted by a high potential applied to a scintillation detector system and secondary electron images are generated by synchronizing the optical output of the detector system with raster of the electron probe across the sample. The insulating sample could not be directly observed under SEM due to charging effects. For this purpose, the sample surface was coated with a thin layer of silver. The SEM photos were generally taken under two magnifications, one at high and another at low. The low magnification ($\sim$ 500) gave overall picture of the surface of the sample while the high magnification ($\sim$ 15, 000 or 30, 000) pictures were used to calculate grain size. The typical operating conditions of the SEM are given in Table 2.2.

Table 2.2: Typical operating parameters of SEM study

Accelerating voltage	10-15 kV
Beam current	0.3 nA
Working distance	7-15 mm
Magnification	200 to 50, 000 times
Mode of imaging	Secondary electrons

2.4 Magnetization Measurements

Magnetization measurements of all the samples as a function of temperaure and applied magnetic field were performed using the following commercial magnetometers :

- Quantum Design SQUID magnetometer MPMS-system.

- Quantum Design extraction magnetometer PPMS-system.

- Vibrating sample magnetometer (VSM).

Quantum Design's magnetic property measurement system (MPMS) and physical property measurement system (PPMS) are highly integrated instrument systems designed to be a primary research tool for study of magnetism in matter. The MPMS system includes several different superconducting components :

- a superconducting magnet to generate large magnetic fields

- a superconducting detection coil which couples inductively to the sample

- a superconducting quantum interference device (SQUID) connected to the detection coil

- a superconducting magnetic shield surrounding the SQUID.

2.4.1 SQUID Magnetometer

A SQUID is the most sensitive device available today for measuring magnetic fields. However, it does not detect directly the magnetic field from the sample. Instead, the sample moves through a system of superconducting detecting coils which are connected to SQUID with superconducting wires, allowing the current from the detection coils to inductively couple to the SQUID sensor. When properly configured, the SQUID electronics produces an output voltage which is strictly proportional to the current flowing in the SQUID input coil. Hence, the thin film SQUID device, which is located approximately 11 cm below the magnet inside a superconducting shield, essentially functions as an extremely sensitive current to voltage convertor.

2.4.2 Vibrating Sample Magnetometer (VSM)

A vibrating sample magnetometer is a device in which the sample is vibrated in a uniform magnetizing field, and the magnetization of the sample is detected with a set of pickup coils. It allows precise magnetization measurements to be made as a function of temperature, magnetic field strength, and crystallographic orientation. However, the sensitivity of this technique is much smaller than that of a SQUID magnetometer. The VSM used in the present study is from Princeton Applied Research model PAR-150A with a dc field capability of 1.8 Tesla. The block diagram of the VSM is shown in Fig.2.1.

When a specimen is placed in a uniform magnetic field, a magnetization M is induced in the sample equal to the product of the susceptibility χ and the applied magnetic field H *i.e.*

$$M = \chi H. \tag{2.12}$$

If the sample is vibrated, say in a sinusoidal motion, an electrical signal due to the magnetization of the sample can be induced in stationary pick-up coils placed in a suitable position. The elctrical signal is proportional to the magnetic moment, the vibrational amplitude, and the vibrational frequency. The electronic system is designed so that variations in the
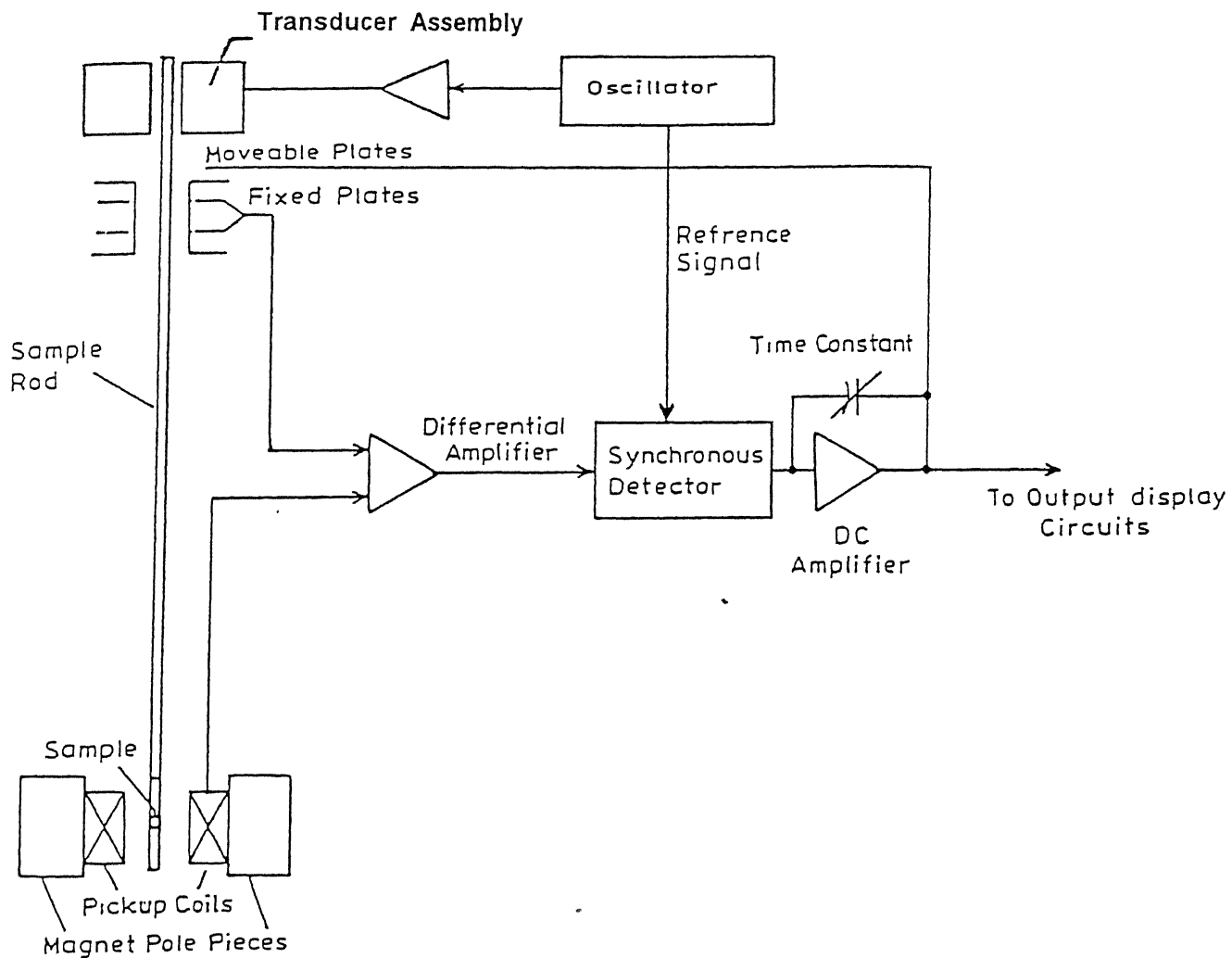
Figure 2.1: Schematic block diagram of the vibrating sample magnetometer.

amplitude and frequency of vibration are accounted for, and a signal proportional only to the magnetization of the sample is monitored and displayed as sample magnetization. The VSM measures the total magnetic moment of the sample in electromagnetic units (emu).

VSM measurements were performed on 3 mm diameter pellets placed in a boron nitride sample holder. The temperature variation of magnetization was studied using a furnace assembly (model 151) associated with the magnetometer, which could provide a temperature upto 973 K. The sample temperature during measurements was controlled using a programmable temperature controller. The furnace chamber was evacuated using rotary and diffusion pumps during the process of heating.

2.5   Infrared Absorption

Infrared transmission measurements on all the samples were carried out using three different IR spectrometers. These are;

1. Fourier-Transform IR Nicolet spectrometer for the spectral range 400-4000 cm^{-1}.

2. PERKIN ELMER 783 spectrophotometer for the spectral range 300-4000 cm^{-1}.

3. Shimadzu IR-420 spectrophotometer for 400-4000 cm^{-1}.

The samples for IR transmission measurements were prepared by thoroughly mixing the finely ground powders of the manganites with dry KBr (or CsBr). The mixture was then pressed into transparent pellets of 0.5 mm thickness. Since factors such as particle size, refractive index of the bromide matrix, adsorption, chemical reaction and mixed crystal formation *etc.* affecting the sample spectra [103, 104] taken using this method, care was exercized in the interpretation and analysis of the data.

2.6   Raman Spectroscopy

The experimental setup for Raman measurements mainly consists of;

- **Excitation source :** Spectra Physics 5 Watt (all line) Ar^+ laser.
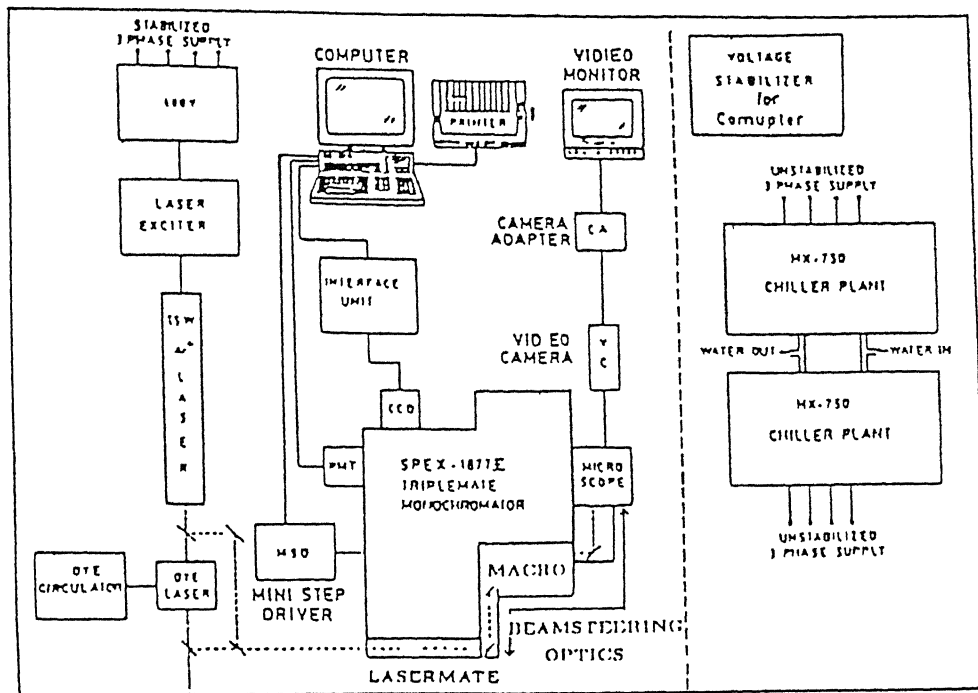
Figure 2.2: Schematic block diagram of the Raman setup with 180° scattering configuration.

- **Spectrometer** : Spex 1877 E Triplemate with two scattering configurations (90° and 180° geometries).

- **Detection system** : Charged coupled device (CCD) and photomultiplier detector.

- **Low temperature stage** : CTI-CRYOGENICS 8200 helium compressor and model M-22 Cryotip, and Lake Shore model 805 temperature controller.

A schematic diagram of the Raman setup with 180° scattering configuration is shown in Fig.2.2.

2.6.1 Excitation Source

The excitation source used for the Raman scattering measurements of the present work is a Spectra Physics model 165 (5 Watt) Ar^+ laser which comprises of model 265 exciter and NESLAB HX 500 chiller plant.

Table 2.3: Performance specification chart of 5 Watt Ar$^+$ Laser

Specifications	5 Watt Ar$^+$ Laser
Beam diameter	1.25 mm
Beam divergence	0.69 mrad
Cavity length without prism	1.00 m
with prism	1.05 m
Polarization	Vertical
Mode spacing without prism	149.6-150.5 MHz
with prism	142.5-143.3 MHz
Input power	3 phase with ground
phase-to-phase voltage	400 ± 8%
Current	38 A
Watts	13.1 kW
Water flow rate	8.4 lit/min.
Water pressure	30 psi

Ar$^+$ Laser

Spectra Physics model 165 (5 Watt) Ar$^+$ laser consists of a laser head [105] and model 265 exciter [106]. The laser head contains a plasma tube of Beryllium oxide (closed at both ends by Brewster's angle windows), a solenoid, an optical resonator formed by a spherical reflector at the output end and a prism (to select wavelength) assisted by a flat mirror at the back end. With a start boost circuit (by 7 kV pulse), the exciter generates an initial discharge in the plasma tube. This exciter contains a regulated power supply that controls the ion discharge current in the plasma tube to provide constant laser performance. The electrical and water requirements of this laser and its optical characteristics are summarized in Table 2.3. The operating wavelength and power ratings of this laser are given elsewhere [105]. For scattering experiments on the manganite compounds the excitation wavelengths $\lambda_{excitation}$ used were 514.5 and 488 nm laser lines.

A chiller unit NESLAB HX 500 with a cooling capacity of 15.7 kW is used to cool the

laser head and the exciter electronics. The unit provides a continuous flow of deionized water at constant temperature (20° C) and pressure (30 psi) to the laser head. The self contained unit consists of a stainless steel reservoir, temperature controller, recirculating pump and refrigeration system. The temperature stability is $\pm 0.1^o$ C. The deionized water is cooled by the refrigerator coils immersed in it. It is circulated in a closed loop by the pump. The compressor is water cooled from an external tap.

2.6.2 Spectrometer Setup

The spectrometer setup for Raman measurement comprises of; (a) Tunable excitation filter (lasermate), (b) 1482 D Micromate (Micro-Raman illuminator), (c) the collection optics and (d) Spex 1877 Triplemate.

(a) Lasermate

The 1450 Tunable excitation filter is a compact grating monochromator used to eliminate plasma emissions from incident visible laser before the light passing through beam steering optics enters the 1482 D micromate and is focused onto the sample [107]. The specifications of the lasermate are given in Table 2.4.

Table 2.4: Specifications for Lasermate

Aperture	3 mm
Wavelength range	200 to 633 nm
Grating	1200 gr/mm (12.7 mm × 12.7 mm)
	blazed at 500 nm
Efficiency	50 % at grazing blaze
Exit slit	120 μm
Bandpass	0.5 nm
Power input	6 W maximum

(b) Micro-Raman Illuminator

This provides a way to isolate the sample area with dimensions as small as 2 μm for study [108]. The sample is kept on the microscope platform where the laser beam is focused onto the sample. The Spex 1482 D Micromate equipped with a video camera and with 40X and 10X microscope objectives is used for sample viewing (video monitoring) in backscattering configuration. The illumination source supplies incident radiation and the reflected light from the sample goes to CCTV camera. Whenever micromate's internal selection mirror is positioned to stear an image of the sample on to the camera, a neutral density filter automatically intercepts and attenuates the beam to reduce the risk of damage to the camera. When the neutral density filter is not in place, a quartz blank replaces it to preserve optical alignment.

(c) The Collection Optics

The scattered intensity from the samples has been collected using 90° and 180° scattering geometries. The collection optics in 90° scattering configuration [as shown in Fig.2.3(a)] is based on a segment cut from an all reflecting ellipsoidal mirror. As such, its reflection is based on the geometrical properties of an ellipsoid. The mirror is positioned so that the sample is at one focus of the ellipsoid, and the entrance slit of the spectrometer at the second.

In 180° scattering geometry the laser light is focused onto the sample using a lens and a plane mirror system [Fig.2.3(b)] and the scattered radiation is collected in the reversed direction. The Spex 1482 D Micromate supplies a way to focus the laser onto the sample and collects the back-scattered radiation to the entrance slit of the monochromator. The major advantage of back-scattering geometry is that once the whole system is properly aligned, one simply has to place the sample at the instrument focus. Another advantage is that, as the incident light could be focused down to a spot of diameter $\sim$ 2-3 μm, this in conjuction with a video image of the sample topography, allowed studies of the variations in the spectral content from grain-to-grain.
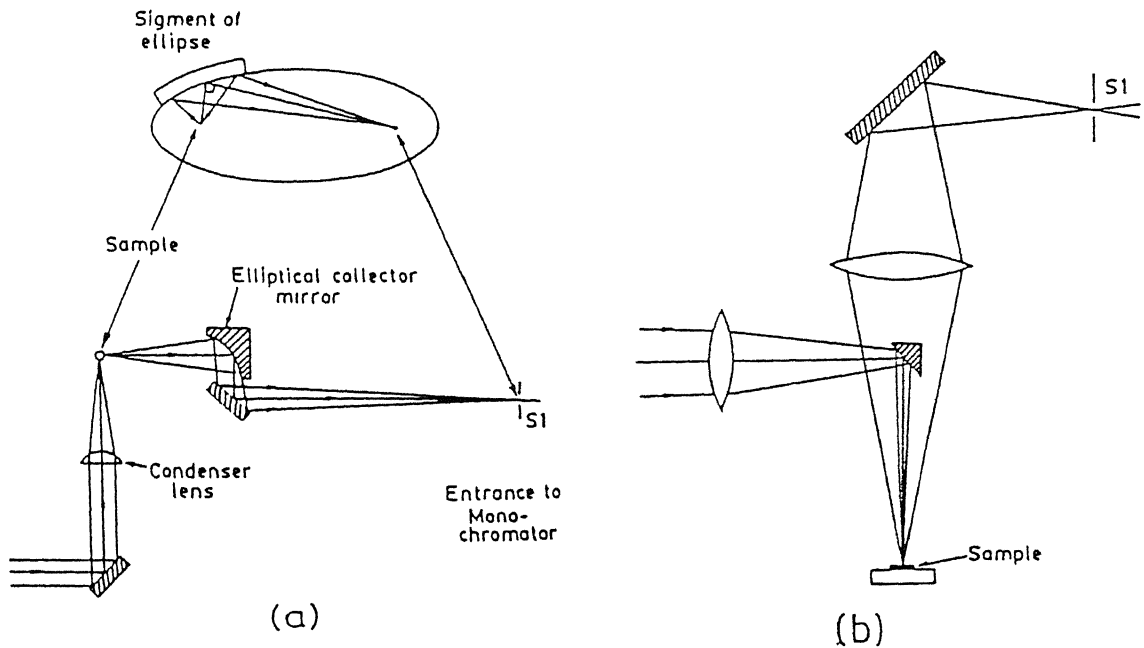
Figure 2.3: Collection optics in (a) the 90° and (b) 180° scattering configurations. The inset in (a) displays the foci (S and S_1) of the ellipsoid mirror.

(d) Spex 1877 E Triplemate

Raman monochromators are specially designed to provide low stray light and flat undistorted focal plane, ideal for sensitive work. The Spex 1877 E triplemate is a spectrograph specially tailored to provide the above specifications successfully [109]. The triplemate has two main sections *i.e.* the filter and spectrograph stages. The filter stage consists of two modified Czerny-Turner 50 mm × 50 mm plane gratings having 600 grooves/mm, coupled in a subtractive mode, and giving a bandpass of about 1100 cm^{-1} on a 5 mm intermediate slit setting. The focal length of the stage is 0.22 m. It acts as a variable wavelength, selectable bandpass filter that feeds a non-dispersed segment of radiation from a sample into the entrance slit of the spectrograph stage. The spectrograph stage is a 0.6 m, single monochromator which disperses the radiation over the detector. It consists of an asymmetric Czerny-Turner mount with a 64mm × 64 mm plane grating having 1200 grooves/mm and is used to produce a dispersion of 1.4 nm/mm. To vary the dispersion and spectral
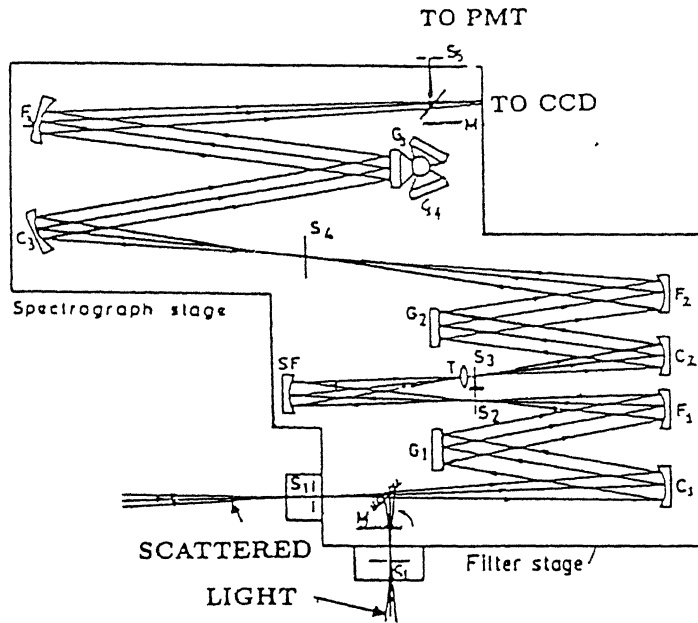
Figure 2.4: Schematic optical diagram of the Spex 1877E Triplemate.

coverage at the focal plane, the spectrograph has provision for mounting three gratings of different groove densities on a manually activated turret. The dispersed radiation is then detected by a liquid nitrogen cooled CCD or by a thermoelectrically cooled PMT The optical path of the triplemate is shown in Fig.2.4 and the specifications of the triplemate are given in Table 2.5.

2.6.3   Detection System

The detection system used for the present Raman measurements is a liquid nitrogen cooled Charge Coupled Device (CCD). The CCD is an ideal detector for multichannel detection of weak Raman signals [110]. It is an optical array detector, the operation of which is based on the accumulation of photogenerated charge carriers [111]. The collected charge is transported sequentially to a single charge sensor and then recorded. The peak efficiency of this device is centered in the red or near-infrared spectral regions [inset of Fig.2.5], making the CCD an ideal detector for Raman spectroscopy applications. Along the focal plane of

Table 2.5. Characteristics of Spex 1877 E Triplemate

Element	Specifications	
	Filter stage	Spectrograph stage
Mount (Czerny-Turner)	Two, subtractive mode	Asymetric
Focal length	0.22 m	0.60 m
Gratings	50×50 mm^2	64×64 mm^2
Grooves/mm	600	1200/1800
Dispersion at 514.5 nm		1.4 nm/mm
Spectra range	185-1000 nm	54,000-10,000 cm^{-1}
Accuracy	± 0.5 nm	± 0.5 nm
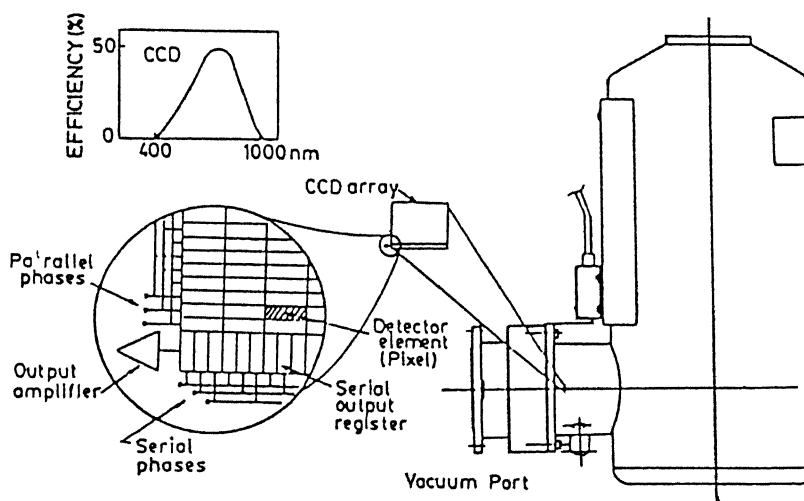
Figure 2.5: Cross section of Spectrum One CCD detector with 2 liter dewar. The inset shows the efficiency curve of CCD.

Table 2.6: Specification of Spectrum One CCD

Parameter	Value
Detector size	578 × 385 pixels
Pixel size	22 × 22 μm
Precision	16 bit
Peak quantum efficiency	50 % at 750 nm
Spectral response	400 to 1000 nm
Read out noise	4 to 10 electrons rms
Dark current	1 electron/pixel/hour
Operating temperature	-70 to -160° C (typically -140° C)
Approx. focal plane location	9.5 mm behind mounting flenge

the spectrometer, the CCD array (Spex Spectrum One) is mounted in a liquid nitrogen Dewar assembly [Fig.2.5] which cools the array for very low thermal noise level. The 2-liter capacity dewar is designed to keep the CCD sensor at a temperature ~140 K for 90 hours in a room temperature environment before refilling with liquid nitrogen. An interface unit [Fig.2.2] connects the dewar mounted CCD to the computer. The specifications of the Spectrum One CCD are given in Table 2.6.

CCD Evacuation

A loss of vacuum results in the insulation inability of the Dewar, it does not hold liquid nitrogen for specified time and the CCD array does not reach the required low temperature. To overcome this situation, the Dewar is evacuated periodically.

CCD Limitation

There are two serious limitations with the charge coupled device based detector systems. First, the CCD detectors are particularly sensitive to high energy photons and particles such as those in cosmic radiation. To minimize these events, the CCD may be covered

with foil/plates (preferrably aluminium) which can prevent cosmic rays from reaching the detector. The second problem is due to saturation of the device. This arises when one wishes to study weak Raman scatterers with very high background signal.

2.6.4 Low Temperature Stage for Raman Measurements

The low temperature Raman measurements on the manganite samples were carried out in 90° scattering geometry. We have used a helium closed cycle refrigeration unit [model CTI-CRYGENICS] [Fig.2.6] for this purpose. This system consists of a model 8200 com-
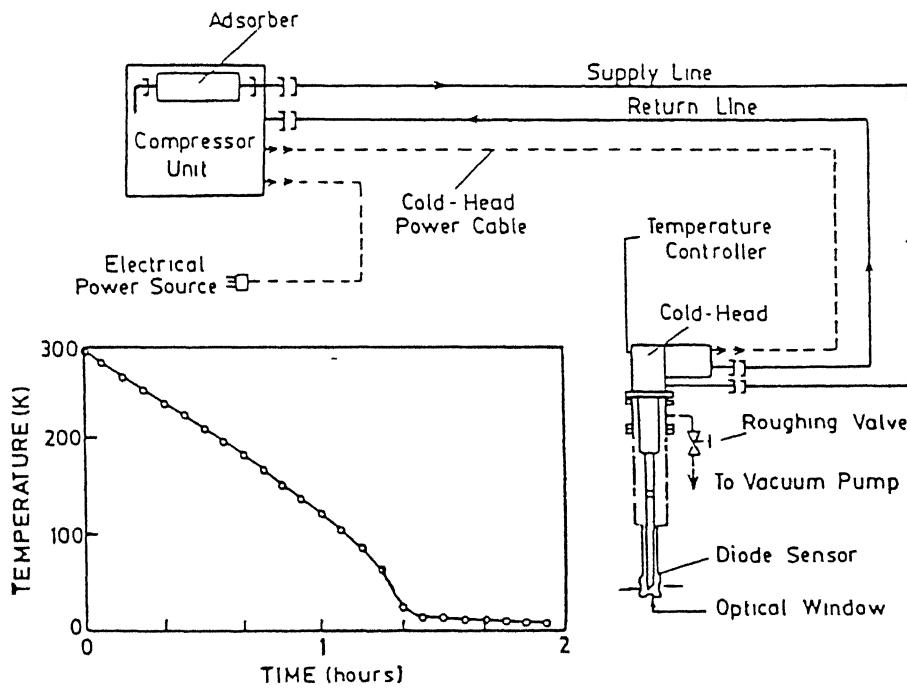
Figure 2.6: Schematic diagram of the low temperature set up used for the Raman measurements. The cooling rate of the cryotip is shown in the inset.

pressor, a model 22 cold head, Lake Shore model 805 temperature controller and associated interconnecting lines. High pressure helium from the compressor enters the cold head at the helium supply connector, and flows through the displacer-regenerator, DG assembly. Helium expansion in the DG assembly provides cooling at the first and second stage cold

stations. The resulting gas from the cold head enters the compressor. A small quantity of oil is injected into the gas stream to overcome its low specific heat. The gas is then compressed and passed through a heat exchanger for removal of compression caused heat. Then it flows through a bulk oil separator, oil-mist separator and helium filter cartridge. where oil and contaminants are removed. The cooling rate for cryotip is shown in the inset of Fig.2.6.

2.6.5 Data Acquisition Parameters

The various data acquisition parameters for the Raman measurements of the manganite samples are described in this section. The manganites are very weak scatterers so one has to scan for a longer time to get a good signal to noise ratio. In view of the cosmic ray spikes. the integration time is of special importance while using the CCD detector. Therefore. to get a good spectrum all these factors must be considered and optimized. The Raman spectra presented in this thesis have been taken mostly with 514.5 nm laser line and 800 cm^{-1} bandpass. The CCD integration time was typically 100 sec. The instrument was calibrated with crystalline silicon and diamond, since depending upon the alignment *i.e.* the angle at which the scattered radiation strikes at the entrance slit of monochromator in its focal plane, the peak position of the spectrum may shift within a few wavenumbers. The resolution of the spectrometer for Raman data of manganite samples was optimized by plotting the full width at half maximum (FWHM) of the sharpest band of $BaMnO_3$ system with the spectrograph slit width. These data are shown in Fig.2.7 indicate that the line width saturates for the slit width of $\sim 100 \mu m$. For all our measurements, 100 μm spectrograph slit width was used for high resolution of the spectra.
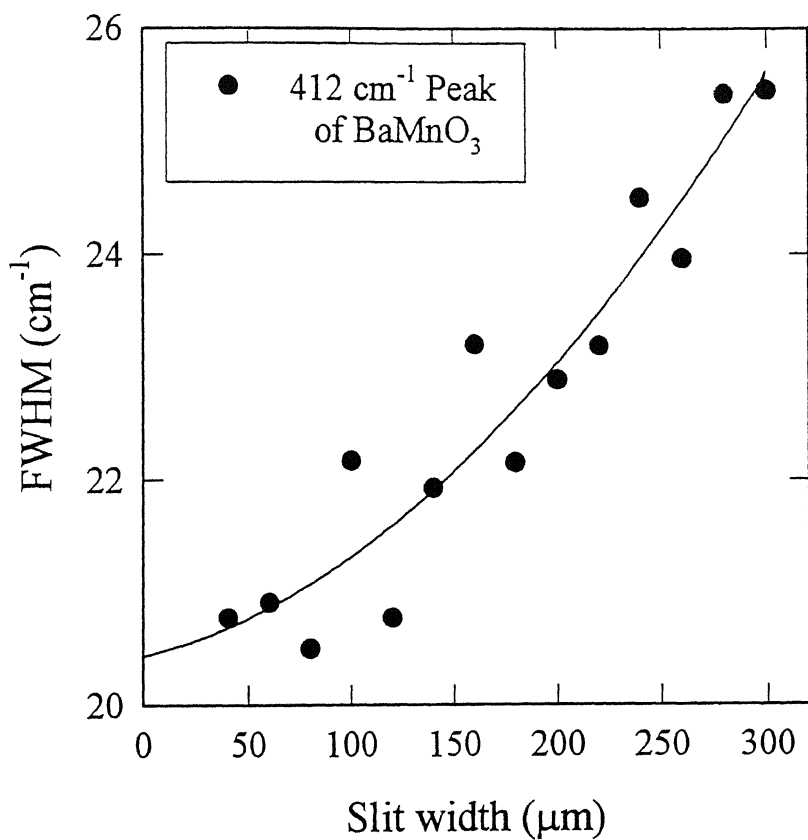
Figure 2.7: The full width at half maximum (FWHM) of the sharpest band of BaMnO₃ system plotted as a function of the spectrometer slit widths.

Chapter 3

Standard Characterizations of $La_{1-x}Ba_xMnO_3$ $(0 \leq x \leq 1)$

3.1 Introduction

The formation of different crystallographic phases in barium-doped lanthanum manganite system is relatively unexplored. In this Chapter we present our studies of the stability of $LaMnO_{3+\delta}$ $(\delta \geq 0)$ perovskite structure on substitution of Ba at lanthanum sites. Using X-ray powder diffraction, we establish the maximum Ba concentration for which the perovskite structure is stable.

3.2 Characterization Techniques

The samples synthesized through ceramic technique as described in Chapter 2 were characterized by two major techniques :

- X-ray powder diffraction (XRD) and

---

[0]The work presented in this Chapter is based on :
  1. "Raman-, infrared- and X-ray diffraction study of phase stability in $La_{1-x}Ba_xMnO_3$ doped manganites", Chaitali Roy and R. C. Budhani, *J. Appl. Phys.* **85**, 3124 (1999).

- Scanning electron microscopy (SEM)

The details of these experimental techniques are discussed in Chapter 2.

3.3 Results and Discussion

3.3.1 XRD Measurements :

The observed X-ray diffractographs of all the samples in the powder form, recorded in the range $20^o \leq 2\theta \leq 70^o$ are reproduced in Fig.(3.1, 3.2, 3.3).

(a) $LaMnO_{3+\delta}$, ($\delta \geq 0$) :

$LaMnO_3$ is the only compound in the $LaMO_3$-type (M = first row transition metal) compound series that exhibits either stoichiometric or nonstoichiometric form. The phases of this compound for $0 \leq \delta \leq 0.18$ are reported [21] to possess an orthorhombic lattice for $0 \leq \delta \leq 0.06$, a rhombohedral phase for $0.1 \leq \delta \leq 0.18$, and a two-phase mixture of orthorhombic and rhombohedral phases for $0.06 \leq \delta \leq 0.10$. We have used a controlled oxygen annealing technique with the objective to vary the structures of $LaMnO_3$ samples between the two limiting phases listed above. Figure 3.1 shows the $\theta - 2\theta$ scan for $LaMnO_{3+\delta}$ samples prepared in oxygen (curve a), argon (curve b) and samples first prepared in argon and subsequently annealed at 600°, 1000° and 1100^oC respectively (curves c, d and e) in oxygen environment. All the diffraction lines in Fig.3.1(b) can be indexed on the basis of an orthorhombic cell corresponding to $GdFeO_3$ type structure (space group Pbnm). The observation is consistent with the earlier reports of preparation of orthorhombic $LaMnO_{3-\delta}$. While we could not make a quantitative measurement of oxygen concentration in our samples, the observation of orthorhombic structure with lattice parameters a=5.53(Å), b=5.74(Å), and c=7.70(Å), suggest an upper bound of 0.04 for the δ The X-ray pattern of the sample prepared in pure oxygen (curve a) can be indexed in terms of a rhombohedrally distorted perovskite cell. A comparison of this result with the earlier reports [21, 36-37] also suggests a value of 0.10-0.14 for the δ. The 'd' spacings calculated from
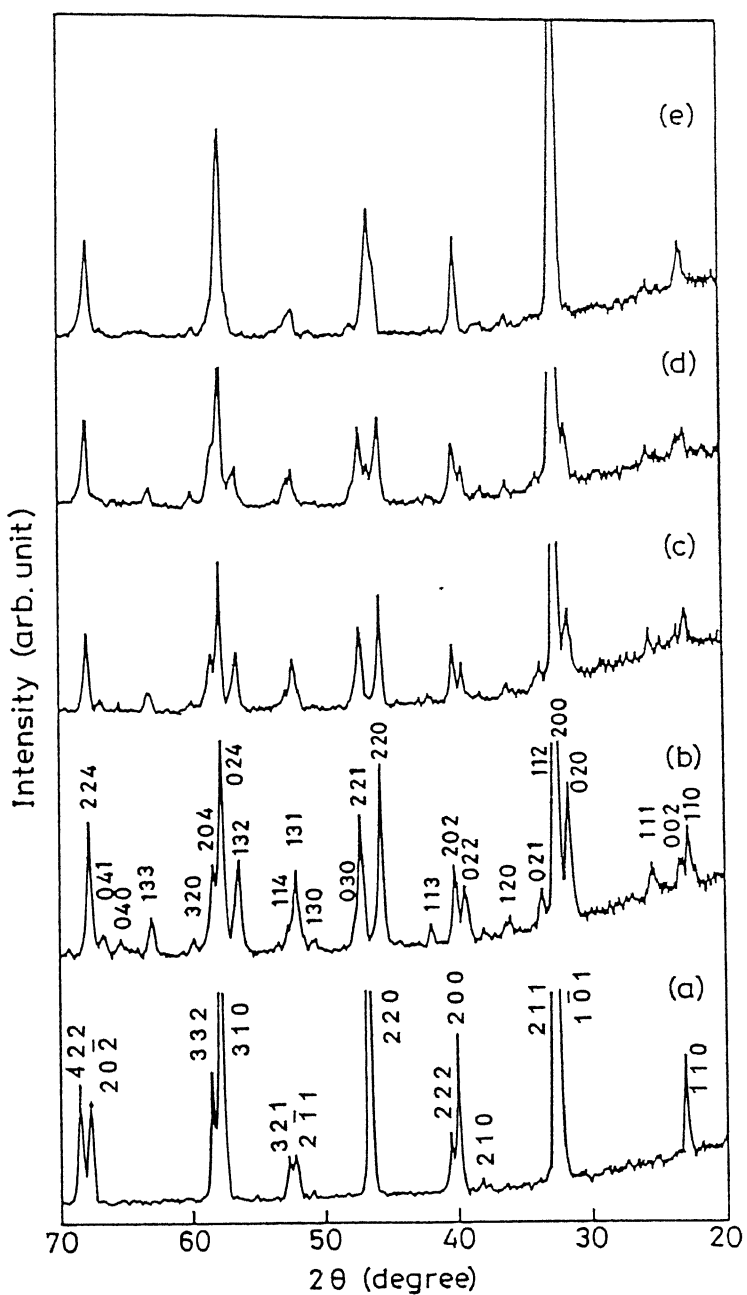
Figure 3.1: X-ray powder diffraction patterns of $LaMnO_{3+\delta}$ samples prepared under different annealing conditions; (a) Rhombohedral $LaMnO_{3+\delta}$ prepared in pure O_2, (b) orthorhombic $LaMnO_3$ prepared under argon, (c, d, and e) $LaMnO_{3+\delta}$ prepared on annealing ortho-$LaMnO_3$ in O_2 at 600, 1000, and 1100°C, respectively.

these patterns with λ=1.5405($\mathring{A}$) have been compared with the 'd' spacings as reported in the powder diffraction file (PDF) No.33-713 (for orthorhombic phase) and 32-484 (for rhombohedral phase). The comparisons of 'd' spacings with the PDF data are tabulated in Table 3.1 (for orthorhombic $LaMnO_{3+\delta}$) and Table 3.2 (for rhombohedral $LaMnO_{3-\delta}$). The close agreement between the $d_{observed}$ and d_{PDF} confirms the correctness of indexing the XRD patterns of $LaMnO_{3+\delta}$ compounds.

The samples originally synthesized in argon atmosphere were heat treated in oxygen for eight hours at several temperatures *viz.* 600, 1000 and 1100 ^{o} C, the X-ray diffraction are shown in Fig.3.1 (c, d, e). An interesting aspect of the annealing experiment is the possibility of making a two-phase mixture of orthorhombic and rhombohedral phases. This is very clear in the XRD patterns of some annealed samples [Fig.3.1(d)]. As evident from a comparison of pattern b and c in Fig.3.1, the oxidation of the material at 600°C leaves the orthorhombic structure intact. But for the samples oxidized at 1100°C, the orthorhombic distortion from the ideal perovskite phase disappears and the material tends to become cubic as evident from the diffraction pattern of Fig.3.1(e). The fact that rhombohedral angle α is closed to 60° in this case becomes clear from a comparison between (200) and (222) reflections in pattern e and a of Fig.3.1. X-ray diffraction measurement on samples oxidized at 600 and 1000°C reveal that this transformation from orthorhombic to cubic is gradual and proceed via the rhombohedral phase. The existence of two phase mixture is also established through the Raman measurement, which will be discussed in Chapter 4. The calculated lattice parameters and space groups for $LaMnO_{3+\delta}$ samples are listed in Table 3.3. It is interesting to note that all the orthorhombic samples obey the criterian $\frac{c}{a}<\sqrt{2}$, characteristics of a cooperative Jahn-Teller deformation superimposed on the orthorhombic structure resulting from t<1. Orthorhombic $LaMnO_3$ crystallizes in Pbnm (D_{2h}^{16}) symmetry group with Z=4 (Z is the number of formula units in the unit cell), rhombohedral $LaMnO_{3+\delta}$ belongs to space group R$\bar{3}$c (D_{3d}^6) with Z=2 whereas cubic $LaMnO_{3+\delta}$ crystallizes in P$_{m3m}$ (O_h^1) symmetry group with Z=1. The unit cell volume of $LaMnO_{3+\delta}$ samples decreases with increase of δ, which is evident from our XRD measurement. This

Table 3.1: Comparison of 'd' spacings with the PDF # 33-713 for orthorhombic $LaMnO_{3-\delta}$

$d_{observed}$	d_{PDF}	h k l
3.96	3.96	(1 1 0)
3.86	3.83	(0 0 2)
3.54	3.52	(1 1 1)
2.85	2.85	(0 2 0)
2.76	2.76	(1 1 2), (2 0 0)
2.68	2.68	(0 2 1)
2.36	2.36	(2 1 1)
2.29	2.29	(0 2 2)
2.25	2.24	(2 0 2)
2.16	2.15	(1 1 3)
1.98	1.985	(2 2 0)
1.92	1.921	(2 2 1), (0 0 4)
1.91	1.907	(0 3 0)
1.80	1.80	(1 3 0)
1.79	1.787	(2 1 3)
1.75	1.754	(1 3 1), (3 1 0)
1.73	1.73	(1 1 4)
1.71	1.709	(0 3 2)
1.63	1.631	(1 3 2)
1.59	1.595	(0 2 4), (3 1 2)
1.58	1.578	(2 0 4)
1.55	1.549	(3 2 0)
1.47	1.474	(1 3 3)
1.43	1.432	(0 4 0)
1.40	1.407	(0 4 1)
1.38	1.382	(2 2 4)
1.35	1.354	(0 2 5), (0 3 4)
1.32	1.324	(4 1 1)

Table 3.2: Comparison of 'd' spacings with the PDF # 32-484 for rhombohedral $LaMnO_{3-\epsilon}$

$d_{observed}$	d_{PDF}	h k l
3.89	3.86	(1 0 2)
2.76	2.75	(1 1 0)
2.73	2.72	(1 0 4)
2.35	2.34	(1 1 3)
2.25	2.24	(2 0 2)
2.23	2.22	(0 0 6)
1.94	1.937	(2 0 4)
1.79	1.787	(2 1 1)
1.75	1.741	(2 1 2)
1.73	1.727	(1 1 6)
1.59	1.591	(2 1 4)
1.57	1.570	(1 1 7)
1.38	1.379	(2 2 0)
1.37	1.365	(2 0 8)

Table 3.3: Calculated lattice parameters for $LaMnO_{3+\delta}$ compounds

Sample	Structure	Space group	a (Å)	b (Å)	c (Å)	α (°)
$LaMnO_3$ (Ar)	Orthorhombic	Pbnm, Z=4	5.53	5.74	7.70	
$LaMnO_{3+\delta}$ (O_2)	Rhombohedral	R$\bar{3}$c, Z=2	5.49			60.52
$LaMnO_{3+\delta}$ (600°C in O_2)	Orthorhombic	Pbnm, Z=4	5.54	5.71	7.71	
$LaMnO_{3+\delta}$ (1000°C in O_2)	Orthorhombic	Pbnm, Z=4	5.54	5.69	7.72	
$LaMnO_{3+\delta}$ (1100°C in O_2)	Cubic	P$_{m3m}$, Z=1	3.92			

is in good agreement with the earlier structural studies of $LaMnO_{3+\delta}$ by Roosemalen *et al.* [112]. These authors have studied the La_2O_3-Mn_2O_3 phase diagram in order to obtain the limits of perovskite phase. The largest influence on the structure is the overall amount of Mn^{4+} ions, but the La:Mn ratio and the temperature also play a significant influence on the structure. With increasing Mn^{4+} content in $LaMnO_{3+\delta}$ samples, the unit cell volume decreases and symmetry changes. With a low Mn^{4+} content ($\leq 20\%$) an orthorhombic symmetry with a large deviation from ideal perovskite structure has been found. This is due to the ordering of JT distorted $Mn^{3+}O_6$ octahedra. The ordering is destroyed by an increase in the Mn^{4+} content ($\geq 30\%$), which results in a rhombohedral or cubic symmetry. With an intermediate Mn^{4+} content, the behavior is complicated and depends on the La:Mn ratio rather than Mn^{4+} content. However, the structural behavior of this compound is not straight forward. Our structural measurements show the mixed-phase structure for some samples having the intermediate Mn^{4+} content *viz.* the samples oxidized at $600^\circ C$.

(b) $La_{1-x}Ba_xMnO_3$, ($0 < x \leq 1$) :

Figure 3.2 shows the changes in the powder diffraction pattern of the $1200^\circ C$ sintered $La_{1-x}Ba_xMnO_3$ samples as a function of Ba-concentration. The lattice parameters calculated from XRD patterns of the doped compounds are displayed in Fig.3.3. The crystallographic phase diagram of $La_{1-x}Ba_xMnO_3$ can be divided into four regions as shown in Fig.3.3. For $0<x<0.25$, the powder diffraction pattern can be indexed as due to a rhombohedral structure with $R\bar{3}c$ space group. With the increase of x from 0.05 to 0.25 the rhombohedral angle α decreases from 60.52° to 60.06° indicating a change to cubic phase. The space group for the cubic compound is P_{m3m}. The ideal perovskite structure of $La_{1-x}Ba_xMnO_3$ exists in the composition range of $0.25<x<0.40$. The X-ray diffraction pattern of the samples with x=0.40 reveals the presence of a second phase in the matrix of the cubic structure. The additional lines (marked by arrows) in the diffraction pattern are due to the presence of hexagonal $BaMnO_3$ [56] (space group P6$_3$mc) in the sample which phase separates for $x \geq 0.40$. A similar observation was also made on a sample of identical
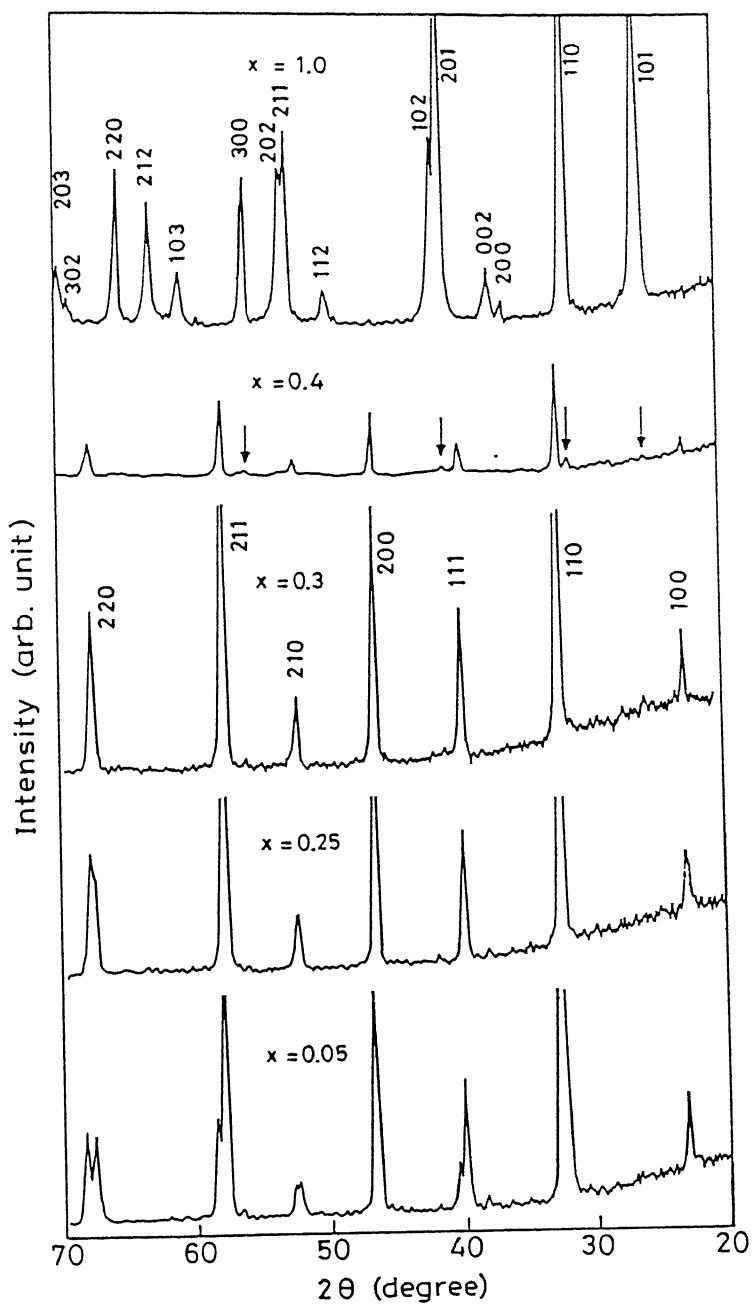
Figure 3.2: X-ray powder diffraction (θ-2θ) of the series $La_{1-x}Ba_xMnO_3$ for different values of x. The phase separation at x=0.4 is indicated by the appearance of diffraction peaks (marked by arrows) of the hexagonal $BaMnO_3$.
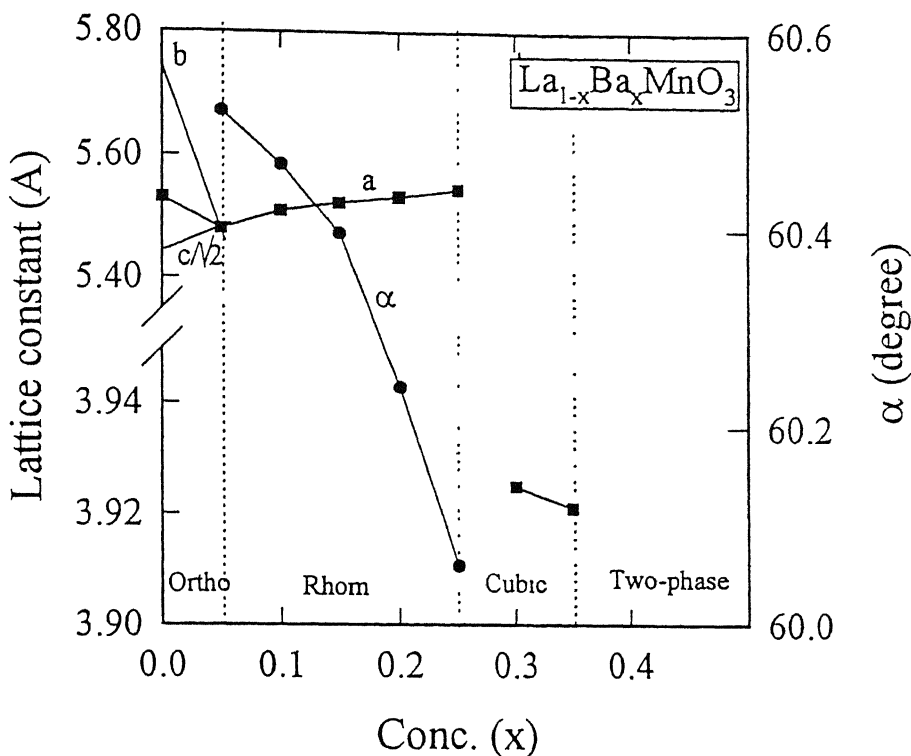
Figure 3.3: The lattice parameters as obtained from XRD patterns of the $La_{1-x}Ba_xMnO_3$ doped compounds.

Ba-composition synthesized at 1350°C. This result suggests that the phase separation is an intrinsic property of $La_{1-x}Ba_xMnO_3$ system.

The structural phase change from orthorhombic to cubic via rhombohedral symmetry with increasing x can be explained in terms of the Jahn-Teller distortion as it applies to pure material. The substitutional doping of Ba at the La site converts Mn^{3+} ions into Mn^{4-} state. The latter is not an Jahn-Teller ion and hence the JT distortion is gradually removed and the structure goes to a more symmetric form. The main factor responsible for the phase separation at large Ba concentration is the larger ionic radius of Ba^{2+} (1.43Å). As discussed in Chapter 1, the stability of the perovskite structure is mainly governed by the Goldschmidt [32] formula (Eq.1.1). The elements R, A, Mn, O form either simple $RMnO_3$ type or mixed $(R + R')(A + A')MnO_3$ type following the perovskite stability criteria. The perovskite structure for the manganite system is stable up to that concentration of alkaline earth (AE) metal for which it has cubic symmetry. Once a large number of La sites are

replaced by Ba, the cubic perovskite structure becomes unstable. The stability of the Ba-substituted lanthanum manganites has been studied by Chakraborty *el al.* [46] who also show that the material exists as a single phase cubic perovskite up to 40% substitution of Ba for La, and a further increase in Ba leads to the phase separation. However, our micro-Raman measurements show that the phase separation actually occurs for x$\geq$0.35 [113]. These results are discussed in detail in Chapter 4. The critical Ba-concentration (x$_c$, according to XRD studies is $\simeq$0.40 but from Raman measurements the value is established as $\simeq$0.35 after which BaMnO$_3$ phase separates out. On the other hand, the phase separation in Sr-substituted lanthanum manganite system is not established properly, but the studies on these materials in early fifties by Jonker [18] have shown that Sr and Ba as high as 70 and 50 percent respectively can be accomodated in the perovskite structure. While it is certain that the critical concentration x$_c$ for Sr-doped lanthanum manganite will be greater than the Ba-doped material due to the smaller ionic radius of Sr ion (1.27Å), the actual value x$_c$ for La$_{1-x}$Sr$_x$MnO$_3$ solid solution is yet to be established.

(c) BaMnO$_{3-\delta}$, ($\delta \geq 0$) :

The other extreme member of the series La$_{1-x}$Ba$_x$MnO$_3$ is the compound BaMnO$_{3-\delta}$. ($\delta \geq 0$). These are basically oxygen deficient compounds. As discussed in Chapter 1. the crystallographic structure of BaMnO$_{3-\delta}$ ($\delta \geq 0$) is quite complex. It exhibits several polymorphic forms depending on the value of oxygen and metal ion vacancies [50, 57-58]. The ideal anionic compositions for the various polymorphic forms have been established as BaMnO$_3$ (2H), BaMnO$_{2.90}$ (15R), BaMnO$_{2.875}$ (8H), BaMnO$_{2.83}$ (6H), BaMnO$_{2.8}$ (10H) and BaMnO$_{2.75}$ (4H) [114].

We have synthesized the stoichiometric BaMnO$_3$ compound in excess oxygen environment. In order to vary the oxygen stoichiometry, the oxygen rich BaMnO$_3$ compound was then quenched from various temperatures like 1400, 1320 and 1200°C to room temperature in air. Also, a separate set of samples of BaMnO$_{3-\delta}$ was synthesized in inert atmosphere like argon to yield a much more oxygen deficient compound. The XRD patterns of all

Table 3.4: Comparison of 'd' spacings with the PDF # 26-167 for 15-layer rhombohedral $BaMnO_{3-\delta}$

$d_{observed}$	d_{PDF}	h k l
3.29	3.289	(0 1 18)
2.84	2.839	(1 1 0)
2.36	2.358	(0 0 15)
2.15	2.149	(2 0 8)
2.02	2.018	(1 0 16)
1.81	1.814	(1 1 15)
1.73	1.745	(1 2 8)
1.64	1.644	(3 0 0)
1.42	1.420	(2 2 0)
1.34	1.345	(0 2 22)

such $BaMnO_{3-\delta}$ samples are shown in Fig.3.4(a-e). The XRD profile lebeled as 'a' is for the sample prepared entirely in argon environment. This pattern is very similar to the XRD pattern of the 15-layer rhombohedral (15R) $BaMnO_{3-\delta}$ compound. The diffraction pattern of Fig.3.4(a) can be indexed on the basis of a unit cell of rhombohedral symmetry. the observed d values ($d_{observed}$) and d_{PDF} values from powder diffraction file # 26-167 are compared in Table 3.4. The 15R compound belongs to the space group $R\bar{3}m$. A comparison of our X-ray data with the reports of Parras *et al.* suggests that the value of $\delta \sim 0.08$, so the ideal composition for this structural type is $BaMnO_{2.92}$. The calculated lattice parameters for this 15R $BaMnO_{3-\delta}$ are a=5.675Å and c=35.330Å. Figure 3.4(b) shows the $\theta - 2\theta$ X-ray diffraction pattern of oxygen rich $BaMnO_{3-\delta}$ compound synthesized in oxygen atmosphere. All diffraction maxima in pattern b can be indexed on the basis of a unit cell of hexagonal symmetry which is characteristic of the 2-layer (2H) structural type. The 'd' spacings calculated from this diffractograph have been compared with the 'd' spacings of the low temperature phase (2H) as reported in the powder diffraction file #26-168 (see Table 3.5). From the comparison of the lattice spacing and corresponding
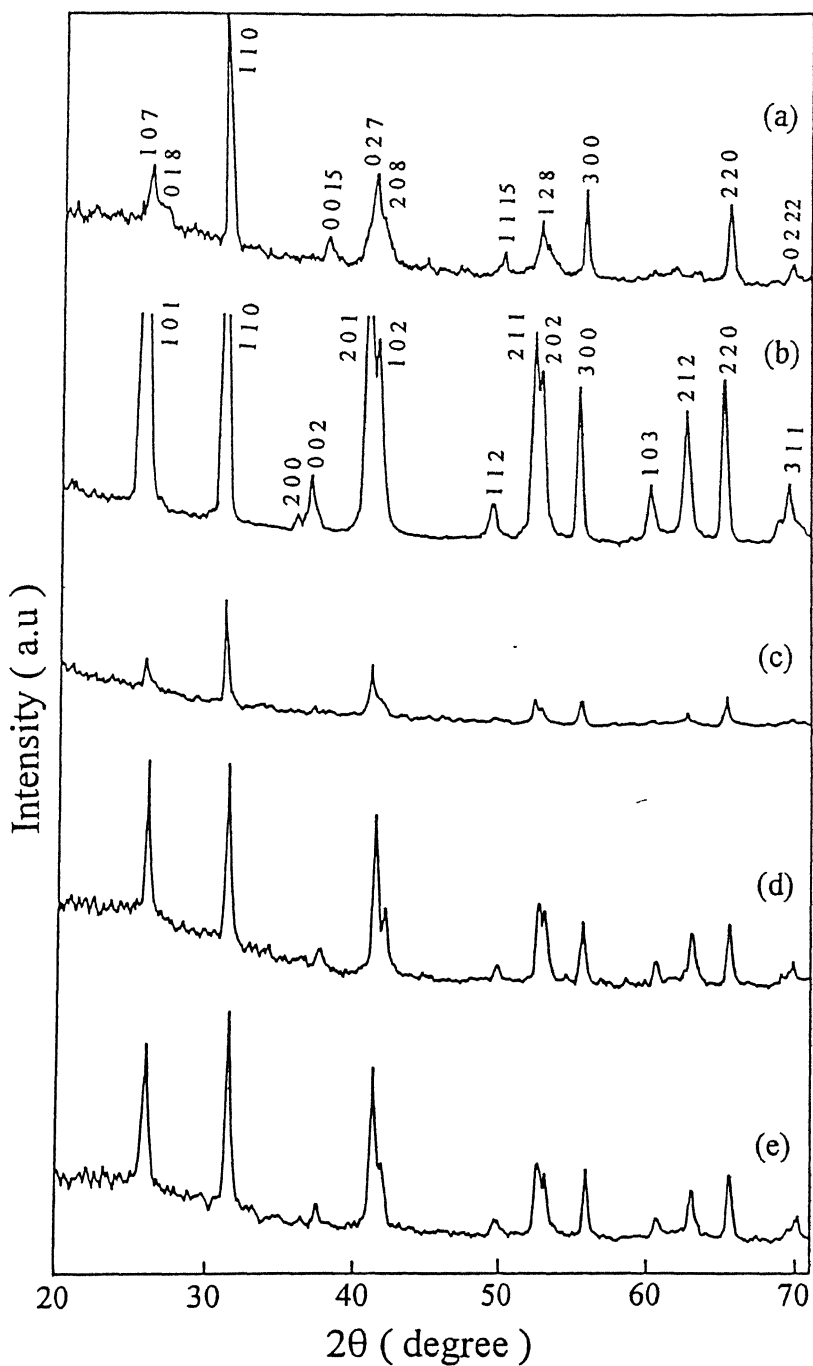
Figure 3.4: The XRD patterns of $BaMnO_{3-\delta}$ compounds prepared under various annealing conditions; (a) sample prepared in argon environment, (b) sample synthesized in oxygen rich environment, (c, d, and e) samples synthesized originally in oxygen rich environment were quenched from 1200, 1320, and 1400°C respectively to room temperature in air

Table 3.5: Comparison of 'd' spacings with the PDF # 26-168 for 2-layer hexagonal $BaMnO_3$

$d_{observed}$	d_{PDF}	h k l
3.44	3.452	(1 0 1)
2.84	2.851	(1 1 0)
2.47	2.468	(2 0 0)
2.41	2.408	(0 0 2)
2.19	2.197	(2 0 1)
2.17	2.165	(1 0 2)
1.84	1.841	(1 1 2)
1.74	1.740	(2 1 1)
1.72	1.720	(2 0 2)
1.64	1.646	(3 0 0)
1.52	1.527	(1 0 3)
1.47	1.475	(2 1 2)
1.42	1.425	(2 2 0)
1.36	1.359	(3 0 2)
1.34	1.346	(2 0 3)
1.32	1.318	(3 1 1)

intensity, it is observed that every diffraction peak in Fig.3.4(b) can be attributed to the reported structure. The lattice parameters are found to be a=5.698Å and c=4.4.827Å. The BaNiO$_3$ type crystallographic unit cell for hexagonal BaMnO$_3$ as proposed by Hardy [56] has lattice parameters a=5.672Å and c=4.71Å with the interatomic distances as Ba-O$_1$=2.84Å, Ba-O$_2$=2.86Å, Mn-O=2.02Å, and Mn-Mn=2.35Å. Note that the proposed structure gives two Ba-O bond lengths differing only by 0.02Å. Christensen and Ollivier [59], on the other hand, have refined their X-rays and neutron scattering data using the space group P6$_3$mmc. This structure gives only one Ba-O bond and lattice parameters are a=5.694Å and c=4.806Å. The interesting aspects of the structure in both the cases are the strings of Mn^{4+} ions parallel to the c-axis incased in face-sharing octahedra of oxygen ions [56, 59]. Figure 3.4(c-e) shows X-ray diffraction pattern of the samples quenched from 1200, 1320 and 1400°C respectively. On comparison of the patterns c, d and e with b it is observed that the reduction of oxygen concentration in the material is not high enough to result in a different polymorphic form other than 2L-hexagonal structure. In XRD patterns of all quenched samples no extra line is observed that can be attributed to some type of intergrowth of other phases in addition to the 2H phase. However, in Raman and IR measurements, the evolution of some bands gives the signature of 15R phase along with 2L hexagonal which will be discussed in Chapter 4. Accordingly the value of δ for these quenched samples can be estimated roughly in the range of $0 < \delta < 0.08$. The calculated lattice parameters for various BaMnO$_{3-\delta}$ samples are listed in Table 3.6.

The overall structural parameters of La$_{1-x}$Ba$_x$MnO$_3$, ($0 \leq x \leq 1$) are summarized in Table 3.7.

Table 3.6: Calculated lattice parameters for $BaMnO_{3-\delta}$ compounds

Sample	Structure	Space group	a (Å)	c (Å)
$BaMnO_3$ (Oxygen)	2L-Hexagonal	P6₃mmc	5.698	4.820
$BaMnO_{3-\delta}$ (Ar)	15L-Rhombohedral	R3̄m	5.675	35.330
$BaMnO_{3-\delta}$ (quenched from 1200°C)	2L-Hexagonal	P6₃mmc	5.696	4.819
$BaMnO_{3-\delta}$ (quenched from 1320°C)	2L-Hexagonal	P6₃mmc	5.711	4.817
$BaMnO_{3-\delta}$ (quenched from 1400°C)	2L-Hexagonal	P6₃mmc	5.689	4.814

Table 3.7: Summary of structural parameters for $La_{1-x}Ba_xMnO_3$ compounds

Conc. (x)	Structure	Space group	a (Å)	b (Å)	c (Å)	α (°)
0	Ortho.	Pbnm, Z=4	5.53	5.74	7.70	
0.05	Rhom.	R3̄c, Z=2	5.479			60.52
0.10	Rhom.	R3̄c, Z=2	5.509			60.46
0.15	Rhom.	R3̄c, Z=2	5.523			60.39
0.20	Rhom.	R3̄c, Z=2	5.533			60.24
0.25	Rhom.	R3̄c, Z=2	5.544			60.06
0.30	Cubic	P$_{m3m}$, Z=1	3.925			
0.35	Cubic	P$_{m3m}$, Z=1	3.921			
0.40-0.95	Mixed-phase					
1.00	2L-Hexagonal	P6₃mmc	5.698		4.820	

3.3.2 SEM Measurements :

The SEM micrographs of the fractured surfaces of the pellets of $LaMnO_3$ (Ar). $LaMnO_{3-\epsilon}$ ($600^\circ C$ in O_2), $LaMnO_{3+\delta}$ ($1000^\circ C$ in O_2) and $LaMnO_{3+\delta}$ (entirely in O_2) are shown in Fig.3 5a to Fig.3.5d respectively. In general, the oxygen rich samples synthesized fully in oxygen atmosphere are porous whereas the oxygen deficient samples show compact grains. The grain size is larger for oxygen deficient $LaMnO_3$ samples compared to the oxygen rich samples. Also, the grain size increases systematically as the samples synthesized originally in argon were annealed in oxygen environment at temperatures like 1000 and $1100^\circ C$. There are three distinct processes that occurs during the fabrication of ceramic materials: (i) primary recrystallization, (ii) grain growth and (iii) secondary recrystallization [115]. Primary recrystallization is the process by which nucleation and growth of a new generation of strainfree grains occurs in a matrix which has been plastically deformed. Grain growth is the process by which the average grain size of strainfree or nearly strainfree material increases continuously during heat treatment without change in the grain-size distribution. Secondary recrystallization, sometimes called abnormal or discontinuous grain growth, is the process by which a few large grains are nucleated and grow at the expense of a fine-grained, but essentially strainfree, matrix. From our SEM photographs, the second process as described is more appropriate as the grains are growing uniformly without disturbing the grain-size distribution.

The micrographs shown in Fig.3.5 reveal a grain size of $\sim$1-2 μm for oxygen deficient compound whereas it is $\leq$1 μm for oxygen rich $LaMnO_{3+\delta}$. The SEM micrographs of various Ba-doped lanthanum manganites are shown in Fig.3.6(a-c). The Ba-doped samples are also porous like oxygen rich parent compounds and the grain size is also nearly the same. The microstructure of a two-phase sample with x=0.8 is also shown in Fig.3.6(c). The SEM micrograph of the two-phase sample shows the grains of inhomogeneous distribution of two different phases *viz.* cubic LaBaMnO and hexagonal $BaMnO_3$ phases. Finally, Fig.3.7 shows the SEM micrograph of 2-layer hexagonal $BaMnO_3$ sample. The grain size $\sim$1.5 μm. The micrograph of $BaMnO_3$ sample shows grains of different symmetry like
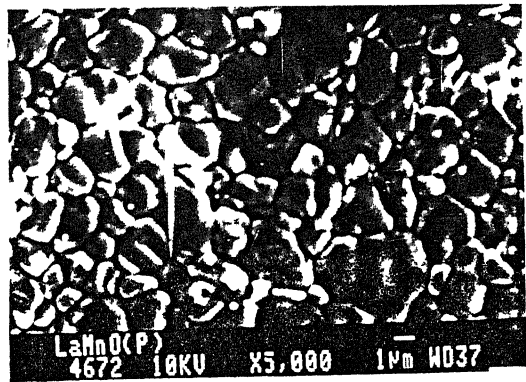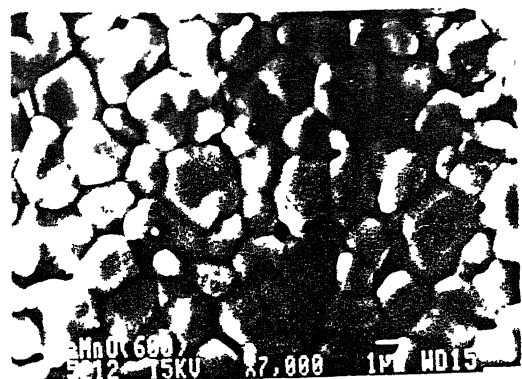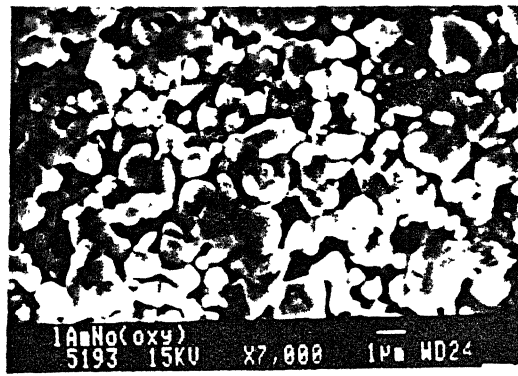
Figure 3.5: SEM photographs showing the surface morphology of (a) $LaMnO_3$ (argon), (b) $LaMnO_{3+\delta}$ (600^oC in O_2), (c) $LaMnO_{3+\delta}$ (1000^oC in O_2), and (d) $LaMnO_{3+\delta}$ (entirely in O_2).
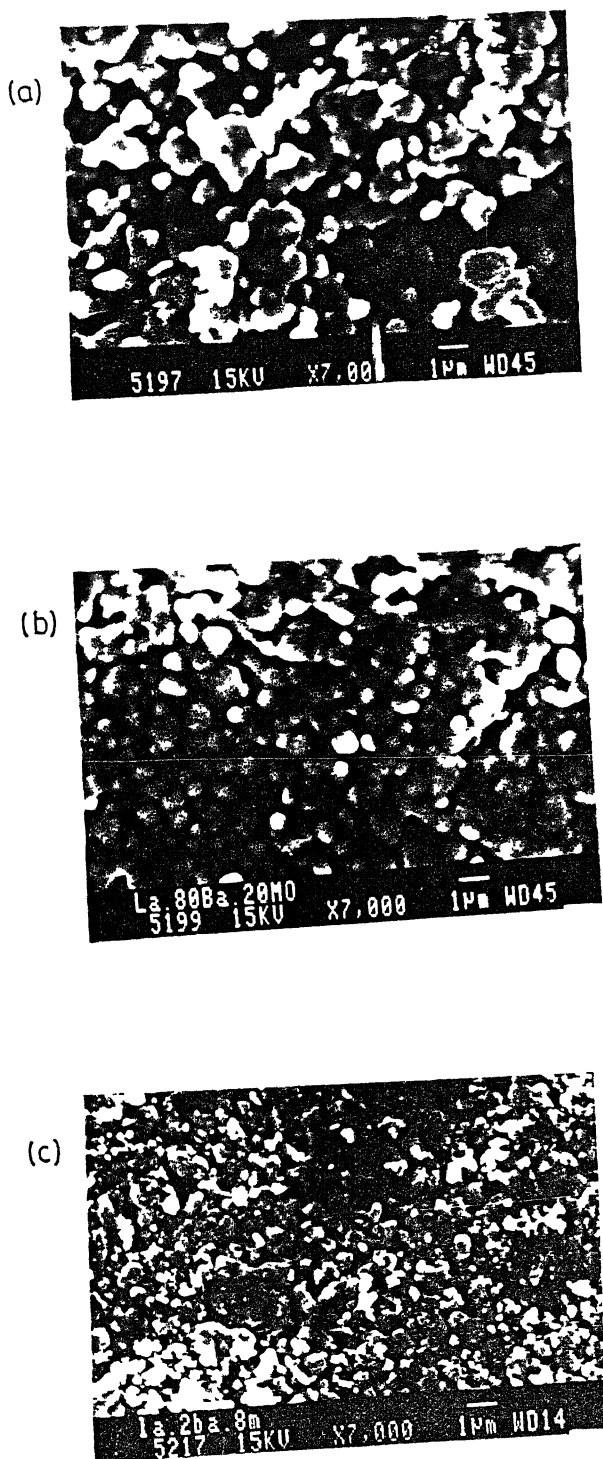
Figure 3.6: SEM micrographs of $La_{1-x}Ba_xMnO_3$ for (a) x=0.1, (b) x=0.2 and (c) x=0.8.

Figure 3.7: SEM micrograph of 2H $BaMnO_3$ sample prepared in pure oxygen environment.

elongated hexagonal structure compared to the structures observed in case of $LaMnO_{3-\varepsilon}$ or $La_{1-x}Ba_xMnO_3$ samples. None of the samples shows any impurity phase near the grain boundaries.

Chapter 4

Raman and IR Study of Phase Stability in La$_{1-x}$Ba$_x$MnO$_3$ (0≤x≤1) at Room Temperature

4.1 Introduction

The strong coupling of the vibrational and electronic degree of freedom in La$_{1-x}$A$_x$MnO$_3$ compounds has been established through X-ray absorption EXAFS [82], and isotope shift measurements of the Curie temperature. The coupling originates primarily from the static and dynamic Jahn-Teller distortion. Since the lattice distortion and changes in crystal symmetry would affect the phonon modes, a study of lattice vibrations can throw additional light on the electronic properties of these compounds. In this Chapter we present a systematic study of the Raman and infrared active phonon modes of various crystallographic phases in the system LaMnO$_{3+\delta}$, La$_{1-x}$Ba$_x$MnO$_3$, and BaMnO$_{3-\delta}$ at room temperature.

A comparison of the experimental data with a group theoretical analysis of the allowed zero-wave-vector phonon modes for the respective structures has been made to identify the presence of various phases and to establish phase boundaries. The use of micro-Raman technique has been made to detect small amounts of secondary phase which falls below the detection limit of X-ray diffraction.

4.2   Experimental Details

The polycrystalline samples of $LaMnO_{3+\delta}$, $La_{1-x}Ba_xMnO_3$ (0<x<1), and $BaMnO_{3-\delta}$ ($\delta \geq 0$) synthesized from solid state reaction method were used in the present study. For Raman measurements at room temperature, either 514.5 nm or 488 nm lines of an Ar^- laser was used to excite the sample in back scattering geometry. The scattered light was dispersed by Spex 1877E Triplemate and detected by a liquid nitrogen cooled CCD. The sample surfaces were seen on a TV monitor with the help of a video camera attached with Raman microprobe. The submicron spatial resolution of microprobe was used to select various spots on the surface of the sample. We callibrated the wavenumber scale by using c-Si and natural diamond spectra.

For infrared transmission measurements, we have used three commercial spectrophotometers as described in Chapter 2. The measurements of IR transmission spectra were carried out in the wave vector range from 300 to 4000 cm^{-1} at room temperature. The samples for these measurements were in the form of thin pellets made in KBr matrix.

4.3   Results and Discussion

The presence of various crystallographic phases in the system $La_{1-x}Ba_xMnO_3$ gives rise to characteristic variations in the spectral content of the Raman scattered light as a function of x. However, before we discuss the results of Raman scattering experiments, a group theoretical analysis of the allowed zone-center vibrations for various crystallographic structures is presented below.

4.3.1   Group Theoretical Formulation

A factor group analysis of the zone-center vibrational modes has been performed using the correlation table method. Results of the analysis for various crystallographic phases of lanthanum manganite system are presented in the subsequent discussions.

(a) $LaMnO_{3+\delta}$, $(\delta \geq 0)$:

We have seen that $LaMnO_{3+\delta}$ exists in various crystallographic forms. Depending upon the structural symmetry, the vibrational phonon modes vary. For stoichiometric compound the crystal symmetry is orthorhombic belonging to space group Pbnm with Z=4, corresponding spectroscopic group is D_{2h}^{16}. Site symmetries of D_{2h}^{16} are 2 $C_i(4)$, $C_s(4)$, and $C_1(8)$. The structure has two nonequivalent O sites C_s and C_1 respectively. The results of the factor group analysis for orthorhombic $LaMnO_{3+\delta}$ are given in Table 4.1. Out of 60 Γ-point phonon modes, $24(7A_g + 5B_{1g} + 7B_{2g} + 5B_{3g})$ are Raman active, $25(9B_{1u} + 7B_{2u} + 9B_{3u})$ are infrared active whereas $B_{1u} + B_{2u} + B_{3u}$ are acoustic and $8A_u$ are silent modes. The data presented here for this orthorhombic phase of $LaMnO_3$ are in good agreement with a recent work of Iliev *et al.* [88].

The rhombohedral phase of $LaMnO_{3+\delta}$ belongs to space group $R\bar{3}c$ with Z=2. The corresponding space group D_{3d}^6 has the site symmetries : $D_3(2)$, $C_{3i}(2)$, $C_3(4)$, $C_i(6)$, $C_2(6)$ and $C_1(12)$. In this case La, Mn and O atoms occupy the sites C_{3i}, D_3, and C_2 respectively. The factor group analysis for this phase yields $(A_{1g} + 4E_g)$ as Raman active modes, $(3A_{2u} + 5E_u)$ as IR active modes, $(A_{2u} + E_u)$ as acoustic mode and $(3A_{2g} + 2A_{1u})$ as silent modes (see Table 4.2).

The cubic symmetry of $LaMnO_{3+\delta}$ corresponds to space group Pm3m (O_h^1 spectroscopic group) with Z=1. The factor group analysis does not yield any first order Raman modes. The irreducible representations $3F_{1u}$ are IR active modes and F_{2u} is neither IR nor Raman active. The results of the analysis are presented in Table 4.3.

From factor group analysis of $LaMnO_{3+\delta}$ compound we observed that the number of Raman active modes increases from 5 to 24 on going from rhombohedral to orthorhombic

Table 4.1: Factor group analysis and selection rules for the zone-center vibrational modes of the orthorhombic $LaMnO_3$ (Pbmn), Z = 4.

Atom	Number of Equivalent Positions (Wyckoff Notation)	Site symmetry	Irreducible Representation of Modes
La	4(c)	C_s	$2A_g + B_{1g} + 2B_{2g} + B_{3g} + A_u$ $+ 2B_{1u} + B_{2u} + 2B_{3u}$
Mn	4(b)	C_i	$3A_u + 3B_{1u} + 3B_{2u} + 3B_{3u}$
O_1	4(c)	C_s	$2A_g + B_{1g} + 2B_{2g} + B_{3g} + A_u$ $+ 2B_{1u} + B_{2u} + 2B_{3u}$
O_2	8(d)	C_1	$3A_g + 3B_{1g} + 3B_{2g} + 3B_{3g} + 3A_u$ $+ 3B_{1u} + 3B_{2u} + 3B_{3u}$

$$\Gamma_{Raman} = 7A_g + 5B_{1g} + 7B_{2g} + 5B_{3g}$$
$$\Gamma_{IR} = 9B_{1u} + 7B_{2u} + 9B_{3u}$$
$$\Gamma_{acoustic} = B_{1u} + B_{2u} + B_{3u}$$
$$\Gamma_{silent} = 8A_u$$

Raman selection rules :

A_g : α_{xx}, α_{yy} and α_{zz}

B_{1g} : α_{xy}

B_{2g} : α_{xz}

B_{3g} : α_{yz}

structure. This increase may be due to the following three effects :

1. lowering of crystal symmetry which splits the doubly degenerate E_g modes into non-degenerate $B_{2g} + B_{3g}$,

2. displacement of oxygen atoms into the lower symmetry site of the La-plane which introduces six new Raman active vibrations, and

3. doubling of the unit cell which folds the zone-boundary modes of the rhombohedral structure into zone-center modes of the orthorhombic structure due to which nine new Raman active modes are created.

Table 4.2: Factor group analysis and selection rules for the zone-center vibrational modes of the rhombohedral $LaMnO_{3+\delta}$ ($R\bar{3}c$), Z = 2.

Atom	Number of Equivalent Positions (Wyckoff Notation)	Site symmetry	Irreducible Representation of Modes
La	2(b)	C_{3i}	$A_{1u} + A_{2u} + 2E_u$
Mn	2(a)	D_3	$A_{2g} + A_{2u} + E_g + E_u$
O	6(e)	C_2	$A_{1g} + 2A_{2g} + 3E_g + A_{1u}$ $+ 2A_{2u} + 3E_u$

$$\Gamma_{Raman} = A_{1g} + 4E_g$$
$$\Gamma_{IR} = 3A_{2u} + 5E_u$$
$$\Gamma_{acoustic} = A_{2u} + E_u$$
$$\Gamma_{silent} = 3A_{2g} + 2A_{1u}$$

Raman selection rules :

A_{1g} : $\alpha_{xx} + \alpha_{yy}$, α_{zz}

E_g : $(\alpha_{xx} - \alpha_{yy}, \alpha_{xy})$, $(\alpha_{xz}, \alpha_{yz})$

Table 4.3: Factor group analysis for the zone-center vibrational modes of the cubic $LaMnO_{3+\delta}$ (Pm3m), Z = 1.

Atom	Site symmetry (No. of equivalent atoms)	Irreducible Representation of Modes
La	O_h (1)	F_{1u}
Mn	O_h (1)	F_{1u}
O	D_{4h} (3)	$2F_{1u} + F_{2u}$

$$\Gamma_{IR} = 3F_{1u}$$
$$\Gamma_{acoustic} = F_{1u}$$
$$\Gamma_{silent} = F_{2u}$$

(b) La$_{1-x}$Ba$_x$MnO$_3$:

The crystallographic symmetry groups for the rhombohedral and cubic phases of Ba-doped lanthanum manganites are same as that of respective phases for the parent LaMnO$_{3-\delta}$ compound. Accordingly, the same factor group analysis (as described above) can be applied to rhombohedral and cubic phases of La$_{1-x}$Ba$_x$MnO$_3$.

(c) BaMnO$_{3-\delta}$, ($\delta \geq 0$) :

The XRD analysis of the stoichiometric BaMnO$_3$ reveals that the crystal symmetry of this compound is 2L-hexagonal belonging to the space group P6$_3$mmc (D$_{6h}^4$) with Z=2. However, Hardy [56] has suggested that the low temperature phase of BaMnO$_3$ corresponds to noncentrosymmetric space group P6$_3$mc (C$_{6v}^4$). In order to assign the correct space group to this compound a factor group analysis for both the space groups is necessary. We have performed a factor group analysis of the allowed phonon representations for both centrosymmetric P6$_3$mmc and noncentrosymmetric P6$_3$mc. Results of this analysis are presented in Table 4.4 and Table 4.5. The analysis for P6$_3$mmc (Table 4.4) shows that A$_{1g}$ + E$_{1g}$ + 3E$_{2g}$, 2A$_{2u}$ + 3E$_{1u}$, and A$_{2u}$ + E$_{1u}$ are the allowed Raman, infrared and acoustic phonon modes respectively whereas for noncentrosymmetric space group P6$_3$mc, the allowed Raman, IR and acoustic phonon modes are 3A$_1$ + 4E$_1$ + 5E$_2$, 3A$_1$ + 4E$_1$, and A$_1$ + E$_1$, respectively.

One of the oxygen deficient BaMnO$_{3-\delta}$ compounds having 15-layer rhombohedral phase corresponds to space group R$\bar{3}$m and the spectroscopic group D$_{3d}^5$. The compound has 15 molecular units per crystallographic unit cell. It should be noted that R type crystal structures may be divided by 3 or 1 to reduce the crystallographic unit cell to the Bravais space cell which results 5 molecular formula per unit cell. From the factor group analysis, we obtain the symmetry of the optical phonon modes at the zone-center as : out of a total 75 phonon normal modes (8A$_{1g}$ + 2A$_{2g}$ + 10E$_g$ + 3A$_{1u}$ + 12A$_{2u}$ + 15E$_u$), 28(8A$_{1g}$ + 10E$_g$), 39(11A$_{2u}$ + 14E$_u$) and (A$_{2u}$ + E$_u$) are the allowed Raman active, IR active and acoustic modes respectively, whereas A$_{2g}$ and A$_{1u}$ are inactive modes. The group theoretical data

Table 4.4: Factor group analysis and selection rules for the zone-center vibrational modes of the hexagonal 2L $BaMnO_3$ ($P6_3mmc$), Z = 2.

Atom	Number of Equivalent Positions (Wyckoff Notation)	Site symmetry	Irreducible Representation of Modes
Ba	2(d)	D_{3h}	$A_{2u} + B_{1g} + E_{2g} + E_{1u}$
Mn	2(a)	D_{3d}	$A_{2u} + B_{2u} + E_{1u} + E_{2u}$
O	6(h)	C_{2v}	$A_{1g} + A_{2g} + A_{2u} + B_{1u} + B_{2u} + B_{1g}$ $+ E_{1g} + 2E_{2g} + 2E_{1u} + E_{2u}$

Γ_{Raman} $= A_{1g} + E_{1g} + 3E_{2g}$

Γ_{IR} $= 2A_{2u} + 3E_{1u}$

$\Gamma_{acoustic}$ $= A_{2u} + E_{1u}$

Γ_{silent} $= A_{2g} + 2B_{1g} + B_{1u} + 2B_{2u} + 2E_{2u}$

Raman selection rules :

A_{1g} : $\alpha_{xx} + \alpha_{yy}, \alpha_{zz}$

E_{1g} : $(\alpha_{xz}, \alpha_{yz})$

E_{2g} : $(\alpha_{xx} - \alpha_{yy}, \alpha_{xy})$

Table 4.5: Factor group analysis and selection rules for the zone-center vibrational modes of the hexagonal 2L $BaMnO_3$ ($P6_3mc$), Z = 2.

Atom	Number of Equivalent Positions (Wyckoff Notation)	Site symmetry	Irreducible Representation of Modes
Ba	2(b)	C_{3v}	$A_1 + B_1 + E_1 + E_2$
Mn	2(a)	C_{3v}	$A_1 + B_1 + E_1 + E_2$
O	6(c)	C_s	$2A_1 + 2B_1 + 3E_1 + 3E_2$ $+ A_2 + B_2$

Γ_{Raman} $= 3A_1 + 4E_1 + 5E_2$

Γ_{IR} $= 3A_1 + 4E_1$

$\Gamma_{acoustic}$ $= A_1 + E_1$

Γ_{silent} $= A_2 + 4B_1 + B_2$

Raman selection rules :

A_1 : $\alpha_{xx} + \alpha_{yy}, \alpha_{zz}$

E_1 : $(\alpha_{xz}, \alpha_{yz})$

E_2 : $(\alpha_{xx} - \alpha_{yy}, \alpha_{xy})$

Table 4.6: Factor group analysis and selection rules for the zone-center vibrational modes of the 15R $BaMnO_{3-\delta}$ ($R\bar{3}m$), Z = 15.

Atom	Number of Equivalent Positions (Wyckoff Notation)	Site symmetry	Irreducible Representation of Modes
Ba_1	1(a)	D_{3d}	$A_{2u} + E_u$
Mn_1	1(b)	D_{3d}	$A_{2u} + E_u$
Ba_2, Ba_3, Mn_2, Mn_3	2(c)	C_{3v}	$A_{1g} + E_g + A_{2u} + E_u$
O_1	3(e)	C_{2h}	$A_{1u} + 2A_{2u} + 3E_u$
O_2, O_3	6(h)	C_s	$2A_{1g} + A_{2g} + 3E_g$ $+ A_{1u} + 2A_{2u} + 3E_u$

$$\Gamma_{Raman} = 8A_{1g} + 10E_g$$
$$\Gamma_{IR} = 11A_{2u} + 14E_u$$
$$\Gamma_{acoustic} = A_{2u} + E_u$$
$$\Gamma_{silent} = 2A_{2g} + 3A_{1u}$$

Raman selection rules :
$A_{1g} : \alpha_{xx} + \alpha_{yy}, \alpha_{zz}$
$E_g : (\alpha_{xx} - \alpha_{yy}, \alpha_{xy}), (\alpha_{xz}, \alpha_{yz})$

for this structure is presented in Table 4.6.

4.3.2 Raman Measurements

The results of the room temperature unpolarized Raman scattering from parent $LaMnO_{3-\delta}$ and Ba-substituted lanthanum manganites for entire range of doping *i.e.* the concentration range $0 \leq x \leq 1$ are presented below. The first order Raman spectra for these compounds are confined in the spectral range of 150-800 cm^{-1}. For pure $LaMnO_3$ system we have performed a laser annealing experiment using 514.5 nm line of a 5 Watt Ar^+ laser, the results of which are also described in the subsequent sections.

(a) $LaMnO_{3+\delta}$, ($\delta \geq 0$) :

The room temperature unpolarized Raman spectra of the orthorhombic and oxygen rich rhombohedral phases of $LaMnO_{3+\delta}$ prepared in argon and oxygen atmosphere respectively
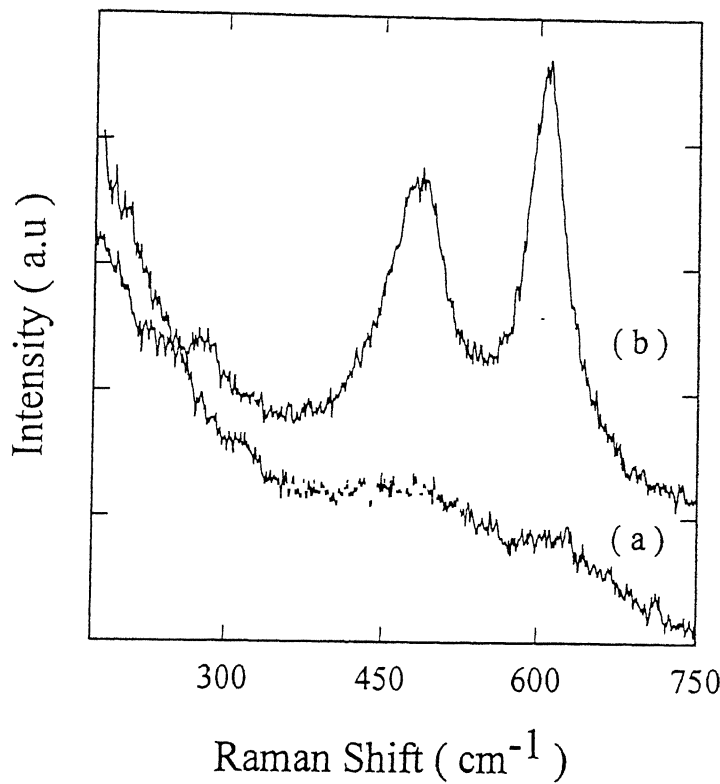
Figure 4.1: Raman spectra of the rhombohedral $LaMnO_{3+\delta}$ (curve a) and orthorhombic $LaMnO_3$ (curve b).

are shown in Fig.4.1. Two broad intensity distributions centered at 492 and 620 cm^{-1} have been observed in the Raman spectrum of the rhombohedral phase of $LaMnO_{3+\delta}$ (curve a). The factor group analysis for the allowed Raman modes of the rhombohedral structure yields one A_g and four E_g symmetry vibrations. On the other hand the Raman spectrum of the orthorhombic sample (curve b) is characterized by two prominent lines centered at 490 and 612 cm^{-1} and some weak spectral features at lower wavenumbers. This spectrum is identical to the one reported by Iliev *et al.* [88] for polycrystalline samples of orthorhombic $LaMnO_{3+\delta}$. We can assign the peak at 612 cm^{-1} to B_{2g} mode based on their polarization measurements and LDC calculations. The B_{2g} modes involve inphase stretched motion of O_1 atoms in the xz plane (see Fig.1.10). The broad peak centered at 490 cm^{-1} on the other hand, is due to phonon modes of A_g and B_{2g} symmetry. The corner shared MnO_6 octahedra are the building blocks of $LaMnO_3$ compounds as the Mn-O_1 and Mn-O_2 bonds
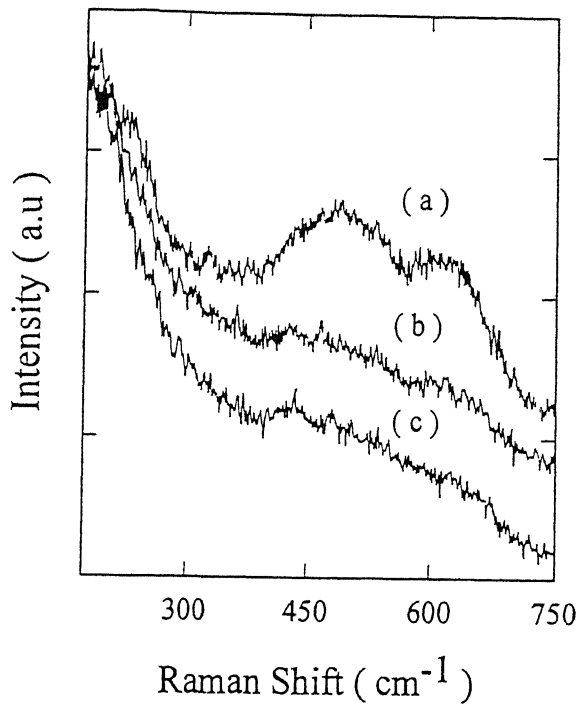
Figure 4.2: Raman spectra, a, b, and c of the samples prepared after annealing ortho-$LaMnO_3$ in O_2 at 600, 1000, and 1100°C, respectively.

are shorter than the La-O_1 and La-O_2 ones. The Mn atom is in the center of symmetry and does not participate in Raman active vibration. Therefore, one can expect that atleast part of the Raman modes will include motion of oxygen atoms similar to the characteristic ones for an isolated MnO_6 units.

Figure 4.2 shows the effects of oxidation on the Raman spectra of orthorhombic $LaMnO_{3+\delta}$. The prominent Raman peak at 612 cm^{-1} observed in the sample prepared in argon environment reduces considerably on annealing the sample at a temperature as low as 600°C (curve a). Further annealing of the samples at 1000 and 1100°C results in a Raman profile (curve b and c) identical to that of the rhombohedral phase (Fig.4.1). These observations are consistent with X-ray diffraction measurements as discribed in Chapter 3. As expected from the magnitude of the distortion, the scattering intensity decreases with the increase of Mn^{+4} content in the sample. The intensity change at $\delta > 0$ is explained by the smaller JT distortion of the nearly cubic $LaMnO_{3+\delta}$ structure because in perfect cubic

perovskites the first order Raman active modes are forbidden by the Raman selection rule as discussed in the previous section.

Figure 4.3 describes the results of laser annealing experiments carried out on the orthorhombic sample synthesized in argon environment. A series of spectra from the same spot of area $\sim 7 \ (\mu m)^2$ and the same exposure time of 100 sec at various power densities have been collected. In the absence of any laser induced structural changes, one would expect the intensity of the peaks to increase linearly with laser fluence. The inset of Fig.4.3 shows the dependence of 612 cm^{-1} peak height and full width at half maximum (FWHW) on the intensity. A sublinear dependence of the peak height and an increase in peak width on laser power are manifestation of a change in the structure. The modification of the spectra with the increasing incident energy can be attributed to oxidation of the sample and subsequent convertion to the rhombohedral phase. However, from our measurement it is observed that the structural change is not so prominent compared to the results of Iliev *et al.* [88]. This is due to the fact that the precise magnitude of such changes would depend on many extraneous factors such as porosity of the sample, rate of heat removal from the sample and humidity in the environment.

(b) $La_{1-x}Ba_xMnO_3$, (0<x≤1) :

The unpolarized Raman spectra of Ba-doped lanthanum manganite for the entire range of divalent doping are displayed in Fig.4.4. All the spectra were recorded at room temperature using $\lambda_{excitation}$ of 514.5 nm line of Ar$^+$ laser. The measurements for the samples (0.05≤x≤0.35) were done very precisely using the repeated scanning mode of the CCD detector so that a higher exposure time could be achieved. Since the scattering efficiency of these pseudocubic materials is very low, special care had to be taken in collecting the weak signal. It should be recalled that for x in the range of $\sim$0 - 0.2, X-ray diffraction measurements show a rhombohedral phase albeit with a decreasing distortion from the ideal cubic perovskite structure on increasing the x. The Raman spectra of these samples are identical to that of rhombohedral $LaMnO_{3+\delta}$ but for a gradual shift of the hump at 620 cm^{-1} to
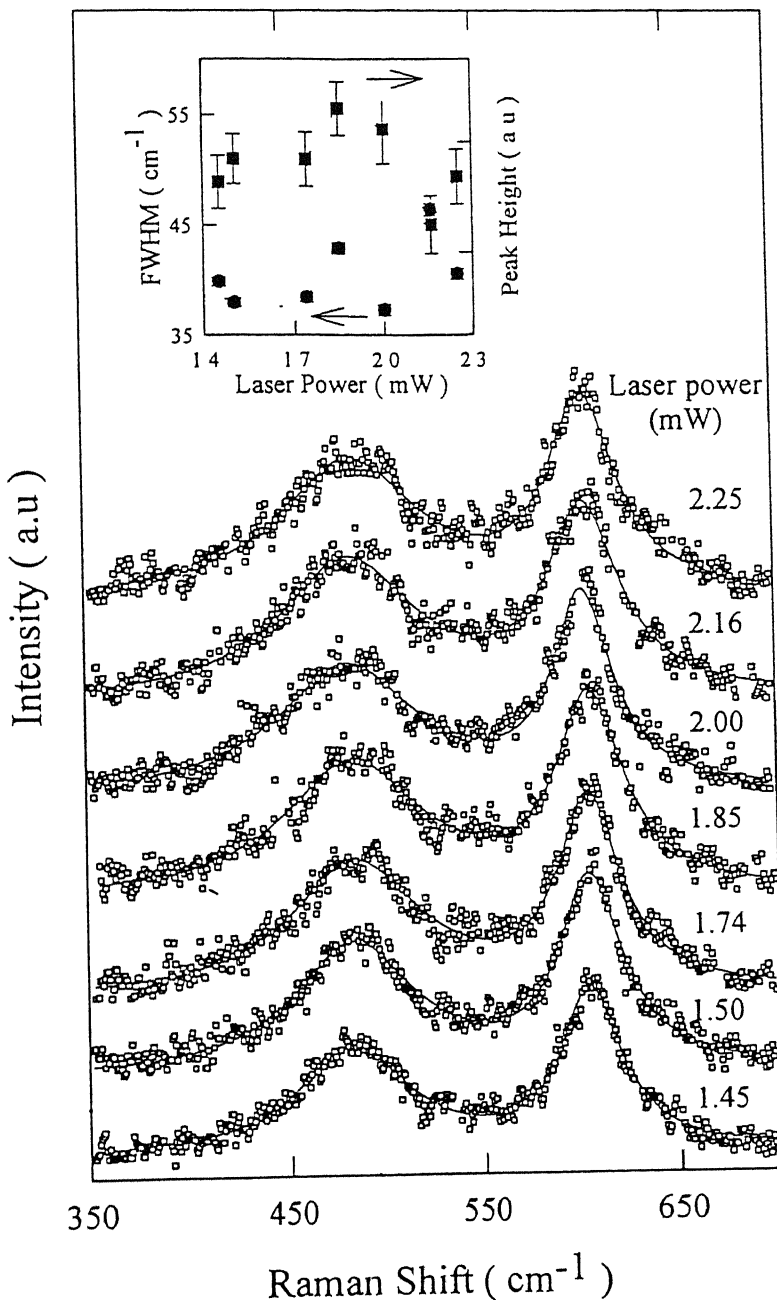
Figure 4.3: Raman spectra of the orthorhombic $LaMnO_3$ phase prepared in argon environment collected at different fluences of the laser beam from the same spot on the sample. Solid lines in the figure are Gaussian fits to the spectra used for extracting peak position and FWHM. Inset shows the power dependence of the peak intensity and FWHM of the Raman line at 612 cm^{-1}.
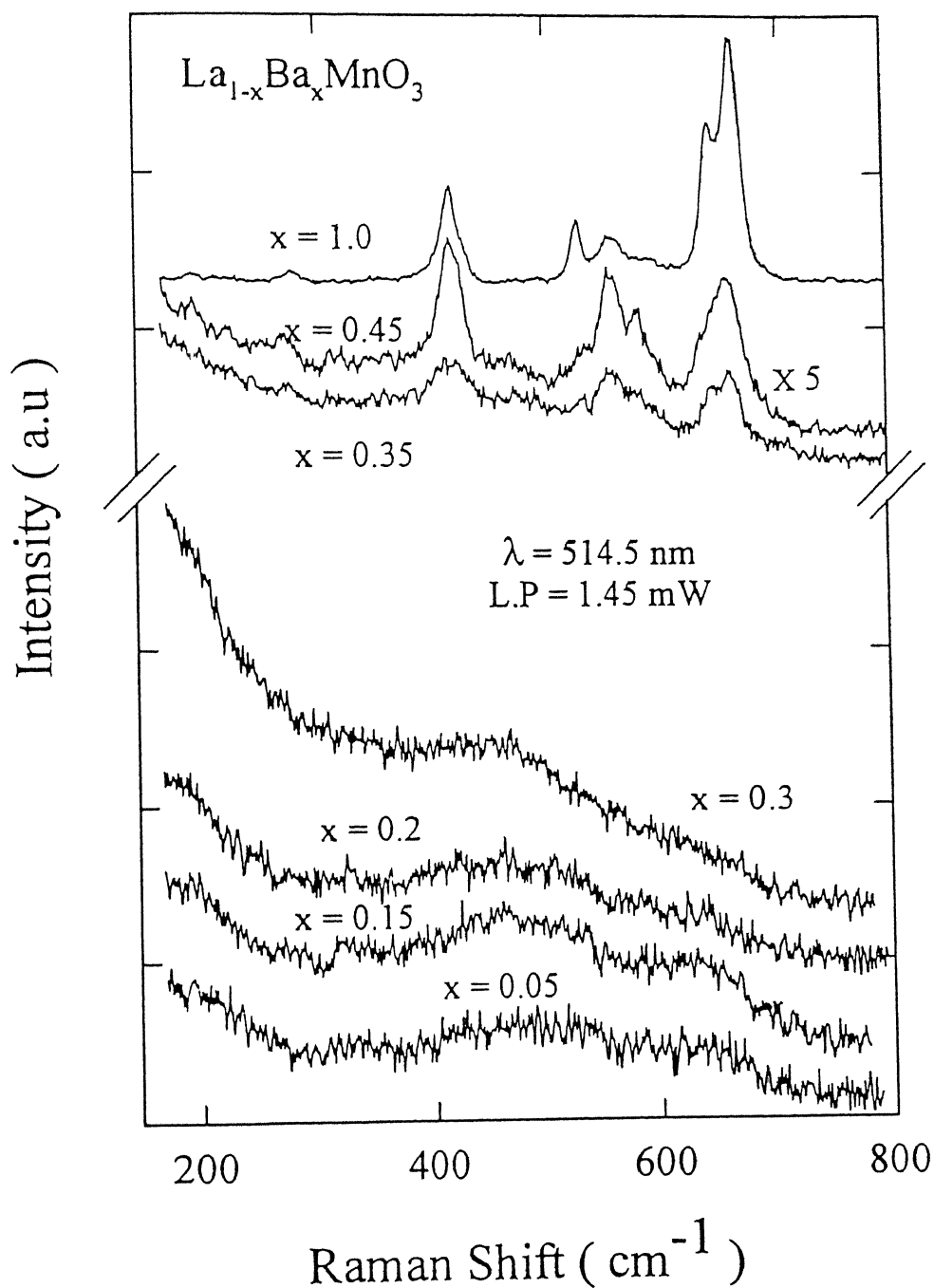
Figure 4.4: Room temperature Raman spectra of La$_{1-x}$Ba$_x$MnO$_3$ as a function of x. The figure also shows the spectrum of hexagonal BaMnO$_3$. The appearance of Raman lines at 415, 556, and 658 cm^{-1} in the spectrum for La$_{0.65}$Ba$_{0.35}$MnO$_3$ indicate a phase separation.
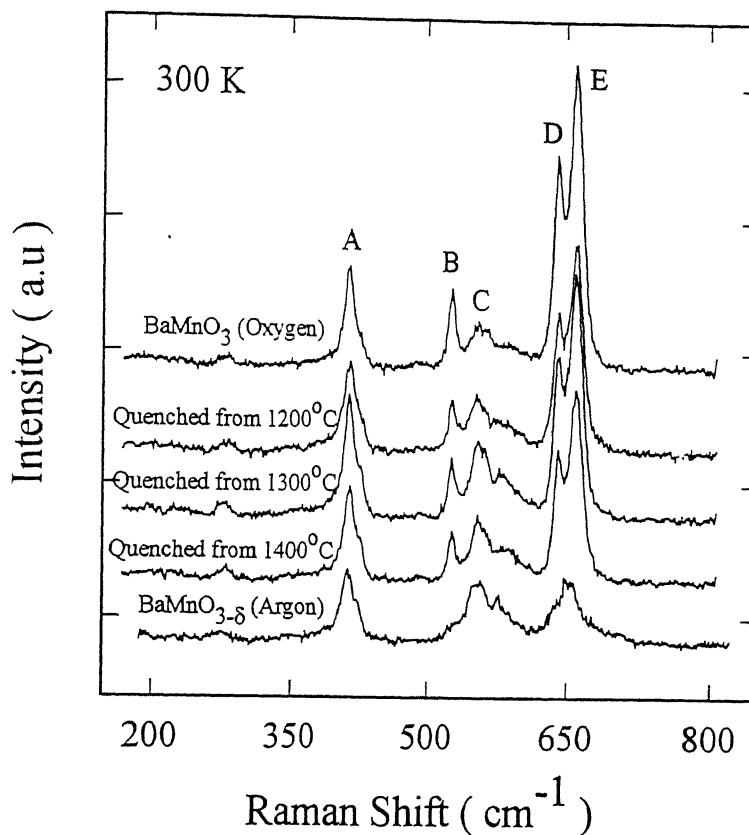
Figure 4.5: Room temperature Raman spectra of $BaMnO_{3-\delta}$ samples prepared under different annealing conditions.

$YMnO_3$ (space group $P6_3mc$, 6 formula units per unit cell) [117] indicates that the strongest lines appearing at 658 and 412 cm^{-1} in the spectrum may be due to the A_1 and E_1 symmetry vibrations respectively. Figure 4.5 also shows the Raman spectra of oxygen deficient $BaMnO_3$ prepared under various conditions, the sample synthesized entirely in argon environment shows striking change in its spectrum. The lines D and E are not well resolved in this case and peak intensities of these lines are also comparable to the intensity of peak A. But the major changes occured in the spectrum of this sample at lower temperatures, where we have seen some new prominent lines characteristic of a new phase. The detailed analysis of the low temperature measurements will be discussed separately. At this stage one can say that the room temperature spectrum of this oxygen deficient compound is from a different polymorphic form of $BaMnO_3$ other than the 2H. The XRD pattern of this sample is indexed to 15R structure belonging to space group

R$\bar{3}$m. The allowed Raman and IR active modes for this structure are more in number compared to the number of modes in 2H symmetry. The large number of Raman lines seen in this sample are consistent with these calculations. On the other hand, the Raman spectra of the BaMnO$_{3-\delta}$ as prepared through the quenching experiment are more or less similar to the spectrum obtained from the 2H compound. There is, however, a reduction in the peak intensity of lines B, D, and E on going from oxygen rich to the oxygen deficient compounds. This may be due to the fact that as this compound undergoes the reduction process, some of the Mn^{4+} ions would convert to Mn^{3+} resulting in an increase in the free carrier concentration. This free charge may screen the phonon modes. This effect is more clear in the IR absorption spectra of these compounds. The possibilities of intergrowth of any other phase in the case of quenched samples can not be ruled out however. There are several reports [57-58, 114] on these materials showing the intergrowth of 15R or 21R type structures along with 2H phase. However, the intergrowth phenomenon in the quenched samples will be clear when we discuss the IR spectra of these compounds.

4.3.3 IR Transmission Measurements

The changes in the crystallographic and electronic structure of $La_{1-x}Ba_xMnO_3$ with increasing Ba concentration are also reflected in the infrared transmission spectra of the samples. The IR spectra of the end members, namely LaMnO$_{3+\delta}$ and BaMnO$_{3-\delta}$ change considerabily on variation of δ. In the following, we discuss these results in detail.

LaMnO$_{3+\delta}$ and $La_{1-x}Ba_xMnO_3$:

The IR transmission spectra of LaMnO$_3$, LaMnO$_{3+\delta}$ and $La_{1-x}Ba_xMnO_3$ for some specific values of x in the spectra range of 2500-400 cm^{-1} are displayed in Fig.4.6. All the measurements were carried out at room temperature. These spectra are characterized by a set of discrete absorption bands in the frequency range of 400-700 cm^{-1} and a continuous absorption of increasing intensity as we go to higher energies. While the low frequency absorption bands are due to lattice vibrations of the perovskite structure, the continuous
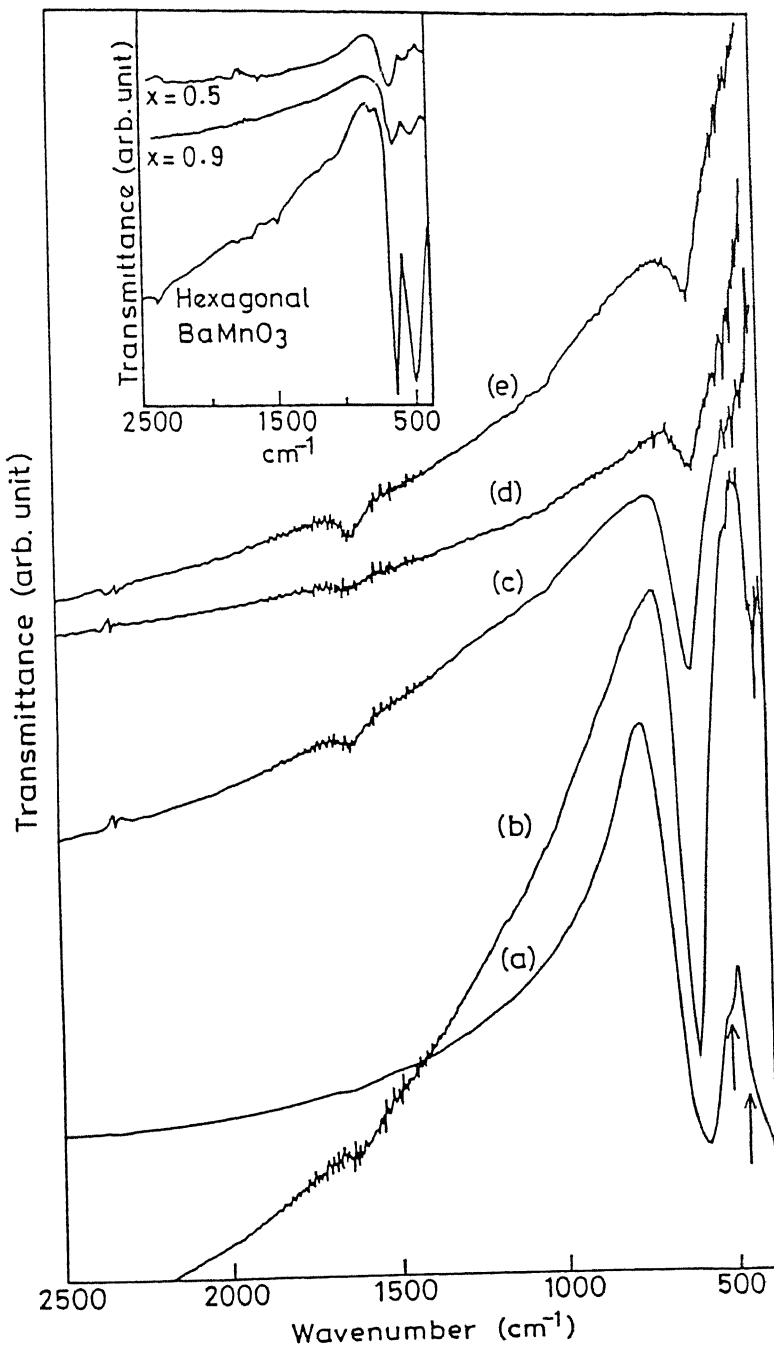
Figure 4.6: Infrared transmission spectra of $La_{1-x}Ba_xMnO_3$ for some representation values of x; (a) x=0, $\delta \approx 0$, (b) x=0, $\delta > 0$, (c) x=0.1, (d) x=0.2, and (e) x=0.25. Inset shows the IR transmission spectra of hexagonal (2L) $BaMnO_3$ and two mixed-phase samples with x=0.5 and x=0.9.

absorption whose onset (edge) shifts to lower wavenumbers with the increasing Ba concentration suggest a gap in the electron density of state of the material. The spectrum of orthorhombic $LaMnO_3$ (curve a) has two prominent vibrational bands centered at 405 and 603 cm^{-1}. These two spectral features are characteristic of many ABO_3 perovskite oxide [96] including doped manganites [84, 86]. In addition to these, some weak features (indicated by arrows) are also present in the spectrum. These observations are in agreement with reported IR measurements on $LaMnO_3$ [96]. From the frequency mass relationship for a rigid oscillator, one would expect these high frequency vibrations to be due to the internal modes of MnO_6 octahedra. Amongst all internal modes, the stretching motion of the Mn-O bond is expected to have the highest frequency followed by the distortional vibration of the O-Mn-O bond angle. Based on this arguement, we attribute the bands at 603 and 405 cm^{-1} to Mn-O and O-Mn-O vibrations, respectively. In the case of the rhombohedral phase of $LaMnO_{3+\delta}$, while the peak at ~603 cm^{-1} remains, the second feature of the orthorhombic $LaMnO_3$ centered at 405 cm^{-1} has a considerable reduced intensity. This peak is absent in $LaMnO_3$ doped with various amounts of Ba. It is also noticeable in the figure that the absorption edge due to the electronic excitations gradually shifts to lower wavenumbers as more La atoms are replaced by Ba atoms. This behavior, which is indicative of the disappearance of the gap, is closely linked with the insulator-to-metal transition in the system. The most interesting feature of the IR spectra presented in Fig.4.6 is the diminishing intensity of the Mn-O stretch mode with the increasing concentration of Ba in the structure. This behavior is also linked with the onset of a metallic state in the system. The inset of Fig.4.6 shows the infrared spectra of pure $BaMnO_3$ and samples with x=0.5 and 0.9. The IR spectrum of $BaMnO_3$ is characterized by strong phonon modes between 400-800 cm^{-1} and a large electronic absorption in the higher energy range. These characteristic phonon modes are also present in the spectra of samples with x=0.5 and 0.9 indicating a two-phase mixture as already seen in X-ray and Raman data.

BaMnO$_{3-\delta}$, ($\delta \geq 0$) :

Figure 4.7 shows the room temperature IR transmission spectra of the BaMnO$_{3-\delta}$ samples in the spectral range of 300-2000 cm^{-1}. The pronounced absorption bands for oxygen rich 2H-BaMnO$_3$ are centered at 405, 514, 550, 630 and 670 cm^{-1} and marked by letters A, B, C, D and E respectively. Note that these frequencies are same as the frequencies of A, B, C, D and E peaks in the Raman spectra at room temperature (Fig.4.5). The group theoretical analysis as discussed previously results in $\Gamma_{Raman} = 3A_1 + 4E_1 + 5E_2$ and $\Gamma_{IR} = 3A_1 + 4E_1$ for the case of noncentrosymmetric P6$_3$mc space group whereas for centrosymmetric group P6$_3$mmc the allowed Raman and IR modes are $\Gamma_{Raman} = A_{1g} - E_{1g} + 3E_{2g}$ and $\Gamma_{IR} = 2A_{2u} + 3E_{1u}$. The important point to notice here is that in the case of P6$_3$mmc, the A$_{1g}$ (nondegenerate) and E$_{1g}$ + 3E$_{2g}$ (doubly degenerate) Raman-active modes are distinctly different from the infrared-active modes. Whereas for P6$_3$mc, three nondegenerate A$_1$ modes and four doubly degenerate E$_1$ modes are common in IR and Raman. Since the Raman modes appearing at 412, 525, 555, 638 and 658 cm^{-1} are also seen in the IR spectrum, this observation suggests that the correct group assignment in the present case is P6$_3$mc.

The IR transmission spectrum of the BaMnO$_{3-\delta}$ samples prepared in argon environment shows the prominent absorption bands at 345, 405, 425, 510 and 620 cm^{-1}. The additional bands centered at 345 and 425 cm^{-1} are the manifestation of different polymorphic form. As we have seen from the factor group analysis that the 15R compound yeilds more number of IR active phonon modes compared to the 2H-BaMnO$_3$, this observation supports our assignment of the XRD pattern to a 15R structure. Note that the two additional bands centered at 345 and 425 cm^{-1} respectively are also observed in IR transmission spectra of CaMnO$_{3-\delta}$ system [86] which are correlated with Mn-O clusters. The intensity of these bands increases in the case of the quenched samples which indicates the presence of 15R phase in addition to the 2H phase in the compound. The Raman spectra of these quenched samples also showed some feature of 15R phase. Moreover, the IR measurements on these samples confirm the intergrowth of 15R phase in addition to
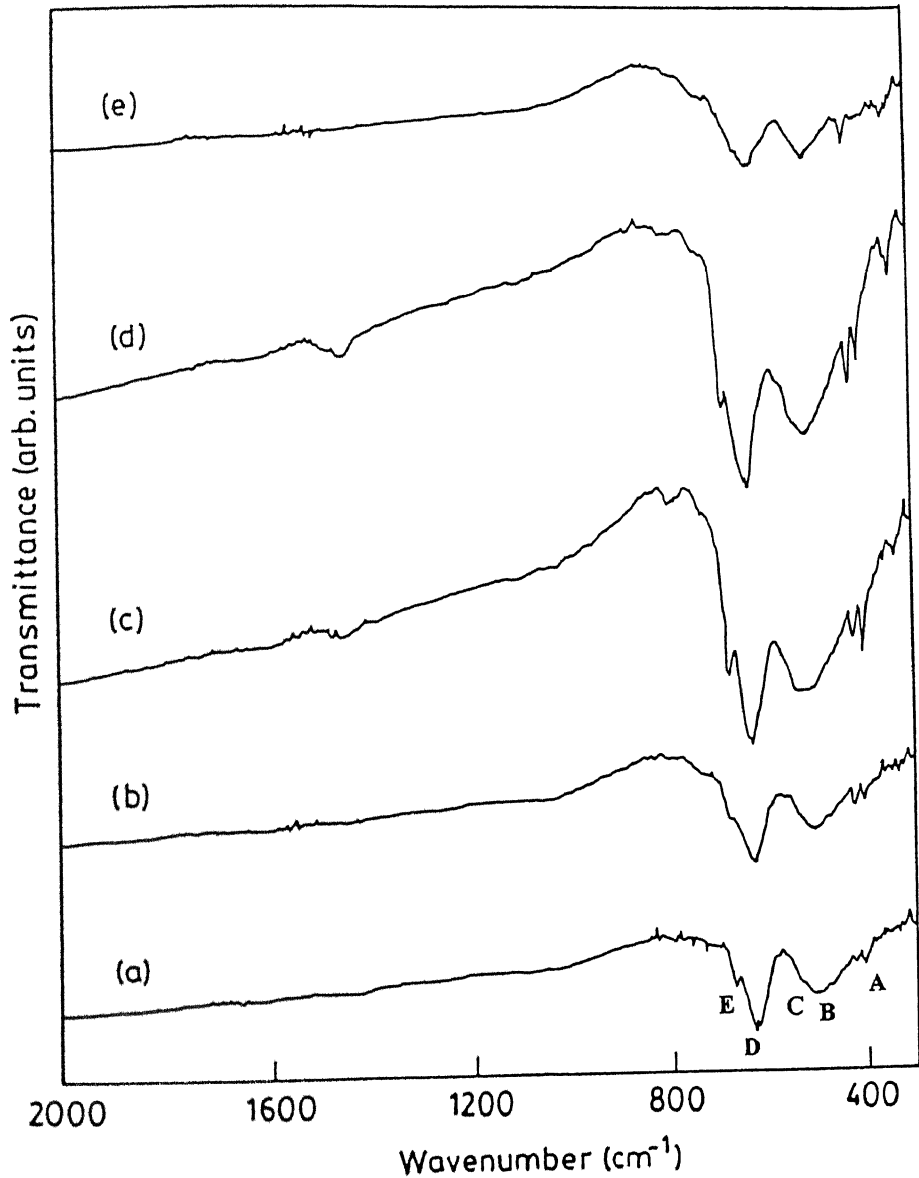
Figure 4.7: Infrared transmission spectra of $BaMnO_{3-\delta}$ samples prepared under different annealing conditions; (a) $BaMnO_3$ (O_2), (b, c, and d) $BaMnO_{3-\delta}$ (Quenched from 1200, 1320, and 1400°C respectively, and (e) $BaMnO_{3-\delta}$ (argon).

the 2H in these quenched samples. One of these bands $\sim$345 cm^{-1} also shows a large shift towards lower wavenumber 345$\rightarrow$335$\rightarrow$330 cm^{-1} on going from 15R to quenched at 1400^{o}C$\rightarrow$1320^{o}C$\rightarrow$1200°C respectively. Whereas for the 2H phase this band is absent. The peak intensity of the strongest band $\sim$630 cm^{-1} is reduced sharply compared to the intensity of the band at 500 cm^{-1} on going from oxygen rich to oxygen deficient compound. this may be explained in terms of the free carriers which suppress the phonon modes present in the oxygen deficient samples. We have also noticed a similar trend in Raman spectra of these compounds

Chapter 5

Magnetic Behavior of La$_{1-x}$Ba$_x$MnO$_3$, $(0{\leq}x{\leq}1)$ compounds

5.1 Introduction

The generic behavior of paramagnetic-to-ferromagnetic transition in $R_{1-x}A_x MnO_3$ manganites is understood within the framework of double-exchange theory [62, 71-72], which includes only the transfer integral of the e_g electrons and the on-site exchange interaction (Hund's coupling J_H) between the itinerate e_g electrons and localized t_{2g} spins (S=3/2). The doped manganites show much more multifarious magnetic properties depending on the relative ionic radii of the rare-earth and the alkaline-earth dopant In a system like $Pr_{0.5}Sr_{0.5}MnO_3$ for example, the ferromagnetic state which develops at 270 K is destroyed by the real space ordering of Mn^{3+} and Mn^{4+} ions into two sublattices at 140 K. At this temperature the system also becomes antiferromagnetic. In a system like $Pr_{0.5}Ca_{0.5}MnO_3$, the charge ordered (CO) state is much more robust. The CO and AFM

---

transitions are decoupled in this case [118]. Recently Akimoto *et al.* [119] have systematically investigated the ground state properties for the manganites as a function of nominal hole concentration (x) and the arranged ionic radius (r$_R$) of the rare-earth ion. It has been observed that the magnetic phase diagram of these materials is dominated by the ferromagnetic metallic (FM) state in the low-x region and an antiferromagnetic metallic (AFM) state with A-type spin structure in the high-x region. The magnetic behavior of the Ba doped LaMnO$_3$ can be quite different due to the large radius of Ba^{2-}. As we have already seen this system exhibits in a single phase material only upto 35% doping of Ba in the La sites. In order to understand the magnetic behavior of Ba-doped lanthanum manganites we have carried out a systematic measurements of the magnetic moment on the bulk samples of La$_{1-x}$Ba$_x$MnO$_3$. In this Chapter we present the results of these measurements over a wide range of composition (0≥x≥1), temperature (4.2K-775K) and magnetic field strength (1G-50kG). We have probed the magnetic state of the two-phase region, and have established the effects of magnetic inhomogeneity on T$_c$. It is important to point out here that while such granular effects have been well studied in metallic systems from the viewpoint of magnetoresistance and superparamagnetism, the granularity in manganites is of considerable current interest from the viewpoint of spin-polarized transport. The work has also been undertaken to reinvestigate the magnetic state of the two end members of the La$_{1-x}$Ba$_x$MnO$_3$ series.

5.2   Experimental Details

The polycrystalline samples of LaMnO$_{3+\delta}$, La$_{1-x}$Ba$_x$MnO$_3$ for x in the range of 0<x<1, and BaMnO$_{3-\delta}$ as synthesized from solid state reaction method were used in the present study. Magnetization measurements as a function of temperature (4.2K-775K) and applied field (1G-50kG) were performed using three commercial magnetometers (Quantum Design SQUID magnetometer MPMS-system, Quantum Design extraction magnetometer PPMS system and a vibrating sample magnetometer). The paramagnetic susceptibility of some of the compounds was also measured in the temperature range 400K to 750K using the

high temperature stage of the SQUID magnetometer.

5.3   Results and Discussion

In the following sections we present magnetic ordering aspects of LaMnO$_{3+\delta}$, BaMnO$_{3-c}$ and La$_{1-x}$Ba$_x$MnO$_3$ (0<x<1) samples synthesized under various conditions. The paramagnetic susceptibility of these materials is also discussed. Finally, the possible existence of superparamagnetism in the two phase region is analysed.

5.3.1   Magnetic Behavior of LaMnO$_{3+\delta}$:

The temperature dependence of magnetization for the LaMnO$_{3+\delta}$ samples prepared in argon and oxygen environments is depicted in Fig.5.1. The oxygen rich sample shows a well-developed ferromagnetic state at T$\leq$200 K which is characterized by a large moment
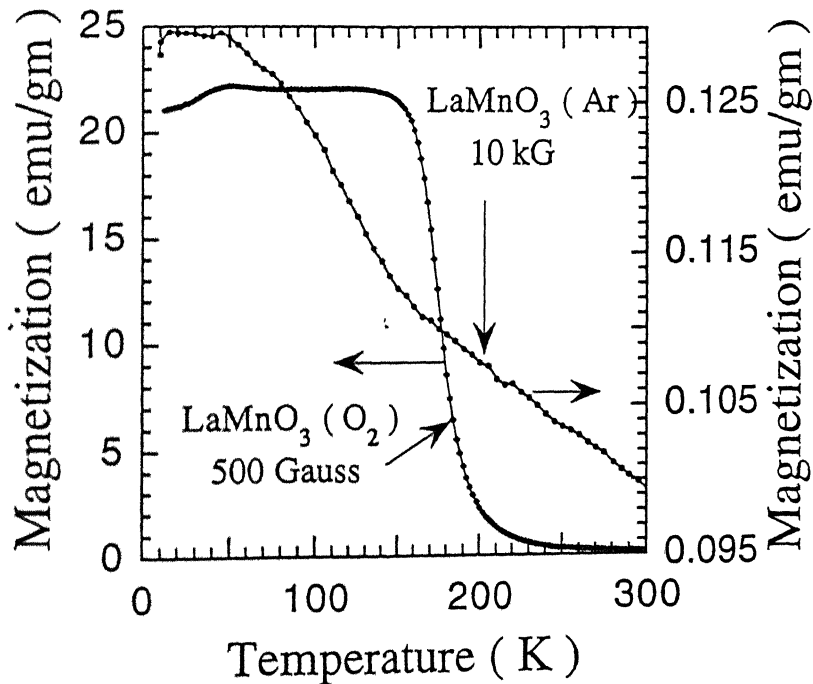
Figure 5.1: Zero-field-cooled magnetization curves of LaMnO$_3$ samples prepared in argon and oxygen environments. Measurements have been done at different fields as indicated in the figure.

in a field as low as 500 G, whereas the oxygen deficient sample (prepared in argon) has a
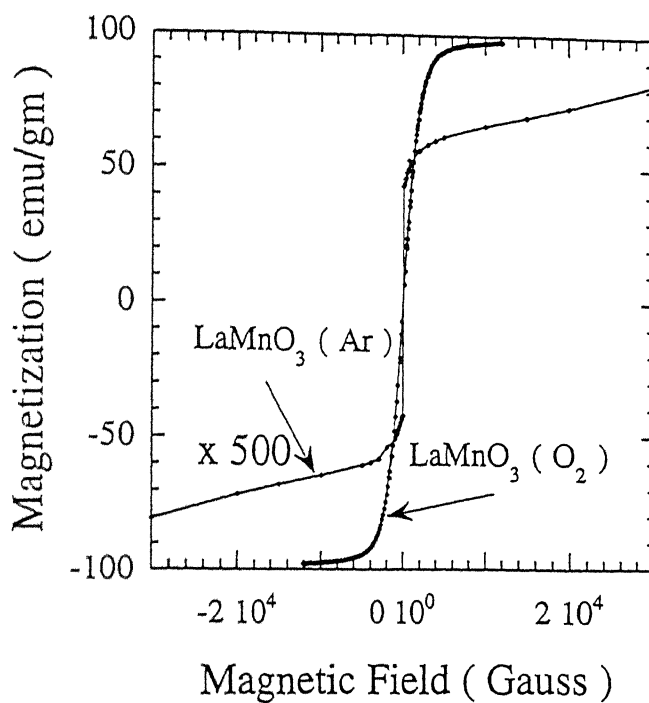
Figure 5.2: Dependence of magnetization of the two types of $LaMnO_{3\pm\delta}$ samples on the applied magnetic field.

much smaller moment at 5 K even at 10 kG magnetic field. On increasing the temperature, the magnetic moment of the oxygen deficient sample first remains unchanged upto T$\simeq$50 K and then drops with a well-defined inflection point at T$\sim$145 K. As stated in Chapter 3, the sample synthesized in argon atmosphere showed a single phase orthorhombic structure. We attribute the change in magnetization at 145 K to the onset of antiferromagnetic state in this orthorhombic phase where Mn ions are in +3 valence state. This conclusion is consistent with neutron diffraction measurements on orthorhombic $LaMnO_3$ [60-61, 119]. The behavior of magnetization at 10K as a function of field for the two samples is shown in Fig. 5.2. A strong ferromagnetic behavior of the oxygen rich sample is evident in the figure. The magnetization saturates at $\sim$12kG field with a saturation value of $\sim$97 emu/gm which corresponds to an effective moment per Mn ion of $\sim$4.2 μ_B. On the other hand, the field dependence of magnetization for the orthorhombic sample is remarkably different. The M vs H curve in this case is characterized by a sharp increase of M for $|H| \leq 3$ kG followed by a much slower dependence of M on H. The value of magnetization at H $\approx$ 5 kG

corresponds to a $\mu_B \sim 0.006$. This small value of the moment per Mn ion is consistent with the picture of a Dzialoshinsky type canting of antiferromagnetically ordered Mn^{3+} spins [81]. The crystallographic phase of the oxygen rich $LaMnO_{3+\delta}$ sample is rhombohedral as determined from our x-ray diffraction study A comparison of these magnetization and XRD results on $LaMnO_{3-\delta}$ with the works of Topfer and Goodenough [21] suggests a δ of ~ 0.0 and 0.1 for the oxygen deficient and oxygen rich samples respectively. Hauback et al. [36] have also reported effects of non-stoichiometry on the magnetic properties of $LaMnO_{3+\delta}$. The behavior of our oxygen rich sample is in excellent agreement with the magnetization measurements of these authors on a rhombohedral sample of nominal composition $La_{0.96}MnO_{3+\delta}$.

The low value of saturation magnetization ($\mu_B = 0.006$) due to spin canting for the sample prepared in argon environment is rather remarkable. Magnetization measurements of Ritter et al. [61] on $LaMnO_{3+\delta}$ ceramics having a well-controlled δ show a value of 0.11 at 5 K for $\delta = 0$ sample. However, the $\delta = 0$ samples used in their study were synthesized by deoxygenating $\delta = 0.7$ samples at 1000°C in argon environment. Similar values of μ_{eff} have also been observed in other cases when the $\delta = 0$ samples were prepared by using a deoxygenation procedure. It is likely that such samples have some traces of cation vacancies and Mn^{4+} species which contribute to the residual moment. It is therefore evident that the lowest value of δ is realized only by carrying out the entire calcination and sintering procedure in an inert gas environment as reported in this work. In the regime of H>5kG, the linear rise of M with the applied field for the oxygen deficient sample seems to be a general feature of the antiferromagnetic sample with $\delta = 0$ [36]. This type of behavior observed earlier in granular antiferromagnets has been argued to be due to the spins at the surface region of a grain [120].

5.3.2 Magnetic Behavior of $BaMnO_{3-\delta}$:

Stoichiometric $BaMnO_3$ is found to have a 2-layer hexagonal structure. The molar susceptibility of this compound as a function of temperature in the range 5K-300K is plotted in
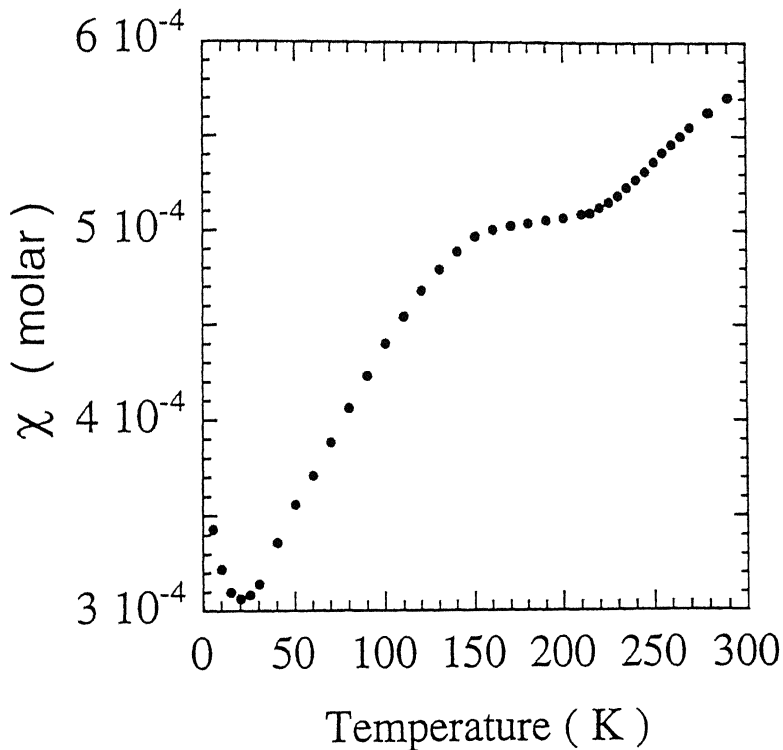
Figure 5.3: Molar susceptibility of the $BaMnO_3$ sample over the temperature range of 5-300K.

Fig.5.3. In this range of temperature, the data do not show any indication of a Curie-Weiss type of behavior. Although the data do not exhibit a well defined Neel temperature, the broad hump in susceptibility centered around 150K suggests antiferromagnetic ordering of the Mn^{4+} spins. At temperature below ~20K, the rise in susceptibility is indicative of a glassy behavior. Earlier measurements of susceptibility of this compound have shown varied results depending on the purity of hexagonal stacking of BaO_3 planes. Our susceptibility value in the vicinity of room temperature is comparable to the measurements of Christensen and Ollivier [59] and that of Chamberland et al. [54]. Neutron diffraction measurements of Christensen and Ollivier [59] indicate partial antiferromagnetic ordering of Mn^{4+} spins below 150K. However, their susceptibility data do not show the characteristic cusp-like behavior of χ for antiferromagnetic ordering. Chamberland et al. also suggested a T_N ~150K for this compound.
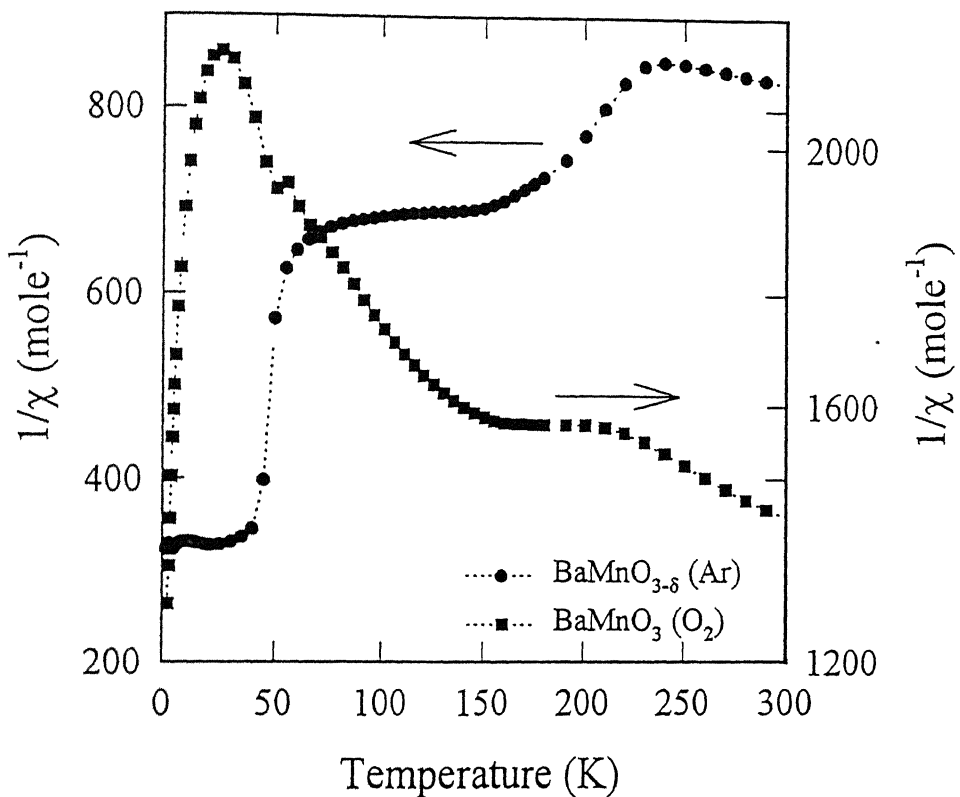
Figure 5.4: The inverse molar susceptibility for the oxygen deficient $BaMnO_{3-\delta}$ sample prepared in argon and stoichiometric $BaMnO_3$ prepared in oxygen environment.

The inverse molar susceptibilities of the oxygen deficient $BaMnO_{3-\delta}$ sample prepared in argon and stoichiometric $BaMnO_3$ prepared in oxygen environment in the temperature range 2K-300K are plotted in Fig.5.4. The data for oxygen deficient compound show two ordering temperatures. The inflection point at ~150K is common for both the compounds which is most likely due to antiferromagnetic ordering of Mn^{4+} spins. However, the moment for the oxygen deficient compound is higher than that for the stoichiometric compound. This may be due to some canting of the Mn^{4+} spins. At lower temperature (~50K), a ferromagnetic ordering is observed in the oxygen deficient compound. The moment in this regime of temperature show hysteresis. The likely origin of the FM behavior is the Mn^{3-} ions formed due to the removal of oxygen and the ensuing double exchange between Mn^{3-} and Mn^{4+} ions. The ferromagnetic ordering, however, will be confined to the Mn^{3+}-Mn^{4-} spin clusters formed around the oxygen vacancies. The observation of a sudden increase in

the moment of BaMnO$_3$ prepared in oxygen environment below $\sim$20 K may also be due to the Mn^{3+}-Mn^{4+} clusters which might exist in the system although it is a fully oxygenated compound.

5.3.3 Magnetism in La$_{1-x}$Ba$_x$MnO$_3$, (0<x<1) :

The magnetization curves at 10 K of Ba-doped LaMnO$_3$ samples for both forward and reverse field sweeps are displayed in Fig.5.5. Data for samples with x<0.2 are not shown
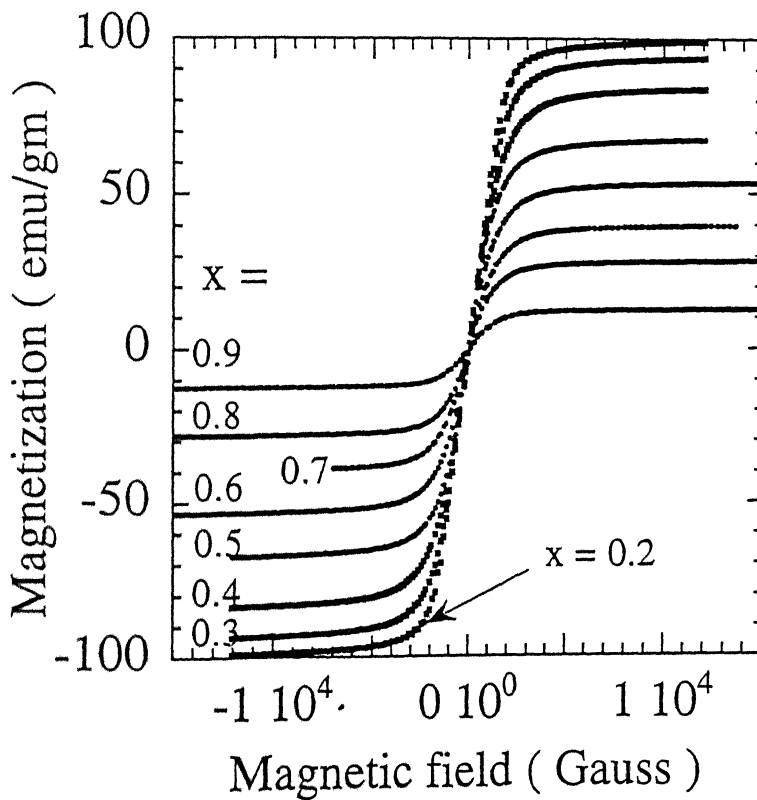
Figure 5.5: Magnetization of La$_{1-x}$Ba$_x$MnO$_3$ samples plotted as a function of applied magnetic field. Data for only a limited values of x are shown for the sake of clarity.

for the sake of clarity. The saturation magnetizations (M$_s$) has been claculated from these curves and is plotted in Fig.5.6 as a function of Ba concentration. The magnetization shows a marginal but distinct rise between x=0 and 0.2 and drop beyond x$\approx$0.35. First we focus on the drop in magnetization observed beyond x=0.35. Our x-ray and micro-Raman measurements on samples with x$\geq$0.35 show a two phase material consisting of cubic La$_{0.65}$Ba$_{0.35}$MnO$_3$ and hexagonal BaMnO$_3$ [113] as discussed in Chapter 3 and 4 re-
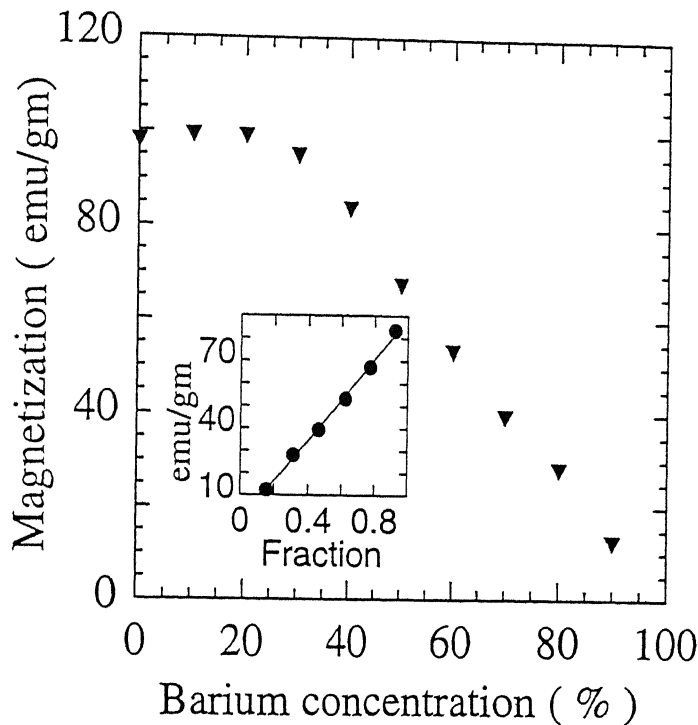
Figure 5.6: Saturation magnetization in units of emu/gm of the $La_{1-x}Ba_xMnO_3$ samples plotted as a function of barium concentration. Inset shows how the moment scales with the fraction of the ferromagnetic phase present in the two-phase region.

spectively. Since the magnetic moment on $BaMnO_3$ is negligible compared to the ordered moment on the cubic phase $La_{0.65}Ba_{0.35}MnO_3$, it is reasonable to argue that the measured signal in the samples with $x \geq 0.35$ is entirely due to the latter phase. This assumption is supported by the observation that the magnetic moment at 10K of the mixed phase samples scales with the fraction of $La_{0.65}Ba_{0.35}MnO_3$ present in the two phase region (see inset of Fig.5.6). Figure 5.7 shows the value of magnetic moment in units of Bohr magneton calculated from the saturation magnetization data under the assumption that for $x \leq 0.35$ every manganese ion contributes to the moment and for $x > 0.35$ the ferromagnetic moment arises only from the fraction of $La_{0.65}Ba_{0.35}MnO_3$. Assuming that all 3d electrons of Mn^{3+} and Mn^{4+} ions which are 4 and 3 respectively are aligned ferromagnetically and the concentration of Mn^{4+} in the range $0 < x \leq 0.35$ is given by the value of x alone, one can calculate the saturation moment as
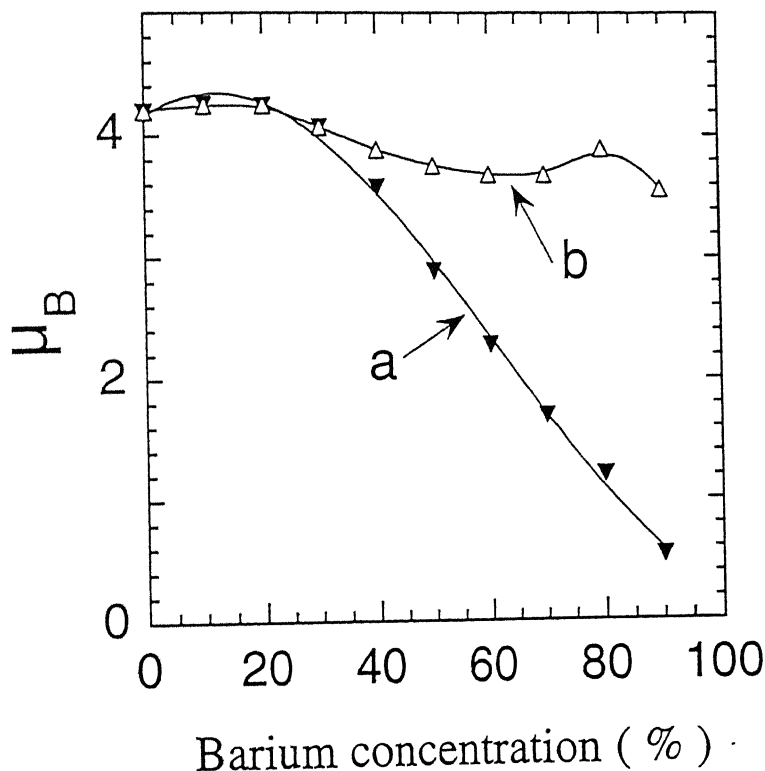
Figure 5.7: Magnetic moment in μ_B per Mn ion; Curve 'a' under the assumption that the entire composition range is a homogeneous ferromagnetic system and curve 'b' after taking into account phase separation at x=0.35. Solid lines are guide to the eye.

$$\mu_{sat}(Cal) = (1-x)\mu_{sat}(Mn^{3+}) + \mu_{sat}(Mn^{4+}).$$

This results in a monotonically decreasing curve for μ_{sat} (Cal) in the range of Ba concentration where a single phase is formed. In Fig.5 7, curve 'a' represents the moment in μ_B per Mn ion assuming the entire composition range is a homogeneous ferromagnetic system and curve 'b' after taking into account the phase separation at x=0.35. There are two factors which may contribute to deviations from this simplified picture for the saturation moment of the single phase material. The first has bearing on the possible cation vacancies in the material which will lead to some hole doping. This situation is similar to that of oxygen rich $LaMnO_{3+\delta}$. Secondly, since the ferromagnetic ordering in these manganites is a consequence of Zener-Hasegawa-Anderson double exchange [62, 71] mediated by the itinerant
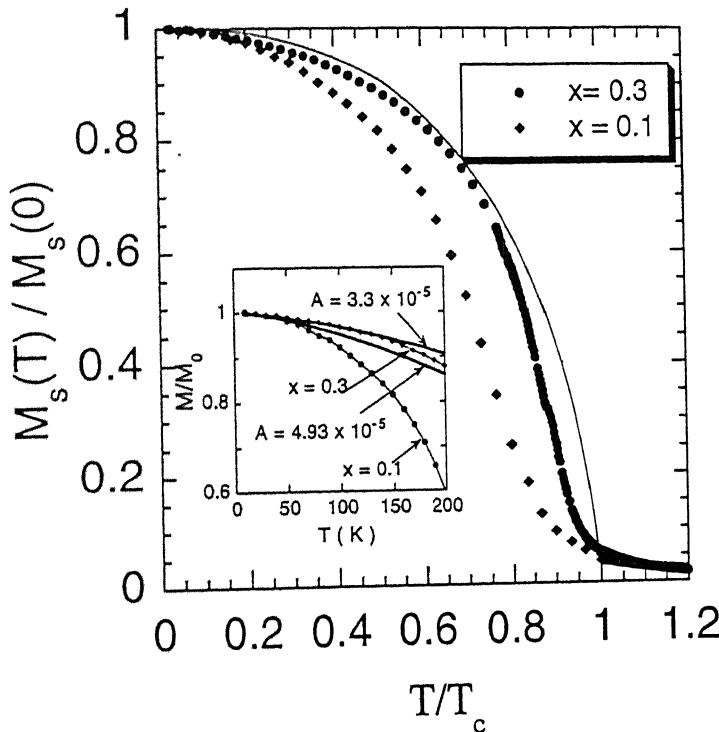
Figure 5.8: Variation of the reduced saturation magnetization with the reduced temperature for two single-phase samples with x=0.1 and 0.3. The solid line is the mean-field behavior of magnetization for a S=2 system. Inset compares the measured magnetization with the prediction of the Bloch theory.

hole in oxygen 2p band which aligns local Mn^{3+} moments ferromagnetically, there must be a minimum concentration of the holes required for the itinerancy. While the possible cation vacancies in $La_{1-x}Ba_xMnO_3$ will contribute to some holes as they do in the case of $LaMnO_{3+\delta}$, remaining holes must come from doping with the Ba. The slow rise of μ_{sat} at lower concentration of Ba is a manifestation of this effect.

The results of the zero-field-cooled saturation magnetization for samples with x=0.1 and 0.3 as a function of temperature are presented in Fig.5.8. The measurements were carried out in a magnetic field of 10 kG. In the case of the sample with x = 0.1, the transition to paramagnetic state is distinct in the vicinity of ~300 K. The sample with x=0.3 retains a fairly large ordered moment even at room temperature. The ordering temperature in this case is ~390K. The mean-field (MF) behavior of the saturation magnetization for a

S=2 system is also shown with a solid curve in Fig.5.8. The actual values of S for these samples is however between 2 and 3/2. While the sample with x=0.3 shows relatively small deviation from the MF behavior for T < 0.6 T$_c$, the drop of M$_s$ in the case of the sample with x=0.1 is much faster than the mean-field result. In metallic ferromagnets the sharper decrease of M$_s$ with temperature as compared to the mean-field behavior is attributed to excitation of spin waves which suppress the magnetization. The magnetization in terms of the exchange integral was introduced for the first time by Bloch [121]. The spin-wave method is applicable only in the low temperature region and the calculated saturation magnetization leads to the result

$$\frac{M_s(T)}{M_s(0)} = 1 - AT^{3/2}.$$

Where M$_s$ (T) is the saturation magnetization at a given temperature T, and M$_s$ (0) is the saturation magnetization at lowest possible temperature T~0. A is the coefficient given as:

$$A = \frac{B}{S}\left(\frac{k_\beta}{2JS}\right)^{3/2}.$$

Where B ≈ 0.059 for a simple cubic magnetic lattice, S is the total spin, and J the exchange integral. The expression for the exchange integral is given by the formula [122]

$$\frac{k_\beta T_c}{J} = \frac{5}{96}[Z-1][11S(S+1)-1]$$

One can estimate the drop in magnetization due to spin waves by calculating the coefficient A. The Curie temperatures of the samples have been calculated from the high temperature susceptibility data and the total spin S from the fractions of Mn^{3+} and Mn^{4+} spins. For the samples with x=0.1 and 0.3, the T$_c$ and S are ~300K, 1.95 and ~390K, 1.85 respectively. In addition to spin-wave excitation, for itinerant spin systems one would expect a contribution which goes as T^2 term in the magnetization due to the single-particle excitation or Stoner excitation [123].

In the inset of Fig.5.8 the measured magnetization of samples x=0.1 and 0.3 are compared with the predictions of the Bloch rule. It is evident in the figure that for T/T$_c$≤0.35

the drop in magnetization with temperature is in fair agreement with this simple spin-wave excitation approach. A better agreement with experiments should be possible if interactions between spin wave excitation are taken into consideration. Indeed, in EuO which shows an insulator-to-metal and simultaneous paramagnetic to ferromagnetic transition on cooling just as in the case of these manganites, the inclusion of dynamical effects leads to a better agreement with the spin wave theory over a broad range of temperatures [124]. However, at still higher temperature the concept of spin wave becomes irrelevant because of the short lifetime of such excitations.

5.3.4 Paramagnetic Susceptibility :

Paramagnetism is related to the tendency of a permanent magnet to align itself in the direction of magnetic field such that its dipole moment is parallel to the field. A paramagnetic substance has a non-vanishing angular momentum. It may also be the permanent moment of unfilled atomic shells that arises from a combination of spin and orbital moment. From the quantum mechanical treatment of paramagnetism, the general expression for magnetization for j=1/2, the spin-only case, is given by

$$\frac{M}{M_s} = tanh(a) \tag{5.1}$$

where $a = \frac{gj\mu_B H}{k_B T}$, g is the spectroscopic splitting factor, j the spin, and H the applied field. For a small value of 'a', the Eq.[5.1] reduces to

$$\chi = \frac{N\mu_{eff}^2}{3k_B T} = \frac{C}{T} \tag{5.2}$$

where μ_{eff} is the effective moment given by g [j $(j+1)^{1/2}$] μ_B and C is the Curie constant given by $\frac{N\mu_{eff}^2}{3k_B}$, which is known as Curie's law. In a solid, where interactions between the atomic/ionic moments are observed, the paramagnetic susceptibility is described by the Curie-Weiss law;

$$\chi = \frac{C}{T - \theta}. \tag{5.3}$$

Here θ is called the Curie-Weiss temperature. The Curie-Weiss θ is related to the
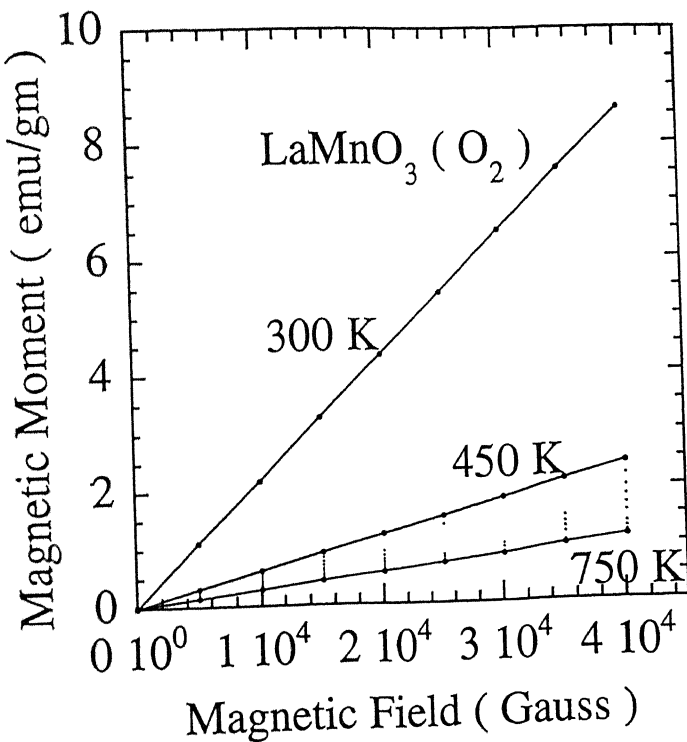
Figure 5.9: Plots of magnetization (emu/gm) versus applied magnetic field for the LaMnO₃ (O₂) sample at several temperatures in the paramagnetic regime.

strength of the interaction between moments, and its sign depends on whether the interaction helps to align adjacent moment in the same direction or opposite to one another. For $\theta > 0$ there is a net ferromagnetic interaction between the moments and for $\theta < 0$, the interaction is antiferromagnetic.

In order to establish the true paramagnetic moment on Mn^{3+} and Mn^{4+} ions, we have carried out the measurements of paramagnetic susceptibility using the high temperature stage of the SQUID magnetometer. Figure 5.9 shows the magnetic moment of a LaMnO₃ sample prepared in oxygen as a function of applied magnetic field. The data have been taken at 300K and in the interval of 25K between 450-750K. Similar measurements have been performed for the samples with $0 < x \leq 1$.

The typical Curie-Weiss plots of magnetic susceptibility for the distinct single-phase compounds with x=0, 0.1, 0.2 and 0.3 are shown in Fig.5.10. The paramagnetic moment
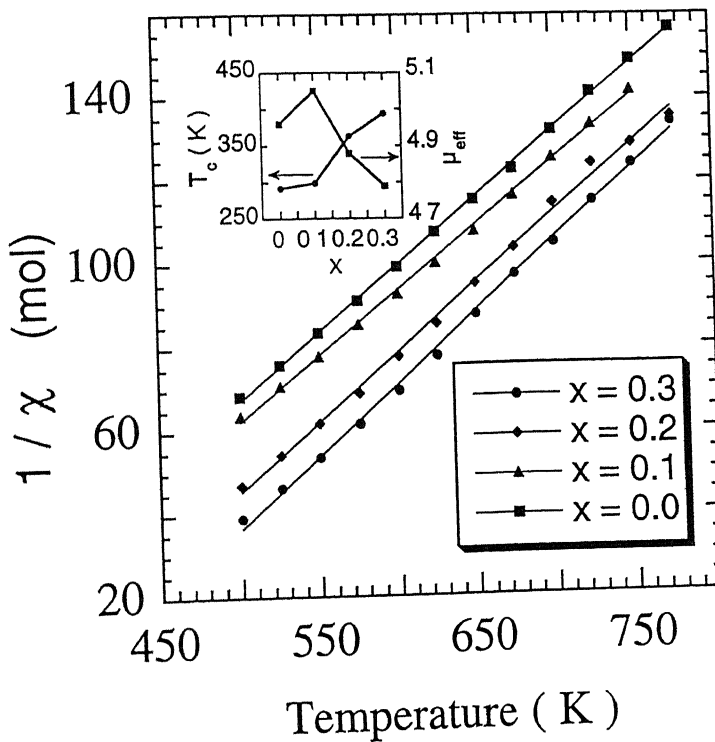
Figure 5.10: $1/\chi$ versus temperature plots for the single-phase La$_{1-x}$Ba$_x$MnO$_3$ sample. Inset shows the behavior of T$_c$ and μ_{eff} deduced from the plots.

present due to the Mn-ions and the Curie temperature T$_c$ are calculated from these data. Considering the spin-only contribution of the unpaired 'd' electrons in Mn 3d shell to the paramagnetic susceptibility, the effective moment per Mn^{3+} and Mn^{4+} ions is expected to be 4.9 μ_B and 3.87 μ_B respectively. The inset of Fig.5.10 shows the values of T$_c$ and μ_{eff} calculated from the Curie-Weiss fits to the high temperature susceptibility data. The value of effective moment decreases from 4.9 to 4.7 on increasing the x from 0.1 to 0.3. The μ_{eff} for the LaMnO$_{3+\delta}$ sample prepared in oxygen is ~4.8. While these values are considerably higher than what is expected from a quenched orbital angular momentum picture for μ_{eff}, they are in excellent agreement with measurements of Topfer and Goodenough [21] on LaMnO$_3$ and AC susceptibility data of Dabrowski *et al.* [47] on La$_{1-x}$Ba$_x$MnO$_3$. The Curie-Weiss temperature increases with Ba substitution and reaches a peak value of 390K for the sample with x=0.3. The increase in T$_c$ with substitution by divalent elements at the
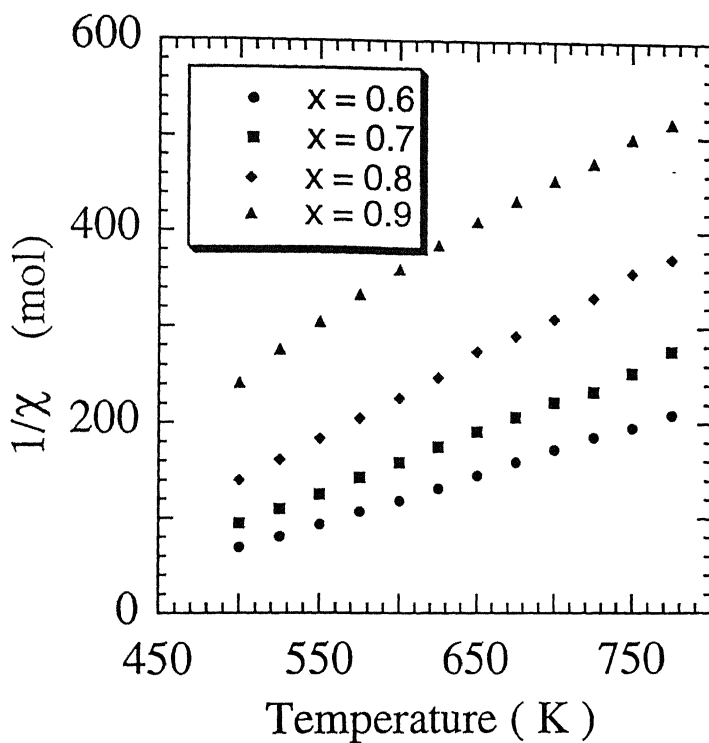
Figure 5.11: $1/\chi$ versus temperature plots for the samples which consist of two distinct crystallographic phases.

trivalent La-sites is a general feature of $R_{1-x}A_xMnO_3$ manganites. Rodriguez and Attfield [125] have estimated a maximum T_c of 530K at x=0.3 which is reduced considerably due to local distortion and stress induced in the structure as a result of the variations in the type of A site ions.

The high temperature susceptibility of the two-phase system (for x≥0.35) shows deviations from a Curie-Weiss type of behavior. As we see in Fig.5.11, the deviation increases as we approach the higher values of x. For the two-phase region, it is tempting to argue that the net susceptibility would be a weighed average of the susceptibility of the two phases. Based on this argument, we have calculated the χ of $BaMnO_3$ phase from the measured temperature dependence of χ for the samples with x=0.6 to 0.9. The rule of fraction yields;

$$\chi_B = \frac{1}{x}\left[\chi_x - (1-x)\chi_A\right]$$
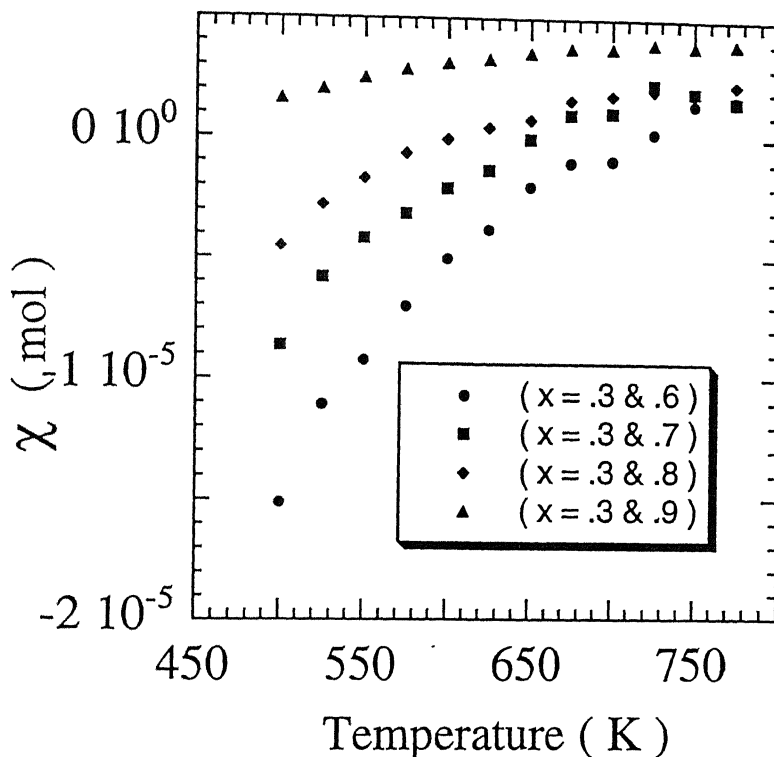
Figure 5.12: The paramagnetic susceptibility of $BaMnO_3$ at different temperature deduced from the susceptibility of $La_{0.65}Ba_{0.35}MnO_3$ and two-phase $La_{1-x}Ba_xMnO_3$ (x=0.6, 0.7, 0.8, and 0.9) using a simple effective medium approach.

where χ_A, χ_B, and χ_x are molar susceptibilities of $La_{0.65}Ba_{0.35}MnO_3$, $BaMnO_3$ and $La_{1-x}Ba_xMnO_3$ respectively. Figure 5.12, shows χ_B calculated from the data for samples with x=0.6, 0.7, 0.8, and 0.9. This analysis does not lead to a unique value for $BaMnO_3$ phase. It is therefore clear that a simple macroscopic effective medium approach for defining the susceptibility does not work in this case. A physically meaningful approach should take into account the variations in local fields and the behavior of Mn^{4+} spins at the interface between $BaMnO_3$ and $La_{0.65}Ba_{0.35}MnO_3$ grains.

5.3.5 Superparamagnetism in Two-Phase Region :

The magnetic behavior of granular systems consisting of ferromagnetic particles uniformly distributed in a non-magnetic host has been of considerable interest since the fifties when some pioneering work was done in this area [120]. The $BaMnO_3$ rich two-phase mixture

of La$_{1-x}$Ba$_x$MnO$_3$ in which the ferromagnetic compound La$_{0.65}$Ba$_{0.35}$MnO$_3$ coexists as a minority phase with BaMnO$_3$ offers a similar system. If the size of the ferromagnetic particles is sufficiently small, the ordered state will have a single domain in which Mn^{3+} and Mn^{4+} spins are aligned in the same direction across the volume of the particle. The net magnetization of such an assembly of particles can be highly sensitive to temperature. As long as the thermal energy remains smaller than the magnetic anisotropy energy, the saturation magnetization of the system will be the same as that of the bulk sample. Above a critical temperature known as the blocking temperature, the thermal energy becomes sufficiently large to cause a Brownian rotation of the direction of magnetization in the particles. The net moment of the sample in the presence of a field is then given by a Boltzman distribution of individual moments in the field direction just as in the case of a paramagnet. The average fraction of the moment in the direction of the field is

$$\frac{\bar{\mu}}{\mu} = \frac{\int (\mu.\mathbf{H}/\mu H)exp(-\mu.\mathbf{H}/k_BT)d\Omega}{\int exp(-\mu.\mathbf{H}/k_BT)d\Omega} \qquad (5.4)$$

where μ is the total magnetic moment of the particle, and $\bar{\mu}$ is the macroscopic average moment. Here, the integration is over all solid angle Ω and exp (-μ.H/k_BT) is proportional to the probability that μ lies within an element of solid angle dΩ relative to **H**. This result is well known Langevin function

$$\frac{\bar{\mu}}{\mu} = L(\mu H/k_BT) = coth(\mu H/k_BT) - k_BT/\mu H. \qquad (5.5)$$

Thus the magnetization behavior of an assembly of single domain particles in thermodynamic equilibrium at all fields is identical with that of atomic paramagnetism except that in the former case extremely large moment is involved. Such thermal equilibrium behavior of the macroscopic moments is termed as 'superparamagnetism' [126]. This behavior has also been discussed in the literature under several other names *e.g.* 'apparent paramagnetism' [127], 'collective paramagnetism' [128], 'quasiparamagnetism' [129], and 'subdomain behavior' [130]. Now, we examine the possible existence of a superparamag-
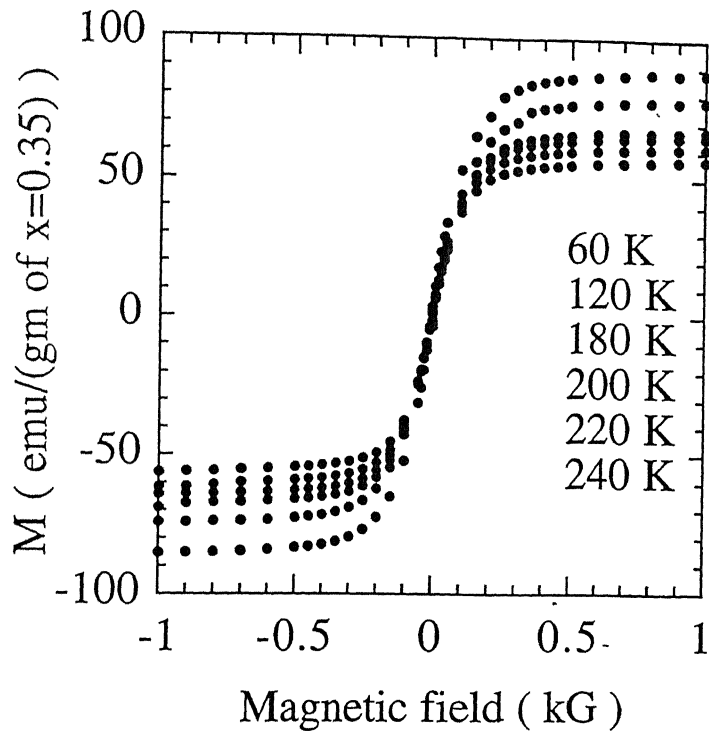
Figure 5.13: Magnetic moment of the ferromagnetic phase (x=0.35) at different temperatures in a two-phase sample of x=0.8 plotted as a function of applied magnetic field.

netic behavior in the Ba-doped lanthanum manganites with x=0.8. The hysteresis curves of $La_{0.2}Ba_{0.8}MnO_3$ at several temperatures between 50K and 240K are shown in Fig.5.13. The saturation magnetization per gram of the phase $La_{0.65}Ba_{0.35}MnO_3$ in this two-phase ceramic at 10 K is same as that of the single phase system with $0.3 \leq x < 0.35$. At temperatures above ∼150 K however, the $M_s(T)$ value of the two-phase mixture starts dropping compared to the value for the single phase material. Above this temperature, the magnetization of the sample with x=0.8 is also fully reversible. These observations suggest that the blocking temperature for the system is in the vicinity of 150 K. Following Jacobs and Bean [120], an operational defition of superparamagnetism should include atleast two requirements. First the magnetization curves should have no hysteresis and second for a non-interacting and isotropic system, the magnetization curves must be temperature dependent to the extent that curves taken at different temperatures must superimpose
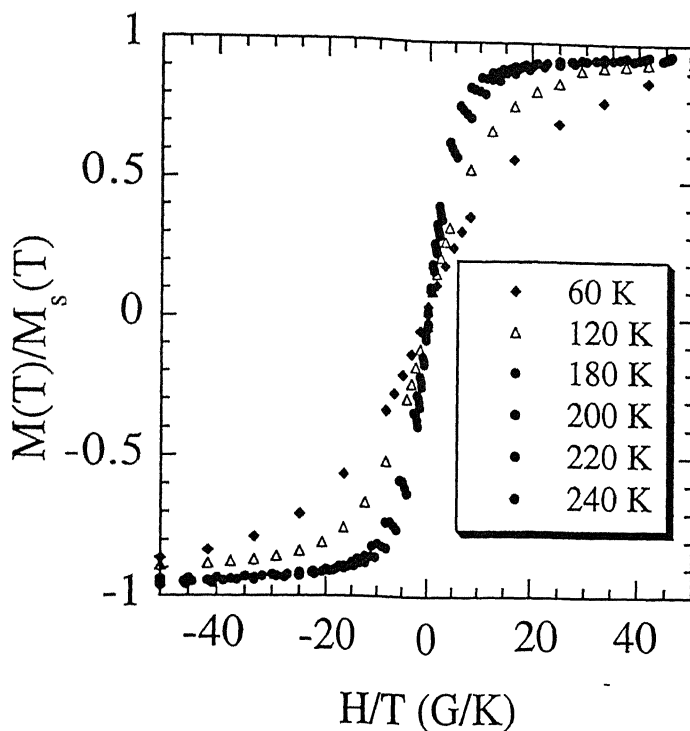
Figure 5.14: H/T superposition of the data shown in Fig.5.12, indicating a superparamagnetic behavior for T≥150K.

when plotted against H/T after correction for the temperature dependence of spontaneous magnetization. In Fig.5.14, we show the H/T superposition of the hysteresis data shown in Fig.5.13. It is evident from the figure that the magnetic behavior of $La_{0.2}Ba_{0.8}MnO_3$ at temperature above ∼150K where a clear H/T superposition is seen, indicates superparamagnetism. We expect this behavior to cover a broader range of temperature in samples with x≥0.8. On the other hand, a bulk ferromagnetic behavior will prevail below the ordering temperature as size of the ferromagnetic particle becomes larger and they also coalesce at the lower values of x.

Chapter 6

Low Temperature Raman Spectra from La$_{1-x}$Ba$_x$MnO$_3$, (x = 0, 1) Compounds

6.1   Introduction

There is a growing evidence of a strong coupling between the local atomic structure, lattice vibrational and electronic degrees of freedom in La$_{1-x}$A$_x$MnO$_3$ perovskites [8, 82]. This coupling is found to play an important role in the transport properties and magnetic ordering, and particularly in the mechanism of colossal magnetoresistance [132-133]. The structural instabilities and lattice distortions present in the vicinity of the transition temperature (T$_N$ or T$_c$) can be better understood by carrying out a temperature dependent study of various phonon modes present in this material. Raman scattering and infrared transmission experiments are particularly important for this purpose. In order to clarify the correlation between the structural changes and magnetic transitions, we have inves-

---

tigated in detail the temperature dependence of the Raman active modes of the series $La_{1-x}Ba_xMnO_3$ and its two end members namely, $LaMnO_{3+\delta}$ and $BaMnO_{3-\delta}$. The unpolarized Raman scattering experiments were performed over a temperature range of 10K to 300K.

6.2 Experimental Details

The polycrystalline samples of $LaMnO_{3+\delta}$, and $BaMnO_{3-\delta}$ as synthesized from solid state reaction method were used in the present study. The 514.5 nm and 488 nm lines of Ar^+ laser have been used to excite the samples. The samples were mounted on the cold finger of a closed-cycle helium cryostat for measurements in the temperature range of 10-300K. The temperature of the samples was measured with a Si diode sensor, and a programmable controller was used to stabilize the temperature at a desire value. The laser beam of energy ~20 mW was focused on the surface of the sample to a spot of diameter ~10 μm. The scattered light was collected in a 90° scattering geometry as shown in Fig.2.3. The spectra were detected by a liquid nitrogen-cooled CCD array.

6.3 Anharmonicity in Light Scattering by Optical Phonons

The temperature dependence of the phonon modes can be attributed to the anharmonic terms in the vibrational potential energy of the lattice [131, 134-136]. For a system with equilibrium atomic positions

$$\vec{R}^{(0)}(l,k) = \vec{R}(l) + \vec{R}(k) \tag{6.1}$$

where $\vec{R}(l) = l_1\vec{\tau_1} + l_2\vec{\tau_2} + l_3\vec{\tau_3}$, the $\vec{\tau_i}$ are primitive translation vectors, the l_i are integers, and $\vec{R}(k)$ is a vector of the basis; the vibrational Hamiltonian can be written as

$$H = \frac{1}{2}\sum_{l,k,\alpha}\frac{1}{M_k}P_\alpha^2(l,k) + \frac{1}{2}\sum_{l,k,\alpha}\sum_{l',k',\beta}\phi_{\alpha\beta}(l,k;l',k')U_\alpha(l,k)U_\beta(l',k')$$

$$+\frac{1}{6}\sum_{l,k,\alpha}\sum_{l',k',\beta}\sum_{l'',k'',\gamma}\phi_{\alpha\beta\gamma}(l,k;l',k';l'',k'')U_\alpha(l,k)U_\beta(l',k')U_\gamma(l'',k'')$$

$$+\frac{1}{24}\sum_{l,k,\alpha}\sum_{l',k',\beta}\sum_{l'',k'',\gamma}\sum_{l''',k''',\delta}\phi_{\alpha\beta\gamma\delta}(l,k;l',k';l'',k'';l''',k''')U_\alpha(l,k)U_\beta(l',k')U_\gamma(l'',k'')U_\delta(l''',k''')+\ldots\ldots$$

$$(6.2)$$

where $\vec{u}(l,k)$ is the displacement of atom l,k from its equilibrium position and $\phi_{\alpha\beta}$, $\phi_{\alpha\beta\gamma}$, and $\phi_{\alpha\beta\gamma\delta}$ are the harmonic, cubic anharmonic, and quartic anharmonic force constants respectively. The first two terms are the harmonic Hamiltonian H$_0$. The remaining terms are the anharmonic Hamiltonian H$_A$.

One diagonalizes the harmonic Hamiltonian by means of the normal-coordinate transformation

$$\vec{u}(l,k)=\sqrt{\frac{\hbar}{2M_kN}}\sum_{\vec{q},j}\frac{\vec{W}(k\mid\vec{q},j)}{(\omega_{\vec{q}},j)^{1/2}}e^{\imath\vec{q}\cdot\vec{R}(l)}A_{\vec{q},j},\qquad(6.3)$$

$$\vec{P}=-i\sqrt{\frac{\hbar M_k}{2N}}\sum_{\vec{q},j}(\omega_{\vec{q},j})^{1/2}\vec{W}(k\mid\vec{q},j)\times e^{\imath\vec{q}\cdot\vec{R}(l)}B_{\vec{q},j}.\qquad(6.4)$$

Here $\omega_{q,j}$ is the normal-mode frequency for wave vector $\vec{q}$ and branch index j, $\vec{W}(\text{k},\mid\vec{q},\text{j})$ is the polarization vector for the normal mode, M$_k$ is the mass of an atom of type k, N is the number of unit cells in the crystal and A$_{\vec{q},j}$ and B$_{\vec{q},j}$ are the field operators.

After making the normal-coordinate transformation, the Hamiltonian becomes

$$H=H_0+H_A$$

where

$$H_0=\frac{1}{4}\sum_{\vec{q},j}\hbar\omega_{\vec{q},j}(A^\dagger_{\vec{q},j}A_{\vec{q},j}+B^\dagger_{\vec{q},j}B_{\vec{q},j})\qquad(6.5)$$

and

$$H_A=\sum_{\vec{q},j;\vec{q}',j';\vec{q}'',j''}V(\vec{q},j;\vec{q}',j';\vec{q}'',j'')A_{\vec{q},j}A_{\vec{q}',j'}A_{\vec{q}'',j''}$$

$$+\sum_{\vec{q},j.....,\vec{q}''',j'''}V(\vec{q},j;\vec{q}',j';\vec{q}'',j'';\vec{q}''',j''')A_{\vec{q},j}A_{\vec{q}',j'}A_{\vec{q}'',j''}A_{\vec{q}''',j'''}+....\qquad(6.6)$$

where V's are the harmonic coefficients. If we restrict ourselves to the cubic anharmonicity in the second order, the damping constant Γ that characterizes the peak width can be

derived as [134],

$$\Gamma(T) = A + \frac{B}{e^x - 1} \tag{6.7}$$

where A and B are constants and e^x is the Boltzmann factor $\exp(h\,\omega_0/k_B\,T)$.

If a similar argument is used for the origin of the line shift, the peak position in cm^{-1} at a given temperature can be written as,

$$\Omega(T) = \omega_0 + C\left[1 + \frac{2}{e^x - 1}\right] \tag{6.8}$$

where C and ω_0 are constants. The constants A, B, C and ω_0 are calculated by fitting these thermal model equations (6.7 and 6.8) with the experimental frequency shift and FWHM data.

6.4   Results and Discussion

In the first part of this section, we present the temperature dependence of various phonon modes of orthorhombic $LaMnO_{3+\delta}$. In a later part of this section, the temperature dependence of the phonon modes of $BaMnO_{3-\delta}$ compounds are discussed.

6.4.1   Temperature Dependence of Phonon Modes in $LaMnO_3$:

The unpolarized Raman spectra of orthorhombic $LaMnO_3$ as a function of temperature are shown in Fig.6.1. The spectra have been obtained from a spot of diameter $\sim$10 μm. There are some qualitative differences in the measurements shown in Fig.6.1 and the data taken in the microstage with a spot size of $\sim$2-3 μm. The main difference is the appearence of an additional band at 672 cm^{-1} in the spectrum of Fig.4.1 which was taken with a much larger beam spot. Since there were no impurity phases present in the material as per XRD and SEM analysis, we believe that the larger spot size is allowing Raman scattering from some grains of different orientation for which polarization selection rules allow appearence of the 672 cm^{-1} line. The Raman line at 672 cm^{-1} is also observed from some scanty distributed grains of diameter $\sim$2-3 μm. This additional band at $\sim$672 cm^{-1} has also been reported by Podobedov et al. [89] in orthorhombic $LaMnO_3$ and recently a Raman line at $\sim$ 640 cm^{-1}
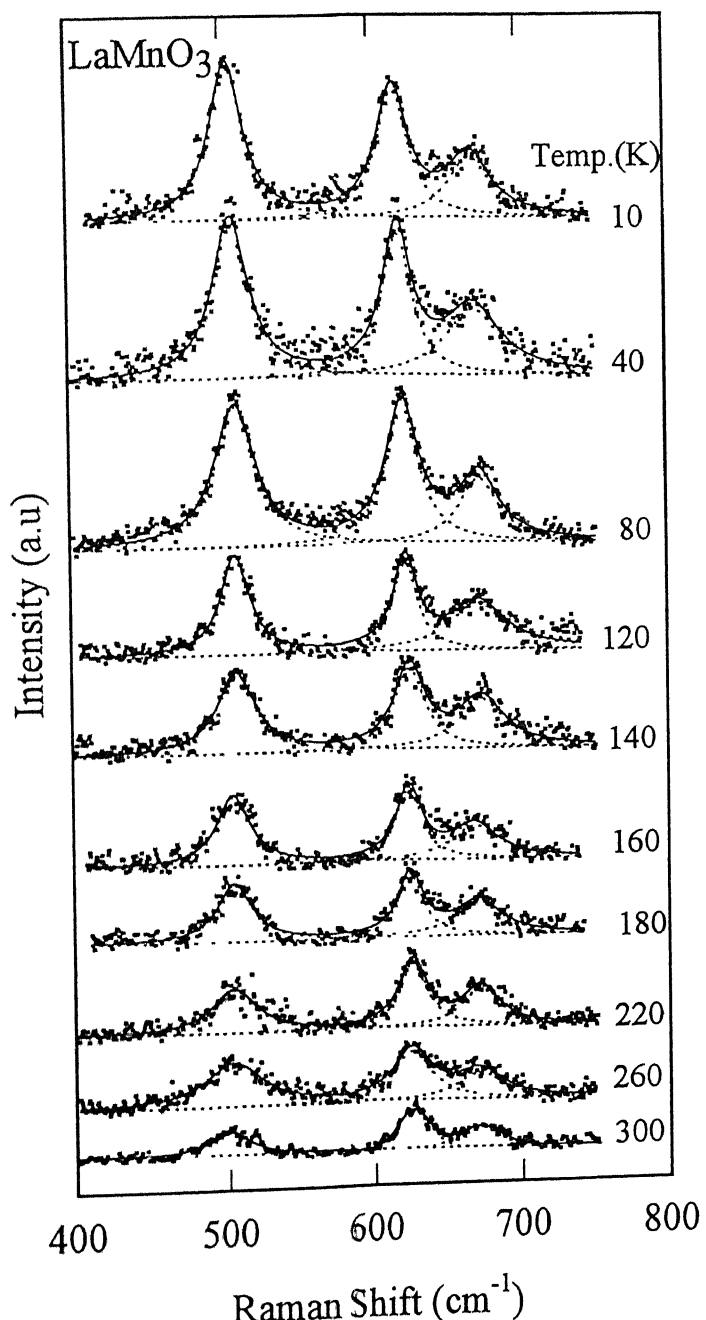
Figure 6.1: The unpolarized Raman spectra from orthorhombic LaMnO$_3$ as a function of temperature.

from rhombohedral $LaMnO_3$ has been reported by Abrasher *et al.* [137]. According to Podobedov *et al.*, the feature may be a contribution of the second order Raman process, as they obtained the same feature from Sr-doped materials for which the first order Raman modes are forbidden. However, in contrast to these results our room temperature Raman measurements of Ba-doped materials did not evolve any feature at ~ 672 cm^{-1} which can be attributed due to the second order contribution. From Fig.6.1, one observes that the intensity of all the peaks decreases gradually with rise of temperature. This indicates the reduction of orthorhombic lattice distortion as the sample gets heated. In particular, the perovskite like compound tends to have more symmetric structure *e.g.* monoclinic or cubic with the rise of temperature [42]. This is most likely due to the oxidation of some of the Mn^{3+} to Mn^{4+} ions with increase in temperature, which destroy the JT distortion in the compound. As a result of this, the structure becomes monoclinic or cubic depending on the Mn^{4+} ion content in the material. The Raman spectrum is characterized by two prominent bands at 490 cm^{-1} and 612 cm^{-1}. The peak centered at 490 cm^{-1} is due to A_g symmetry whereas 612 cm^{-1} peak can be assigned to the B_{2g} symmetry mode as discussed in Chapter 4. The variation of peak position and FWHM of 490 and 612 cm^{-1} peaks with temperature has been displayed in Fig.6.2 and 6.3 respectively. The structural changes associated with the antiferromagnetic ordering at 145K have been noticed in the phonon spectra of this compound. As the transition temperature is approached from below, the strongest line at 490 cm^{-1} of A_g symmetry mode broadens (Fig.6.3) and softens. The 490 cm^{-1} mode shows anomalous behavior below the magnetic ordering temperature (~ 150K). It does not obey the thermal model of anharmonicity of neither cubic nor quartic order contribution to the vibrational potential energy of lattice. This is evident from Fig.6.2 where the fitted curve (solid curve) to the Eq.6.8 shows a large deviation from experimental frequencies below 150 K, and indicates the stiffening of the mode. This is most likely due to the magnetic ordering at this temperature which may influence the phonon mode. The correlation of the magnetic ordering with the phonon vibrations will be discussed in the later part of this section. The temperature dependence of the peaks at 612 cm^{-1} and 672 cm^{-1} also
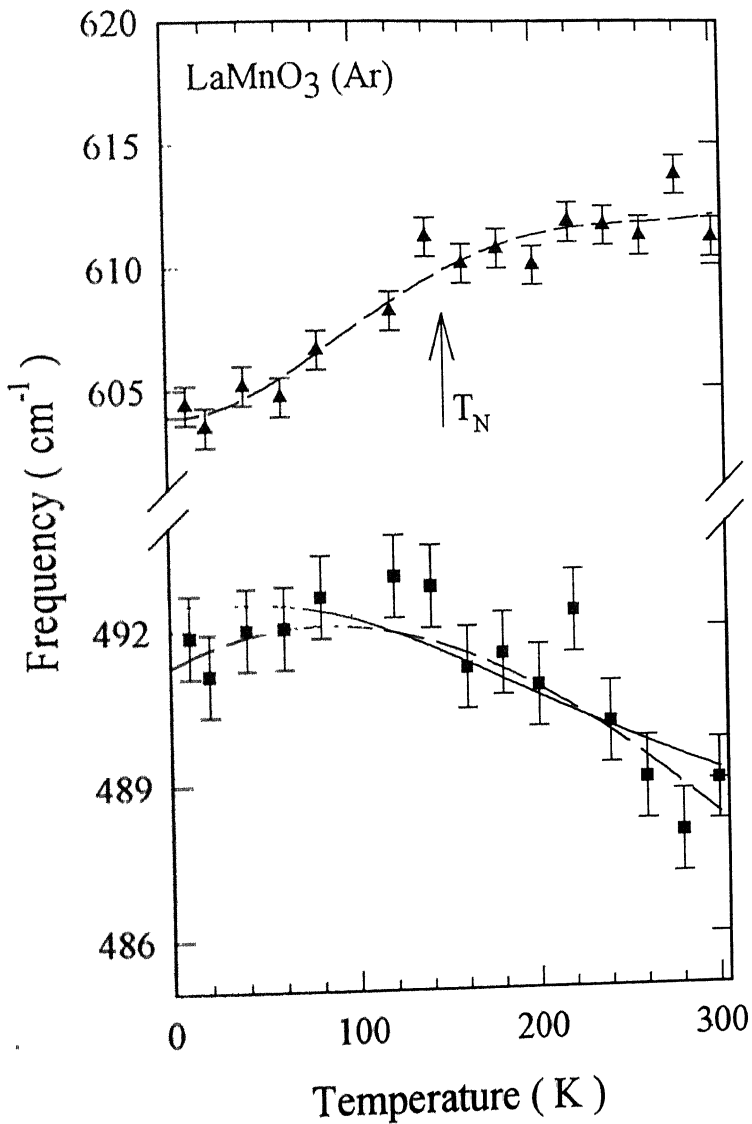
Figure 6.2: Temperature dependence of the peak positions of 490 and 612 cm^{-1} bands of orthorhombic LaMnO$_3$. The solid curve represents the thermal model curve fitting whereas the dashed curve is only an aid to the eye.
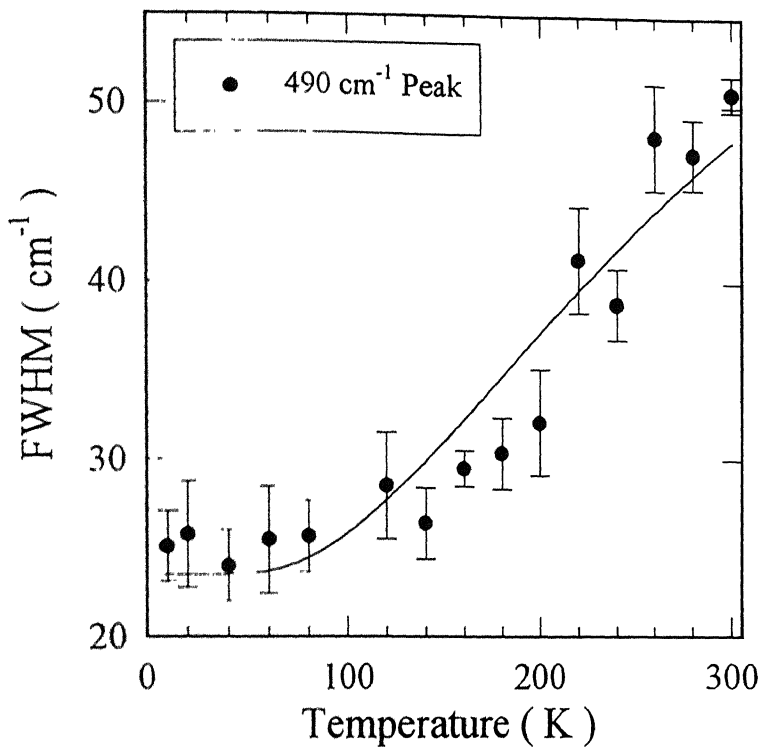
Figure 6.3: Temperature dependence of the peak width (FWHM) of 490 cm^{-1} Raman band of orthorhombic LaMnO$_3$. The solid curve is only an aid to the eye.

shows anomalies in the vicinity of the Neel temperature ($\sim$145K). The abrupt shift of these two lines towards higher wavenumber has been observed near the Neel temperature of the compound (Fig.6.2 and 6.4). While the observed anomaly in the 609 cm^{-1} mode has also been seen by Podobedov *et al.* [89], we notice a similar behavior in the mode centered around 670 cm^{-1}. The possible cause of mode stiffening seen here is the spin-lattice interaction. Neutron diffraction measurements of Huang *et al.* [60] on LaMnO$_{3+\delta}$ system show anomalies in the 'a' and 'b' lattice parameters (with the convension that c is parallel to z axis) near T_N. In Fig.6.5 we reproduce the data of Huang *et al.* It is clear from the figure that the 'a' axis lattice parameter which decreases from room temperature down to T_N following the expected thermal behavior, shows an upturn below T_N. However, the behavior of 'b' axis lattice parameter is quite different. While it increases down to 150 K, in the magnetically ordered state it is relatively temperature independent. The temperature dependence of 490 and 612 cm^{-1} Raman modes (Fig.6.2) shows a behavior
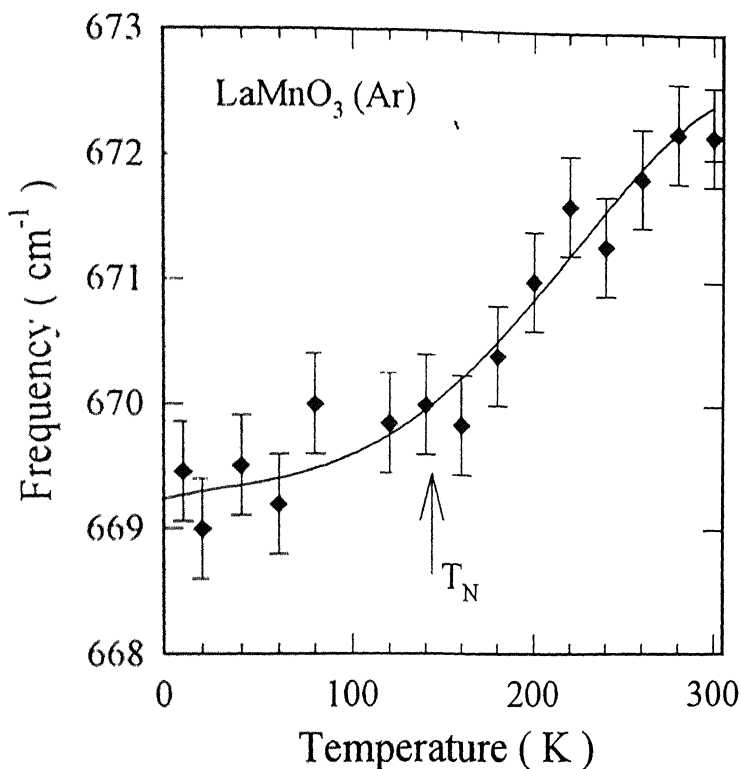
Figure 6.4: Temperature dependence of the peak position of 672 cm^{-1} Raman line of orthorhombic LaMnO$_3$. The solid curve is an aid to the eye.
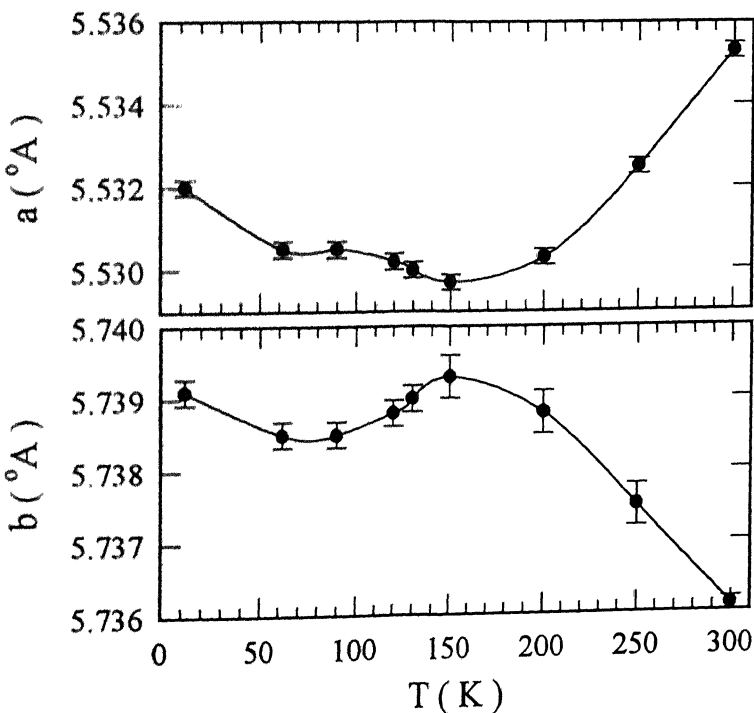
Figure 6.5: Temperature dependence of lattice parameters a and b of orthorhombic LaMnO$_3$ from neutron diffraction measurements [60]

similar to that of 'a' and 'b' lattice parameters.

6.4.2   Temperature Dependence of Phonon Modes in $BaMnO_{3-\delta}$ $(\delta \geq 0)$:

In this section we discuss the temperature dependence of the Raman modes in stoichio-metric $BaMnO_3$ and one of the oxygen deficient $BaMnO_{3-\delta}$ samples. The phonon modes of $BaMnO_3$ at low temperatures, are quite narrow. With the rise of temperature the lines broaden noticeably and also show a slight shift in frequency to the lower side. Figure 6.6 shows the behavior of Raman intensity in the spectral ranges of 370-445 cm^{-1} and 610-710
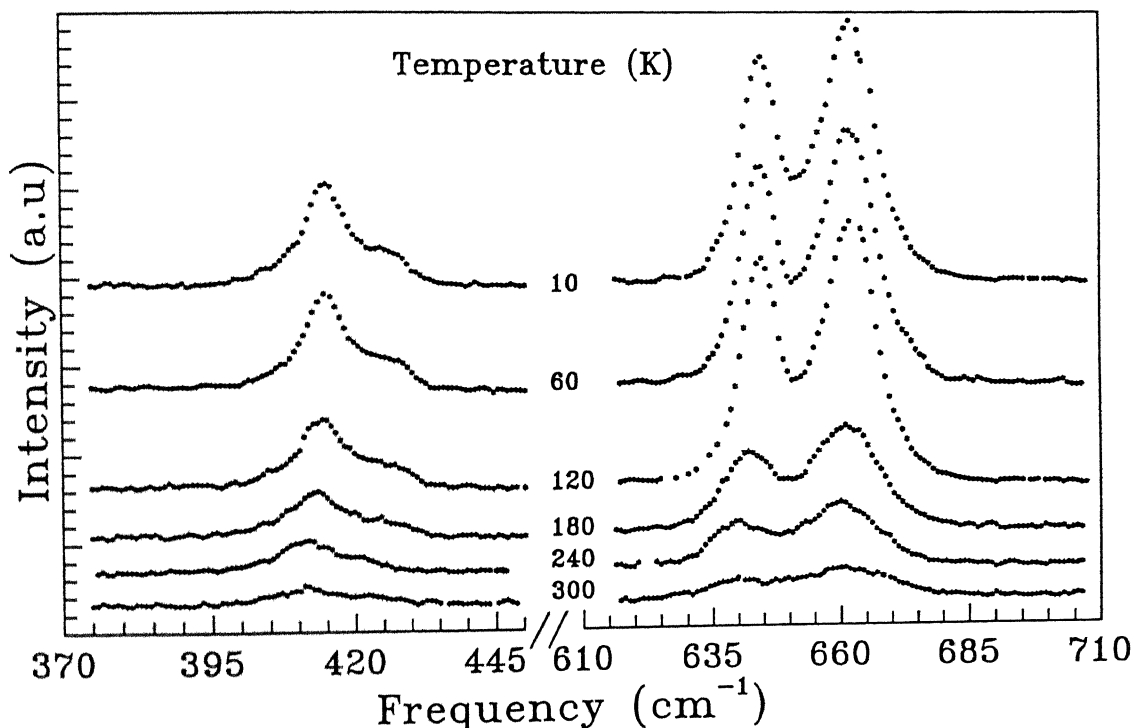
Figure 6.6: Temperature dependence of Raman lines marked as A, D, and E in Fig.4.5 of 2H-$BaMnO_3$ compound. Spectra taken only at a few temperatures are shown for the sake of clarity.

cm^{-1} at various temperatures. In these two ranges of frequencies the strongest modes marked as A, D, and E respectively in Fig.4.5 (Chapter 4) are observed. The variation of peak positions and FWHM of the peaks A and E as a function of temperature has
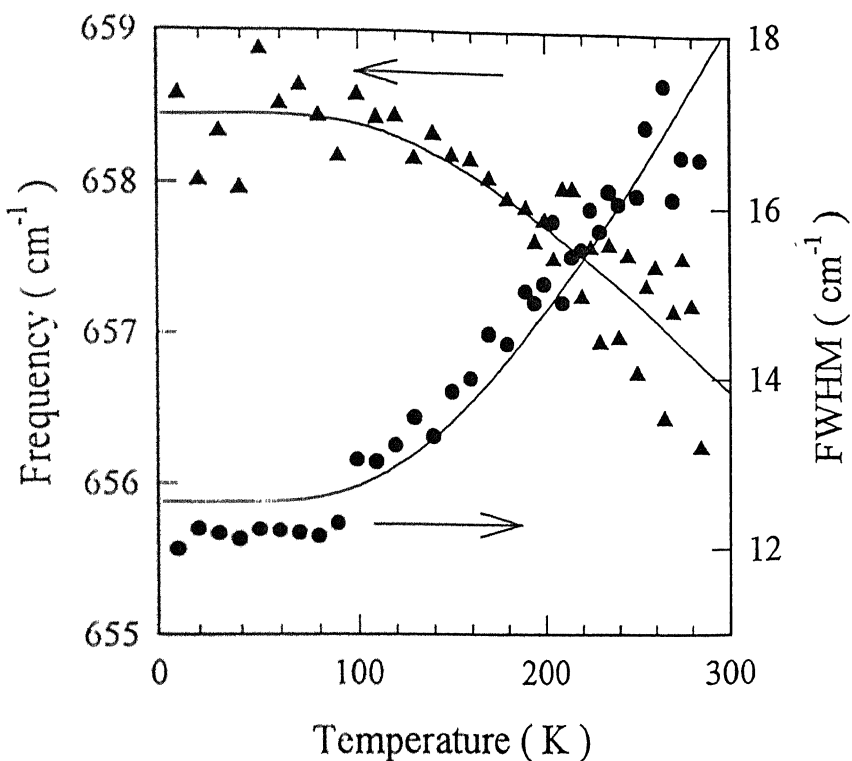
Figure 6.8: Temperature dependence of the peak position and FWHM for Raman line E of BaMnO$_3$ compound.

the contribution of scattering from 3-phonon process may be expected in this system.

The Raman spectra of oxygen deficient 15R-BaMnO$_{3-\delta}$ at various temperatures are presented in Fig.6.9. The spectral intensity of all the phonon lines decreases on heating the sample. On comparing the spectra of stoichiometric BaMnO$_3$ [Fig.6.6] and the oxygen deficient BaMnO$_3$ $_\delta$ [Fig.6.9] at the lowest possible temperature ($\sim$10 K) the following differences are noticed. Firstly, few additional phonon peaks (indicated by arrows) appear in the low temperature spectra from the oxygen deficient BaMnO$_{3-\delta}$ compound (see Fig.6.10). The increase of Raman lines in this compound is in good agreement with the group theoretical formulation for the 15R-BaMnO$_{3-\delta}$ compound. The increase of phonon modes has also been noticed in IR transmission spectra of this compound confirming the 15R phase as discussed in Chapter 4. Secondly, the phonon lines are broader in the case of oxygen deficient compound compared to the stoichiometric one. This broadening of the phonon modes is likely to be due to the increased disorder caused by the cation vacancies
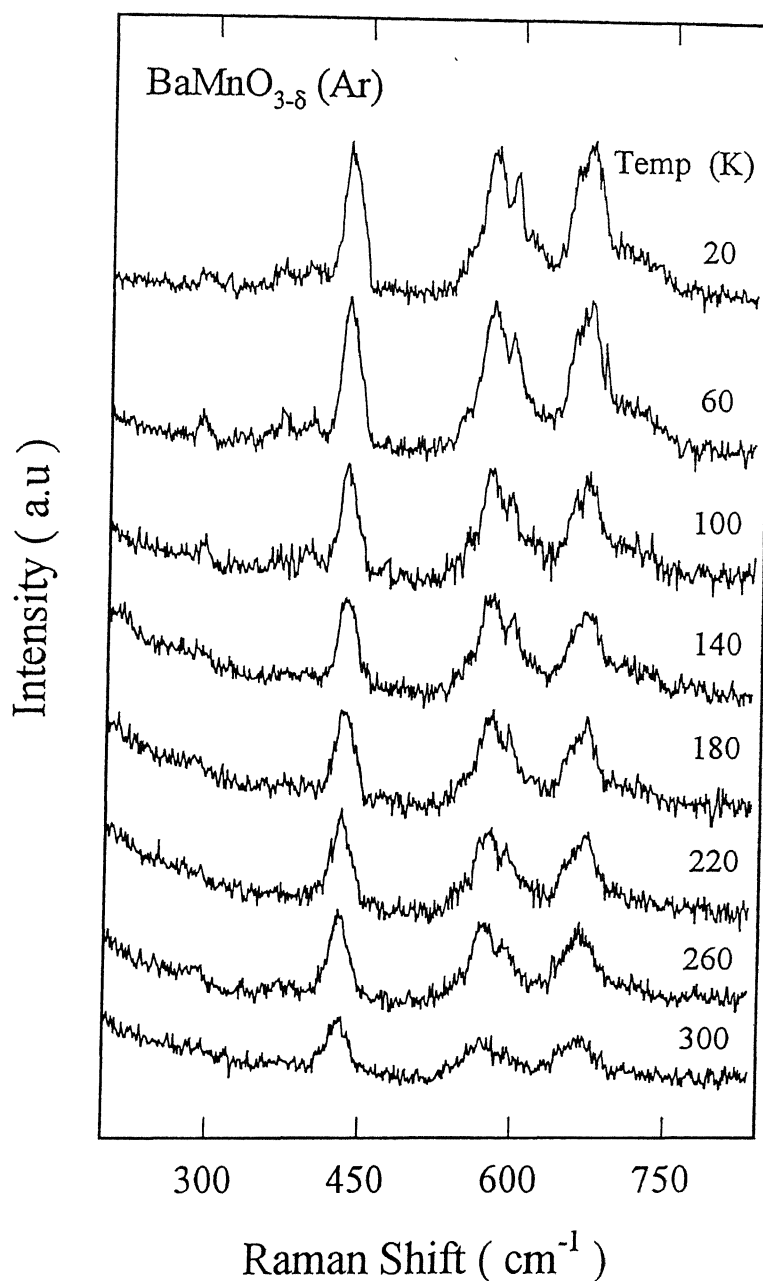
Figure 6.9: Temperature dependence of various Raman active modes from oxygen deficient $BaMnO_{3-\delta}$ compound.
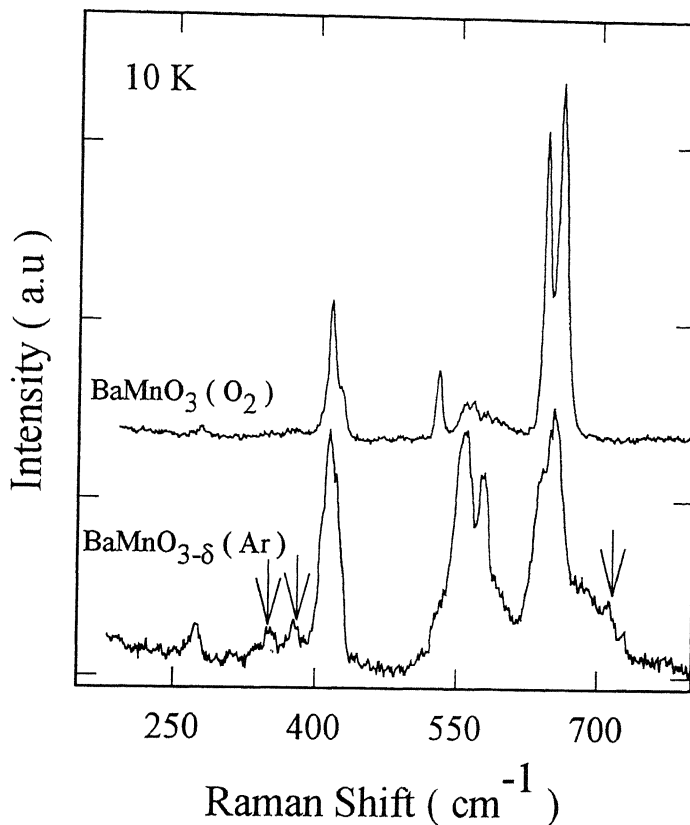
Figure 6.10: Raman spectra of 2H-BaMnO$_3$ and 15R-BaMnO$_{3-\delta}$ compounds taken at 10K with λ=514.5 nm Ar$^+$ laser line. The additional Raman lines have been marked by arrows in oxygen deficient material.

in the quenched sample. The cation vacancy disorder will also result in lowering of the peak intensities.

Another interesting aspect of the low temperature Raman spectra of oxygen deficient BaMnO$_{3-\delta}$ is the large background intensity. The background is not flat and smooth as seen in the spectra for 2H-BaMnO$_3$. One possible reason for the wavenumber dependent background could be the scattering by free carriers. As we discussed previously, with the decrease of oxygen stoichiometry in this system, some of the Mn^{3+} ions changes to Mn^{4+} ions creating holes as free carriers. A similar feature has been obtained in the Raman spectra from metallic La$_{1-x}$Ba$_x$MnO$_3$ samples with 0.25$\leq$x$\leq$0.35 (Fig.4.4) where the doped carriers are itinerant.

Figure 6.11 shows the variation of frequency and FWHM of the three stronger Raman lines centered at $\sim$412, 554, and 651 cm^{-1} respectively of the oxygen deficient BaMnO$_{3-\delta}$ as
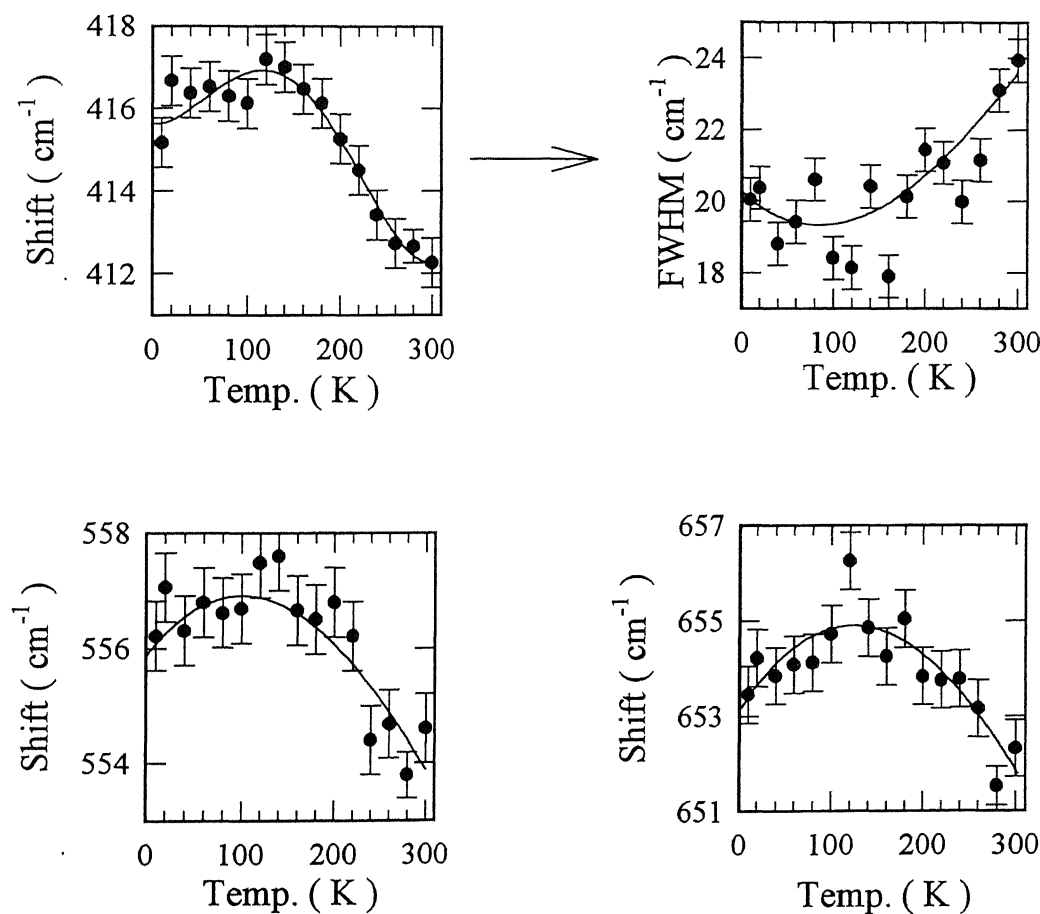
Figure 6.11: Temperature dependence of the peak positions for the three stronger Raman modes of oxygen deficient $BaMnO_{3-\delta}$ compound. The temperature variation of FWHM for one of these bands is displayed, others show the similar trend.

Chapter 7

Conclusions

To conclude, the structural and magnetic phase stability of the Ba-doped lanthanum manganite perovskite system has been investigated in detail using X-ray diffraction, Raman scattering, IR absorption and magnetization measurement techniques. The various crystallographic phases present in the system $La_{1-x}Ba_xMnO_3$ for $0 \leq x \leq 1$ were detected using the first three techniques. It has been amply demonstrated in the literature that the structural state and physical properties of perovskite related oxides are susceptible to changes in the oxygen nonstoichiometry, the range of which has been extended in many cases by adopting high pressure techniques and electrochemical methods. The oxygen nonstoichiometry in lanthanum manganite, however, can be realized by synthesizing the material in oxygen rich and oxygen deficient environments at ambient pressure following the standard solid-state route. The oxygen nonstoichiometry, in general written as δ (>0), actually represents cation vacancies in the structure rather than an excess of oxygen. For the undoped compound $LaMnO_{3+\delta}$, our Raman and IR results confirm the reported suscep-tibility of the structure of this compound to variations in δ. An increase in δ can be realized either by heating the orthorhombic phase ($\delta \simeq 0$) at temperatures as low as 600^oC or via laser annealing. The higher symmetry of the crystallographic structure achieved through oxidation is indicated by a decrease in the number of IR and Raman active phonons. The

effect of Ba substitution is similar to that of an increase in δ. The behavior of IR absorption edge and phonon modes at room temperature is indicative of an insulator-metal transition in this system as a function of Ba concentration. Our micro-Raman measurements fix the maximum solubility of Ba in cubic perovskite structure at $x \leq 0.35$. For higher values of x, a two-phase mixture of hexagonal $BaMnO_3$ and cubic $La_{0.65}Ba_{0.35}MnO_3$ is formed. The IR and Raman spectra of various polymorphic forms of $BaMnO_3$ have been measured. The observed phonon modes for $2H$-$BaMnO_3$ compounds have been compared with allowed zone-center vibrations for the space groups $P6_3mmc$ and $P6_3mc$. The correct space group for this material is established as $P6_3mc$. The temperature dependence of various Raman excitations has been measured and understood in the framework of the temperature dependent changes in the Bose population factor and anharmonicity of the lattice potential The magnetic behavior of the $La_{1-x}Ba_xMnO_3$ samples over a wide range of composition ($0 \leq x \leq 1$) has been studied. The magnetic state of the compound with x=0 depends sensitively on the extent of cation vacancies which leads to Mn^{4+} sites in this system where charge neutrality requires only Mn^{3+} ions. The orthorhombic $LaMnO_3$ samples prepared in an inert environment orders antiferromagnetically ~ 145 K, and show extremely small parasitic moment at 4.2K. The $LaMnO_{3+\delta}$ phases ($\delta \geq 0.07$) and all Ba-substituted samples for $x \leq 0.35$ order ferromagnetically. Both T_c and saturation moment increase with x for $x \leq 0.35$. Samples with $x > 0.35$ provide an interesting granular system where saturation moment scales with the fraction of $La_{0.65}Ba_{0.35}MnO_3$ cubic phase present in the alloy. At very low fraction of this ferromagnetic phase, the system shows signs of superparamagnetism.

The Ba-substituted compounds with $0 < x \leq 0.25$ exhibit in a single phase material with decreasing rhombocity. A further increase in x leads to the ideal cubic perovskite structure for which the factor group analysis yields no Raman active and three IR active phonons of F_{1u} symmetry. The structure of $LaMnO_{3+\delta}$ and $La_{1-x}Ba_xMnO_3$ for $x \leq 0.35$ goes to a state of higher symmetry as the Jahn-Teller distortion is removed with the increasing Mn^{4+} concentration. This is clearly evident from the decreasing number of phonon modes observed in IR and Raman spectra and change of the crystal structure

from orthorhombic to rhombohedral and from rhombohedral to cubic as seen through X-ray diffraction measurements. These changes are accomplished through a local adjustment of bond angles and bond lengths without involving large scale diffusion of cations in the material. Such a large scale motion of atoms, however, occurs for $x \geq 0.35$ where we see the formation of two distinct crystallographic phases *viz.* $La_{0.65}Ba_{0.35}MnO_3$ and hexagonal $BaMnO_3$ respectively. The phase separation is triggered by the fact that the long range cubic perovskite order is unable to accommodate the larger divalent ion (Ba^{2+}) at a large number of La^{3+} sites.

It is generally seen that Raman frequencies of perovskite oxides in the lower wave number (< 450 cm^{-1}) depend on the type of the rare earth element, whereas for $\nu > 450$ cm^{-1}, the internal vibrations of the oxygen octahedra incasing the transition metal ion dominate the spectrum. For $LaMnO_{3+\delta}$ the most intense internal vibration at 612 cm^{-1} [Fig.4.1] is due to inphase stretching motion of oxygen atoms in the ab plane. The second intense peak at 490 cm^{-1} is of A_g symmetry involving out of phase bending motion of oxygen atoms in the octahedra. Since these modes are forbidden for the rhombohedral and cubic phases structure, their position and intensity must reflect the extent of orthorhombic distortion of the structure.

The continuous absorption with an onset at ~ 500-600 cm^{-1} and of increasing intensity as we go to higher wave numbers has been observed in the IR transmission spectrum of orthorhombic $LaMnO_3$, perhaps involves interband electronic transitions. Electronic calculations [138] for $LaMnO_3$ suggest that the lowest energy band-to-band excitation in this system would involve transitions between the JT split $e_g^1 \uparrow$ and $e_g^2 \uparrow$ bands. The $e_g^1 \uparrow$ band overlaps with O 2p band due to strong hybridization, while $e_g^2 \uparrow$ band forms the lowest lying empty conduction band. Optical reflectivity measurements of Jung *et al.* [139] indicate that the center of gravity (CG) of the $e_g^1 \uparrow$ and $e_g^2 \uparrow$ bands are separated by ~ 1.9 eV. The extrapolated value of the absorption edge in the present case is ~ 0.06-0.07 eV. The lower energy of the edge as compared to the band-to-band separation of 1.9 eV is understandable in view of the fact that absorption edge is a measure of the separation

between band edges rather than the band CGs. In the present case, the separation is also susceptible to small variations in oxygen concentration in the sample. It is also important to point out that the observation of a gap is consistent with the reported semiconducting behavior of $LaMnO_3$. The shift of the absorption edge to lower wave numbers as the oxygen concentration is increased or as lanthanum is replaced by barium suggest a lowering of the energy gap and an eventual insulator-to-metal transition in the system. While a correct determination of the edge becomes difficult due to overlap of electronic and phonon parts, the trend is quite clear in our IR data. This type of behavior of the absorption edge is observed in many doped perovskite systems such as $La_{1-x}Ba_xCuO_4$ and $LaNi_{1-x}Cr_xO_3$. For $La_{1-x}Ba_xMnO_3$, while a systematic study of the insulator-to-metal transition as a function of x is lacking, from a comparison with Sr and Ca doped systems this transition should occur in the vicinity of $x\simeq0.18$. Another remarkable effect of the increased hole concentration in the system is on the behavior of the phonon modes. While some of the modes become forbidden because of the raising of the crystal symmetry, the modes which remain show a considerably lower intensity on increasing the x. A stricking similar behavior of phonon modes has also been seen in hole doped La_2CuO_4 [140-141], and in some doped nickolates and the low T_c oxide superconductor $BaPb_{1-x}Bi_xO_3$ [142].

The magnetic measurements show that the ordered moment on $LaMnO_{3+\delta}$ depends sensitively on the processing conditions and lowest value of 0.006 μ_B per Mn ion at 4.2 K is realized in the antiferromagnetic compound of $\delta = 0$. The compounds of $0.07\geq \delta \geq0.04$ show large ordered moment at low temperature. This is not due to spin canting but a result of double exchange between Mn^{3+}-O-Mn^{4+} ions which form magnetic clusters. Compounds with $\delta \geq0.07$ are well defined double exchange ferromagnets. The Ba-substituted compounds order ferromagnetically with a monotonic increase of T_c and M_s with x<0.35. In the two-phase region, M_s scales with the fraction of the ferromagnetic phase present in the sample. Magnetic granularity, superparamagnetism and an effective medium approach for susceptibility of the two-phase mixtures in this system are also studied for the first time. The complex magnetic behavior of $BaMnO_3$ suggests antiferromagnetic ordering

below $\sim$150 K. The oxygen deficient $BaMnO_{3-\delta}$ sample shows two ordering temperatures. The inflection point at $\sim$150 K is most likely due to antiferromagnetic ordering of Mn^{4+} spin, whereas a ferromagnetic ordering is observed at lower temperature ($\sim$50 K).

The temperature dependence of frequency and linewidths of various Raman active modes in case of $LaMnO_{3+\delta}$ and $BaMnO_{3-\delta}$ samples is measured. The anomalous behavior of certain phonon frequencies at the magnetic transition temperature of $LaMnO_3$ compound has been noticed and correlated with the onset of antiferromagnetic ordering effect. The temperature dependence of phonon modes for the 2H- $BaMnO_3$ samples has been attributed to the anharmonic terms in the vibrational potential energy of the lattice. As a results of which the Raman spectra from 2H compound are expected to have contribution of 3-phonon scattering processes.

7.1 Future Scope of the Work

The scientific and commercial interest in the hole doped rare-earth manganites has grown continuously during the last few years. It is very clear that the average ionic radius of A-site in the $AMnO_3$ system plays a key role in establishing the interplay between magnetic, Coulomb and lattice interactions. The A-site radius can be varied in a controlled manner through a suitable choice of the rare-earth and the dopant alkaline earth elements. While some priliminary work in this direction has started appearing in the literature, there is considerable scope for further studies.

The literature survey of the rare-earth manganites shows little evidence of lattice dynamic studies. The lattice effects play an important role in carrier transport and magnetism in these materials. The Jahn-Teller instability of the MnO_6 octahedra is responsible for various structural transformations. Raman scattering is known to be a powerful technique to study the dynamical processes caused by phonons, charge carriers and spins that may effect the magnetoresistance. Particularly, the polarization measurements that can be made with small high-quality single crystals provide a description of anisotropy of the above processes, information that may be inaccessible by other techniques. It will be inter-

esting to study the polarized Raman spectra of $La_{1-x}Ba_xMnO_3$ single crystal. The correct mode assignment would be possible using the room temperature polarized spectra. The influence of magnetic ordering on a particular Raman active mode and its variation with temperature can be studied more easily after a detailed analysis of the polarized Raman spectra of the material.

The real space ordering of Mn^{3+} and Mn^{4+} ions (charge ordering) is another exciting area where Raman studies can provide very useful information. The charge ordering (CO) effect is strongly influenced by the average radius of A-site cations $<r_A>$. In manganites for $x \sim \frac{1}{2}$ ($<r_A> < 1.25$ Å) the Coulomb interaction can overcome the kinetic energy of the electrons resulting an ordered arrangement of the Mn^{3+} and Mn^{4+} cations. The material like $La_{0.5}Sr_{0.5}MnO_3$ ($<r_A> = 1.26$ Å) does not show CO whereas the compounds like $Nd_{0.5}Sr_{0.5}MnO_3$ ($<r_A> = 1.23$ Å) and $Nd_{0.5}Ca_{0.5}MnO_3$ ($<r_A> \leq 1.18$ Å) charge order below a certain temperature. Due to larger ionic radii of La^{3+} (r = 1.22 Å) and Ba^{2+} (r = 1.43 Å) the $La_{0.5}Ba_{0.5}MnO_3$ does not show the charge ordering behavior. In fact, the crystallographic phase is not even stable. One can propose an experiment where some of the atoms of La^{3+} are replaced by Pr^{3+} (r = 1.16 Å), Nd^{3+} (r = 1.15 Å), Sm^{3-} (r = 1.13 Å) or Gd^{3+} (r = 1.11 Å) keeping the Ba and Mn site intact. This may result in the compound having a reduced average A-site cation so as to reach $<r_A> \simeq 1.25$ Å which is the approximate radius for manganites associated with the charge ordering transition. One would expect interesting and unusual behavior in such a system.

Bibliography

[1] G. H. Jonker and J. H. van Santen, Physica (Amsterdam) **16**, 337 (1950)

[2] E. O. Wollan and W. C. Koehler, Phys. Rev. **100**, 545 (1955).

[3] R. von Helmolt, J. Wecker, B. Holzapfel, L. Schultz, and K. Samwer, Phys. Rev. Lett. **71**, 2331 (1993).

[4] S. Jin, M. Mc Cormack, T. H. Tiefel, and R. Ramesh, J. Appl. Phys. **76**, 6929 (1994).

[5] S. Sundar Manoharan, N. Y. Vasantacharya, M. S. Hegde, K. M. Satyalakhmi, V Prasad, and S. V. Subramanyam, J. Appl. Phys. **76**, 3923 (1994).

[6] H. Yoshizawa, H. Kawano, T. Tomioka, and Y. Tokura, Phys. Rev. B **52**, 13 145 (1995).

[7] J. B. Goodenough, Phys. Rev. **164**, 785 (1967).

[8] T. A. Tyson, J. Mustre de Leon, S. D. Conradson, A. R. Bishop, J. J. Neumeier, H. Roder, and Jun Zang, Phys. Rev. B **53**, 13 985 (1996).

[9] P. Schiffer, A. P. Ramirez, W. Bao, and S. -W. Cheong, Phys. Rev. Lett. **75**, 3336 (1995).

[10] A. Urushibara, Y. Moritomo, T. Arima, A. Asamitsu, G. Kido, and Y. Tokura, Phys. Rev. B **51**, 14 103 (1995).

[11] D. I. Khomskii, and G. A. Sawatzky, Solid State Commun. **102**, 87 (1997); J. M. Tranquada, B. J. Sternlich, J. D. Axe, Y. Nakamura, and S. Uchida, Nature **375**, 561 (1995).

[12] D. B. Meadowcroft, P. G. Meier, A. C. Warren, Energy Conversion **12**, 145 (1972).

[13] H. S. Spacil, and C. S. Tedmon, Jr., J. Electrochem. Soc. **116**, 1618 (1969).

[14] Y. Matsumoto, and E. Sato, Electrochimica Acta, **24**, 421 (1979).

[15] G. Karlsson, Electrochimica Acta, **30**, 1555 (1985).

[16] Y. Matsumoto, H. Yoneyama, and H. Tamura, J. Electroanal. Chem. **83**, 245 (1977).

[17] J. Tanaka, K. Takahasi, K. Yukino, and S. Horiuchi, Phys. Stat. Sol. (a) **80**, 621 (1983).

[18] G. H. Jonker, Physica **XXII**, 707 (1956).

[19] J. B. A. A. Elemans, B. V. Laar, K. R. Van Der Veen, and B. O. Loopstra, J. Solid State Chem. **3**, 238 (1971).

[20] H. L. Ju, J. Gopalakrishnan, J. L. Peng, Qi Li, G. C. Xiong, T. Venkatesan, and R. L. Greene, Phy. Rev. B **51**, 6143 (1995).

[21] J. Topfer, and J. B. Goodenough, J. Solid State Chem. **130**, 117 (1997).

[22] R. Mahendiran, S. K. Tiwary, A. K. Raychaudhuri T. V. Ramakrishnan, R. Mahesh, N. Rangavittal, and C. N. R. Rao, Phy. Rev. B **53**, 3348 (1996).

[23] T. Okuda, A. Asamitsu, Y. Tomioka, T. Kimura, Y. Taguchi, and Y. Tokura, Phys. Rev. Lett. **81**, 3203 (1998).

[24] D. N. Argyriou, J. F. Mitchell, C. D. Potter, D. G. Hinks, J. D. Jorgensen, and S. D. Bader, Phys. Rev. Lett. **76**, 3826 (1996).

[25] A. Asamitsu, and Y. Tokura, Phy. Rev. B **58**, 47 (1998).

[26] S. R. Chinn, Phy. Rev. B **3**, 121 (1971).

[27] P. A. Fleury, J. Appl. Phys. **41**, 886 (1970).

[28] M. Udagawa, K Kohn, N Koshizuka, T. Tsushima, and K. Tsushima, Solid State Commun. **16**, 779 (1975).

[29] S. Venugopalan, M. Dutta, A. K Ramdas, and J. P. Remeika, Phys. Rev. B **31**, 1490 (1985).

[30] A. F. Wells, *Structural Inorganic Chemistry* (Oxford, Clarendon Press, 1984) p. 584.

[31] A. Santoro, F. Beech, M. Marezio, and R. J. Cava, Physica C **156**, 693 (1988).

[32] V. M. Goldschmidt, *Geochmische Verteilungsgestze der Elemente* **VII, VIII**, (1927-1928).

[33] A. Wold, and R. J. Arnott, J. Phys. Chem. Solids **9**, 176 (1959).

[34] A. Wold, R. J. Arnott, and J. B. Goodenough, J. Appl. Phys. **29**, 387 (1958).

[35] J. B. Goodenough, Phys. Rev. **100**, 564 (1955).

[36] Bjorn C. Hauback, H. Fjellvag, N. Sakai, J. Solid State Chem. **124**, 43 (1996).

[37] M. Verelst, N. Rangavittal, C. N. R. Rao, and A. Rousset J. Solid State Chem. **104**. 74 (1993).

[38] J. A. M. van Roosmalen, E. H. P. Cordfunke, R. B. Helmholdt, and H. W. Zandbergen, J. Solid State Chem. **110**, 100 (1994).

[39] B. C. Tofield, and W. R. Scott, J. Solid State Chem. **10**, 183 (1974).

[40] P. G. Radaelli, D. E. Cox, M. Marezio, S. -W. Cheong, P. E. Shiffer, and A. P. Ramirez, Phys. Rev. Lett. **75**, 4488 (1995).

[41] P. G. Radaelli, G. Iannone, M. Marezio, H. Y. Hwang, S. -W. Cheong, J. D. Jorgensen, and D. N. Argyriou, Phys. Rev. B **56**, 8265 (1997).

[42] G. Matsumoto, J. Phys. Soc. Jpn. **29**, 615 (1970).

[43] J. Tanaka. M. Umehara, S Tamura, M. Tsukioka, and S Ehara. J. Phys. Soc. Jpn. **51**, 1236 (1982).

[44] A. Asamitsu, Y. Moritomo, Y Tomioka, T. Arima, and Y. Tokura, Nature **373**, 407 (1995).

[45] Y. Tokura *et al.* J. Phys. Soc. Jpn. **63**, 3931 (1994).

[46] A. Chakraborty, P. Sujatha Devi, and H. S. Maiti, J. Mater. Res. **10**, 918 (1994).

[47] B. Dabrowski, K. Rogacki, X. Xiong, P. W. Klamut, R. Dybzinski, J. Shaffer, and J. D. Jorgensen, Phys. Rev. B **58**, 2716 (1998).

[48] K. R. Poeppelmeier, M. E. Leonowicz, and J. H. Londo, J. Solid State Chem. **44**, 89 (1982).

[49] J. Briatico, B. Alascio, R. Allub, A. Butera, A. Caneiro, M. T. Causa, and M. Tovar, Phys. Rev. B **53**, 14020 (1996).

[50] T. Negas, and R. S. Roth, J. Solid State Chem. **3**, 323 (1971).

[51] R. D. Burbank, and H. T. Evans, Acta Crystallogr. **1**, 330 (1948).

[52] T. Negas, and R. S. Roth, J. Solid State Chem. **1**, 409 (1970).

[53] K. Kuroda, K. Shinozaki, K Uematsu, N Mizutani, and M. Kato, J. Am. Cer. Soc. **63**, 109 (1980).

[54] B. L. Chamberland, A. W. Sleight, and J. F. Weiher, J. Solid State Chem. **1**, 506 (1970).

[55] Y. Syono, S. Akimoto, and K. Kohn, J. Phys. Soc. Jpn. **26**, 993 (1969).

[56] P. A. Hardy, Acta Crystallogr. **15**, 179 (1962).

[57] M. Parras, J. Alonso, J. M. Gonzalez-Calbet, and M. Vallet-Regi, Solid State Ionics. **63-65**, 614 (1993).

[58] J. M. Gonzalez-Calbet, M. Parras, J. Alonso, and M. Vallet-Regi, J. Solid State Chem. **106**, 99 (1993).

[59] A. N. Christensen, and G. Ollivier, J. Solid State Chem. **4**, 131 (1972).

[60] Q. Huang, A. Santoro, J. W. Lynn, R. W. Erwin, J. A. Borchers, J. L. Peng, and R. L. Greene, Phys. Rev. B **55**, 14 987 (1997).

[61] C. Ritter, M. R. Ibarra, J. M. De Teresa, P. A. Algarabel, C. Marquina, J. Blasco, J. Garcia, S. Oseroff, and S. -W. Cheong, Phys Rev. B **56**, 8902 (1997).

[62] C. Zener, Phys. Rev. **82**, 403 (1951).

[63] H. Y. Hwang, S. -W. Cheong, P. G. Radaelli, M. Marezio and B. Batlogg, Phys Rev. Lett. **75**, 914 (1995).

[64] P. G. Radaelli, M. Marezio, H. Y. Hwang, S. -W. Cheong, and B. Batlogg, Phys. Rev. B **54**, 8992 (1996).

[65] S. Jin *et al.* Science **264**, 413 (1994).

[66] J. -H. Park, C. -T. Chen, S. -W. Cheong, W. Bao, G. Meigs, V. Chakarain, and Y. U. Idzerda, Phys. Rev. Lett. **76**, 4215 (1996).

[67] C. H. Chen, and S. -W. Cheong, Phys. Rev. Lett. **76**, 4042 (1996).

[68] J. M. De Teresa *et al.* Phys. Rev. B **54**, R 12 689 (1996).

[69] M. R. Ibarra *et al.* Phys. Rev. B **56**, 8252 (1997).

[70] J. Blasco, J. Garcia, J. M. De Teresa, M. R. Ibarra, P. A. Algarabel, and C. Marquina, J. Phys. Condens. Matter **8**, 7427 (1996).

[71] P. W. Anderson, and H. Hasegawa, Phys. Rev. **100**, 675 (1955).

[72] P. -G. de Gennes, Phys. Rev. **118**, 141 (1960).

[73] A. J. Millis, B. I. Shraiman, and R. Muller, Phys. Rev. Lett. **77**, 175 (1996).

[74] M. R. Ibarra, P. A. Algarabel, C. Marquina, J. Blasco, and J. Garcia, Phys Rev. Lett. **75**, 3541 (1995).

[75] H. Roder, J. Zang, and R. Bishop, Phys. Rev. Lett. **76**, 1356 (1996).

[76] P. G. Radaelli, D. E. Cox, M. Marezio, and S. -W. Cheong, Phys. Rev. B **55**, 3015 (1997).

[77] J. F. Mitchell, D. N. Argyriou, C. D. Potter, D. G. Hinks, J. D. Jorgensen, and S. D. Bader, Phys. Rev. B **54**, 6172 (1996).

[78] R. von Helmolt, J. Wecker, K. Samwer, L. Haupt, and K. Barner, J. Appl. Phys. **76**, 6925 (1994).

[79] A. Chakraborty, D. Bhattacharya, and H. S. Maiti, Phys. Rev. B **56**, 8828 (1997).

[80] M. T. Anderson, J. T. Vaughey, K. R. Poeppelmeier, Chem. Mater **5**, 151 (1993).

[81] I. Dzialoshinsky, J. Phys. Chem. Solids **4**, 241 (1958).

[82] M. Croft, D. Sills, M. Greenblatt, C. Lee, S. -W. Cheong, K. V. Ramanujachary, and D. Tran, Phys. Rev. B **55**, 8726 (1997).

[83] T. Arima, and Y. Tokura, J. Phys. Soc. Jpn. **64**, 2448 (1995).

[84] K. H. Kim, J. Y. Gu, H. S. Choi, G. W. Park, and T. W. Noh, Phys. Rev. Lett. **77**, 1877 (1996).

[85] Y. Okimoto, T. Katsufuji, T. Ishikawa, T. Arima, and Y. Tokura, Phys. Rev. B **55**, 4206 (1997).

[86] Li Kebin, Li Xijun, Zhu Kaigui, Zhu Jingsheng, and Zang Yuheng, J. Appl. Phys. **81**, 6943 (1997).

[87] R. Gupta, A. K. Sood, R. Mahesh, and C. N R. Rao, Phys Rev B **54**, 14 899 (1996)

[88] M. N. Iliev, M. V. Abrashev, H. -G. Lee, V. N. Popov, Y. Y. Sun, C. Thomsen, R. L. Meng, and C. W. Chu, Phys. Rev. B **57**, 2872 (1998).

[89] V. B. Podobedov, A. Weber, D. B. Romero, J. P. Rice, H. D. Drew, Phys. Rev. B **58**, 43 (1998).

[90] S. Yoon, H. L. Liu, G. Schollerer, S. L. Cooper, P. D. Han, D. A. Payne, S. -W. Cheong, and Z. Fisk, Phys. Rev. B **58**, 2795 (1998).

[91] E. Granado *et al.* Phys. Rev. B **58**, 11 435 (1998).

[92] W. E. Pickett, and D. J. Singh, Phys. Rev. B **53**, 1146 (1996).

[93] S. Geller, J. Chem. Phys. **24**, 1236 (1955).

[94] A. Asamitsu, Y. Moritomo, R. Kumai, Y. Tomioka, and Y Tokura, Phys. Rev. B **54**, 1716 (1996).

[95] M. D. Fontana, G. Metrat, J. L. Servoin, F. Gervais, J. Phys. C **17**, 483 (1984).

[96] G. V. Subba Rao, C. N. R. Rao, and J. R. Ferraro, Appl. Spectrosc. **24**, 436 (1970)

[97] J. T. Last, Phys. Rev. **105**, 1740 (1957).

[98] S. D. Ross, *Inorganic Infrared and Raman Spectra* (Mc Graw-Hill, London, 1972) p. 108.

[99] P. Ganguly, and N. Y. Vasanthacharya, J. Solid State Chem. **61**, 164 (1986).

[100] K. Nakamoto, *Infrared and Raman Spectra of Inorganic and Coordination Compounds* 4th Eds. (Wiley, New York, 1986) p. 148.

[101] J. A. M. van Roosmalen and E. H. P. Cordfunke, J. Solid State Chem. **110**, 106 (1994).

[102] B. D. Culity, *Elements of X-Ray Diffraction* (Addison-Wesley, London, 1966) p.310.

[103] A. W. Baker, J. Phys. Chem. **61**, 450 (1957).

[104] G. Roberts, Anal. Chem. **29**, 911 (1957).

[105] *Insruction Manual, Spectra Physics Model-165 Ar$^+$ Laser* (Spectra Physics Inc. USA).

[106] *Insruction Manual, Spectra Physics Model-265 Laser Exciter* (Spectra Physics Inc. USA).

[107] *Insruction Manual, 1450 Tunable Excitation Filter* (Spex Industries Inc. USA).

[108] *Insruction Manual, 1482 Micromate (MIcro Raman Illuminator)* (Spex Industries Inc. USA).

[109] *Operation and Maintenance Insructions, 1877 E Triplemate* (Spex Industries Inc. USA).

[110] J. E. Pemberton and R. L. Sibrcinski, J. Am. Chem. **111**, 432 (1989).

[111] D. F. Barbe, Proceedings of The IEEE, **63**, 38 (1975).

[112] J. A. M. van Roosmalen, P. van Vlaanderen, E. H. P. Cordfunke, W. L. Ijdo and D. J. W. Ijdo, J. Solid State Chem. **114**, 516 (1995).

[113] Chaitali Roy and R. C. Budhani, J. Appl. Phys. **85**, 3124 (1999).

[114] M. Parras, J. M. Gonzalez-Calbet, J. Alonso, and M. Vallet-Regi, J. Solid State Chem. **113**, 78 (1994).

[115] W. D. Kingery, H. K. Bowen and D. R. Uhlmann, *Introduction to Ceramics* (John Wiley and Sons, Singapore, 1991).

[116] Chaitali Roy and R. C. Budhani, Phys. Rev. B **58**, 8174 (1998).

[117] M. N. Iliev, H. -G. Lee, V N. Popov, M. V Abrashev, A. Hamed, R. L. Meng. and C W. Chu, Phys. Rev. B **56**, 2488 (1997).

[118] M. R. Lees, J. Barratt, G. Balakrishnan, D. Mck Paul and M Yethiraj, Phys. Rev. B **52**, R14 303 (1995); M. R. Lees, J. Barratt, C. D. Dewhurst, G. Balakrishnan, C. V. Tomy, and D. Mck Paul, Physica B **223-224**, 532 (1996).

[119] F. Moussa, M. Hennion, J. Rodriguez-Carvajal, H. Moudden, L. Pinsard, and A. Revcolevschi, Phys. Rev. B **54**, 15 149 (1996).

[120] I. S. Jacobs and C. P. Bean, *Magnetism* Vol.III, ed. G. T. Rado and H. Suhl (Academic Press, New York, 1963) p. 271.

[121] F. Bloch, Z. Physik **61**, 206 (1930).

[122] G. S. Rushbrooke and P. J. Wood, Mol. Phys. **1**, 257 (1958).

[123] Robert M. White, *Quantum Theory of Magnetism* Mc Graw-Hill Advanced Physics Monograph Series, (Mc Graw-Hill, New York, 1970).

[124] G. G. Low, Proc. Phys. Soc. **82**, 992 (1963).

[125] L. M. Rodriguez-Martinez and J. P. Attfield, Phys. Rev. B **54**, R15 622 (1996).

[126] C. P. Bean, J. Appl. Phys. **26**, 1381 (1955).

[127] L. Weil, L. Gruner, and A. Deschamps, Compt. rend. acad. sci. **244**, 2143 (1957).

[128] A. Knappwost, Z. Elecktrochem. **61**, 1328 (1957).

[129] R. Hahn and E. Kneller, Z. Metallk. **49**, 426 (1958).

[130] A E. Berkowitz and P. J. Flanders, J. Appl. Phys. **30**, Suppl. 111S (1959).

[131] I. P. Ipatova, A. A. Maradudin, and R. F. Wallis, Phys. Rev. **155**, 882 (1967).

[132] A. J. Millis, P. B. Littlewood, and B. I. Shraiman, Phys. Rev. B **53**, 8434 (1996).

[133] W. Archibald, J. -S. Zhou, and J. B. Goodenough, Phys. Rev. B **53**, 14 445 (1996).

[134] T. R. Hart, R. L. Aggarwal, and B. Lax, Phys. Rev. B **1**, 638 (1970).

[135] P. G. Klemens, Phys. Rev. **148**, 845 (1966).

[136] M. Balkanski, R. F. Wallis, and E. Haro, Phys. Rev. B **28**, 1928 (1983).

[137] M. V. Abrashev, A. P. Litvinchuk, M. N. Iliev, R. L. Meng, V. N. Popov, V. G. Ivanov, P. A. Chakalov, and C. Thomsen, Phys. Rev. B **59**, 4146 (1999).

[138] S. Satpathy, Z. S. Popovic, and F. R. Vukajlovic, Phys. Rev. Lett. **76**, 960 (1996).

[139] J. H. Jung *et al.* Phys. Rev. B **55**, 15489 (1997).

[140] K. Ohbayashi *et al.* Jpn. J. Appl. Phys. Part 2 **26**, L420 (1987).

[141] S. L. Herr *et al.*, in *High-Temperature Superconducting Materials Preparations, Properties and Processing*, edited by W. Hatfield and J. H. Miller (Marcel Dekker, Inc. New York, 1988) p.275.

[142] Y. Khan *et al.* Phys. Status Solidi A **39**, 76 (1977).